Copyright Undertaking

This thesis is protected by copyright, with all rights reserved.

By reading and using the thesis, the reader understands and agrees to the following terms:

1. The reader will abide by the rules and legal ordinances governing copyright regarding the use of the thesis.

2. The reader will use the thesis for the purpose of research or private study only and not for distribution or further reproduction or any other purpose.

3. The reader agrees to indemnify and hold the University harmless from and against any loss, damage, cost, liability or expenses arising from copyright infringement or unauthorized usage.

Pao Yue-kong Library, The Hong Kong Polytechnic University, Hung Hom, Kowloon, Hong Kong

http://www.lib.polyu.edu.hk

A STUDY OF INTERNAL FIRE WHIRL GENERATED IN A VERTICAL SHAFT

HUNG HING YEUNG

PhD

The Hong Kong Polytechnic University
2020

The Hong Kong Polytechnic University

Department of Building Services Engineering

A Study of Internal Fire Whirl Generated in a Vertical Shaft

Hung Hing Yeung

A thesis submitted in partial fulfilment of the requirements
for the degree of Doctor of Philosophy

February 2020

CERTIFICATE OF ORIGINALITY

I hereby declare that this thesis is my own work and that, to the best of my knowledge and belief, it reproduces no material previously published or written, nor material that has been accepted for the award of any other degree or diploma, except where due acknowledgement has been made in the text.

_____

Hung Hing Yeung_____

Abstract

With appropriate setting of a vertical shaft, internal fire whirl (IFW) can be formed, which is different from a normal fire burnt in free space. The flame height of an internal fire whirl can reach several times that of a normal fire as well as with a faster burning rate. This thesis examines and discusses the criteria for the formation of an IFW inside a vertical shaft.

Correlation between the flame height and the single corner gap width has been deduced through analytical study of experimental data from an experiment on IFW. In a vertical shaft with a single corner gap, the gap width is found to be a key factor in generating the fire whirl. The swirling motion of the IFW is also studied in detail in this thesis by using a high speed camera. The formation of an IFW at different stages is analyzed in detail and vortex tubes are found moving around the horizontal pool surface. Further correlation of the flame height and the corner gap width is obtained based on the experimental data and analytical study on vertical distribution of the radial velocity.

The arrangement of different roof opening settings of a vertical shaft is also studied in this thesis. Background-oriented Schlieren (BOS) technique is applied to study the hot air flow pattern from the vertical shaft. It is found that compared to a vertical shaft model with the roof closed, the hot smoke layer temperature is lower for the roof half-closed as well as the neutral plane height is higher. Swirling motion of IFW is also studied based on experimental results and solution of the angular velocity equation for circulatory fluid motion.

Attenuation of swirling motion of the fire whirl was then studied by including the variation in vertical velocity and viscous dissipation using the basic equations of vorticity. The relative effects of baroclinic force and buoyancy were found to depend on height and on the heat release rate from the fire pool. The height and the heat release rate were found to be dependent factors on baroclinic force and buoyancy. The regions of the fire whirl are observed from bottom to top based on the baroclinic force and buoyancy ratio. Vertical variation of Froude number as well as the rotating velocity and attenuation of vorticity from bottom to top of the fire whirl were studied by analytical study. Furthermore, numerical simulations with computational fluid dynamics on medium-scale IFW using a fully-coupled large eddy simulation incorporating subgrid scale turbulence and a fire source with heat release rates compiled from experimental results were carried out. It is found that the numerical simulation results agree well with the experimental results for flame surface, temperature and flame length. IFW flame region and intermittent region were longer than those of an ordinary pool fire. The modified centerline temperature empirical formula was derived. Variations of vertical and tangential velocity in axial and radial directions are shown. The vortex core radius was found to be determined by the fuel bed size. The study in this thesis is focused on the relationship between the IFW and the vertical gap width in a vertical shaft to provide some ideas for appropriate fire safety management in tall buildings in the future. The use of highspeed camera also provides a new insight into examining the details of formation of IFW at different stages.

Acknowledgement

The author would like to express his sincere thanks to his Chief Supervisor, Professor W.K. Chow for his valuable advice and kind help throughout the research.

The author would also like to take this opportunity to thank his Co-Supervisor Dr. N.K. Fong for his useful feedback and guidance on this research project. Furthermore, the author would like to give a big thank you to Dr. S.S. Han for his kind assistance in the experimental work and his useful advice. The author would also like to thank Dr. C.L. Chow and Dr. G.W. Zou for their collaboration and help on the research project.

Publications Arising from the Thesis

Refereed Academic Journal Papers

- G.W. Zou, H.Y. Hung and W.K. Chow
  "A study of correlation between flame height and gap width of an internal fire whirl in a vertical shaft with a single corner gap"
  Indoor and Built Environment, Vol. 28, No. 1, p. 34-45 (2019).

- H.Y. Hung, S.S. Han, W.K. Chow, C.L. Chow
  "Observation on a fire whirl in a vertical shaft using highspeed camera and associated correlation derived"
  Thermal Science Published online 8 June 2019,
  https://doi.org/10.2298/TSCI181004266H

- Chung Hwei Su, JiaHong Bai, H.Y. Hung, W.K. Chow and C.L. Chow
  "A study of internal fire whirl in a vertical shaft model with partially open roof"
  Measurement, Vol. 122, p. 141-148 (2018)

Papers Submitted for consideration to publish

- Z.M. Gao, S.S. Li, Y. Gao, H.Y. Hung and W.K. Chow
  "Numerical studies on swirling of internal fire whirls with experimental justification"
  Building simulation – Submitted for consideration to publish, June (2020)

- H.Y. Hung, W.K. Chow and C.L. Chow, Z.M. Gao and S.S. Li, Y. Gao,
  "Attenuation of swirling motion of a fire whirl in a vertical shaft"
  Fire Technology – Submitted for consideration to publish, June (2020)

Contents

Chapter 1. Introduction

1.1 Background of fire whirl

Fire whirl is a whirlwind induced by a fire which is usually being made up from flame or ash. Fire whirl is also known as a fire tornado because it can be disastrous when it is formed with a large and high flame height. There are some catastrophic examples of fire whirl in the past. The fire tornado occurred in the 1923 Great Kanto earthquake [1] in Japan has caused a gigantic city-sized firestorm which caused 38,000 people to death in just a quarter of an hour in the Hitfukusho-Ato Region of Tokyo.

One of another example is the numerous large fire whirls that developed when the oil storage facilities are being struck by lightning near San Luis Obispo, California on 7 April 1926 [2], the lightning has created severe damage to the structural building on the site, causing two peoples' death. The fire storm has been lasted for 4 days and produced many whirlwinds with conditions that produced severe thunderstorms, in which the larger fire whirls carried debris 5 kilometers away.

A more recent example of fire whirl is reported in the New Zealand wildfire in 2017, formed on day three of the 2017 Port Hills fires in Christchurch. It is reported the height of the fire whirl was estimated to reach 100 meters high.

Fig 1.1 Fire Whirl at the New Zealand Port Hills fire (Stuff.co.nz, 2017)

1.2 Definition of internal fire whirl IFW

As mentioned, fire whirl can be occurred in both urban and natural area [3-6, 7]. When intense rising heat and turbulent wind conditions combine to form whirling eddies air, fire whirl will occur. The different between the natural fire whirl and an internal fire whirl is that for natural fire whirl, the fire whirl is formed in open area where the fire is no enclosed by any wall or partition. Moreover, the fire source of the fire whirl can move freely as well as the fire whirl itself. As for an internal fire whirl, the fire source of the fire whirl is fixed in a location and the internal fire whirl is readily created in a vertical shaft by the burning of a small fire [8].

1.3 Formation of the internal fire whirl

The principle of the formation of internal fire whirl is being studied by researchers [9]. When a pool fire is being burnt in a free space, the buoyancy created will move the fuel vapours upward. The mean flame height is taken to be the value with half of the time with flame and deduced by observing the transient flame heights. Moreover, the lower part of the flame which is the luminous flaming region looks to be more stable. Vice versa, the upper portion of the flame can be treated as an intermittent flaming

region. Thus, the surrounding air would then be entrained to give a diffusional flame. However, when the situation is changed such that the pool fire is now being placed in a vertical shaft, due to the barrier of the solid boundary, it limits the motion of the induced air. Upward circular motion might be resulted if buoyancy is generated by the heat source there. The hot gas located at the central region with a lower density would move upward as it has higher buoyancy. Thus, an internal fire whirl is then be induced. The flame height of the fire is increased as well as the flame radius is also reduced. The flame height of the fire whirl in a vertical shaft is much higher than that of a normal pool fire being burnt in an open space. Furthermore, the burning time of an internal fire whirl will be shorter compared to that of a free burning fire in open space.

Chapter 2. Literature Review

2.1 Previous study on internal fire whirl

When the internal fire whirl is formed inside the vertical shaft, the fire environment in the vertical shaft is then very hazardous due to the extended flame length and fast rate of burning. Studied on internal fire whirl has been done previously by scholars and researchers. Research is done by Emmons and Ying [3] on a fire whirl experiment in which the fire whirl is formed at the center of a rotating screen which a controlled angular momentum is imparted to the ambient air. The fire whirl is formed from a liquid acetone fuel pool. From the experiment results, it is found that the fluid motion at the outer part of the flame core of the fire whirl is in a free vortex form. Furthermore, the radial temperature distribution of the fire whirl is also measured by a hot wire method. Based on the temperature distribution obtained from the said hot-wire measurement, it shows that the fire whirl is a rotating cylinder fire that has a rich fuel in the inside but not the outside part of the flame. Moreover, from the experiment result, they deduced that the turbulent plume theory is extended to include combustion and angular momentum. It is found that when the angular momentum of the fire whirl increased the turbulent mixing coefficient will then be decreased. Also they discovered that when the elevation above the ground is increased, the turbulent mixing coefficient will also be increased.

Stable fire whirl is generated by Satoh and Ying in the laboratory [10], which the fire whirl is generated in a vertical square enclosure in which the roof of the enclosure is hollow. The enclosure also has symmetrical gaps at each of the four corners between adjacent vertical enclosure walls. The fire whirls generated is being observed

systematically and it is found that the integrity of the fire whirl heavily rely on the flow induced through the gap of the enclosure. The most crucial conclusion deduced from the experiment is that is the gap opening of the enclosure has a huge influence on the stability of the fire whirl and it is important and essential to the formation of the fire whirl. Furthermore, it is further found that the mentioned two characteristics are hydrodynamic in nature which is, the entrainment of air through the openings of the vertical enclosure essential to the generation of the fire whirl and its stability to maintain the integrity itself.

Medium-scale fire whirl experiment was conducted by Snegirev et al. [11]. Whirling flame fire is being set in a compartment with a door at the side of the front wall of the compartment. The compartment also has a vent opening at the roof. A fuel source which is a fuel pan containing diesel fuel is located at the center of the compartment. Fire whirl is observed in the experiment after the fuel is ignited in which rotation is observed and the fire is significantly lengthened.

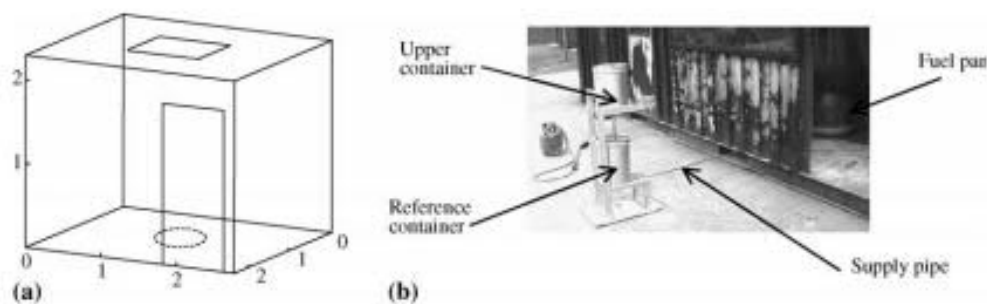**Fig 2.1 Experimental set-up by Snegirev et al. [11]**

The periodic formation and destruction of the fire whirl core is observed in the experiment. It is also found that there is an increment for the time-averaged burning rate during the burning process. It is identified that two conditions is essential to develop the fire whirl which are non- zero background vorticity and vertical acceleration of the flow.

Another experiment was conducted by Kuwana et al. [12] in which they tried to recreate the fire whirl occurred in the Great Kanto earthquake in Tokyo in 1921. Scaled model in scale 1:1000 is used in a low speed open-loop wind tunnel. 16 numbers of experiments are conducted using n-heptane as the fuel for the pool fires. From the experiment result, it is found that the critical lateral wind velocity is 1m/s that cause the formation of intense fire whirl. Furthermore, there are 3 types of fire whirls being identified in the experiment. The first type is fire whirl that is very stable and intense; the second type is fire whirl that is relatively not so stable and will spun off from time to time from the burning area; the third type of the fire whirl is fire whirl formed by the air circulation moving around the burning area.
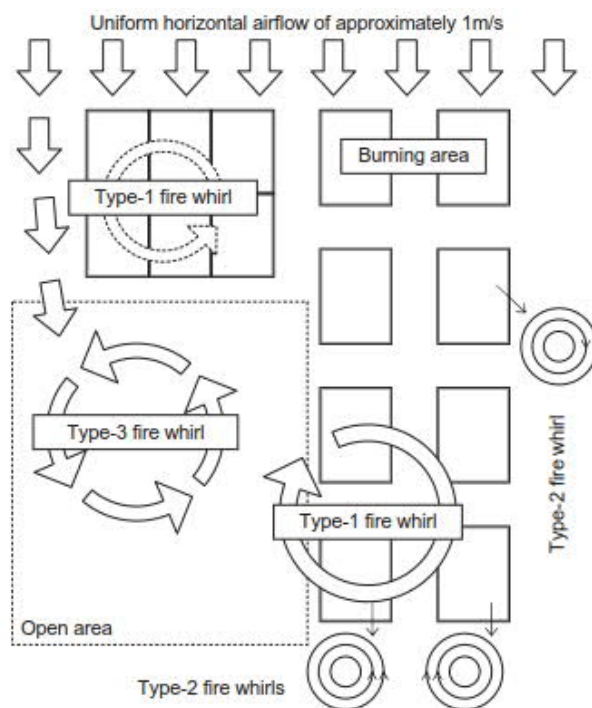

Fig 2.2 Air flow direction and types of fire whirl formed in the experiment conducted by Kuwana et al. [12]

The correlation of the flame height and fire heat release rate and ambient circulation is being studied by Lei et al. [13] by using a medium-scale model on the fire whirl. A

6

shaft model of 2m x 2m x 15m with channel open at top and 20 cm wide vertical gap at the corner to allow air to entrain into the shaft which allows the rotating flow and movement of air which is essential for the fie whirl formation. pitot tubes and type K thermocouples are being used to measure the velocity and air temperatures at different location inside the shaft model.

Fire whirl is successfully formed in the shaft model. Several founding is observed from the experiment results. It is found that free burning fire whirl is a highly stable burning phenomenon with large quasi-steady period, burning rate of the fire is dependent to the diameter of the pool fire which is more or less the same with normal open pool fire. However, when the pool diameter increased, the transition turbulent burning occurs earlier. A correlation of $H = K \cdot (Q \cdot \Gamma^2)^m$ was deduced relating the height of fire whirl to the fire release rate and ambient circulation. Furthermore, from the temperature profile obtained, it is found that the fire whirl is fuel rich in the inside and the pool diameter and heat release rate of the fuel do not significantly affect the radical temperature profile. Likewise, same with normal pool fire, there are 3 distinct zones for the fire plume of fire whirl but with different normalized ranges. The fire whirl has a higher ratio of continuous flame height to the overall flame height, and higher maximum centerline excess temperature in continuous flame region. One more final observation from the experiment is that the plume of the fire whirl at its origin has moderate swirling and the plume has a tendency to become buoyancy dominated downstream and with little swirling.

Numerical study is also applied to study the internal fire whirl by other researchers. Computational field model is used by Yuen et al. [14] to study the fire model on internal fire whirl developed by other researchers. Fire Dynamic simulator FDS is

being used. To carry out the simulation, liquid fuel evaporation model is being used together with other essential components such as combustion, turbulence and radiation models which are used to describe the physical and chemical situation that is commonly found in an internal fire whirl. When evaluating the evaporation rate of the fire, radiation as well as convection heat feedbacks from the fire source to the liquid fuel has been taken into account. From the numerical simulation result, it is found that the four unique stages for internal fire whirl has been successfully captured which include the initial stage where the flame circulates around the fuel pool center and tilted towards the wall with a short flame height; the second stage in which the flame begins to rise and revolute along the middle axis of the fuel pool and the flame height is gradually increased; the third stage is the fire whirl that is fully developed and stable in which the flame height reaches the maximum and stay continuously for a certain period of time; the last stage is the decaying stage where the fire begins to stop as the fuel is running out. Based on this numerical study, it is suggested that in order to produce the fundamental characteristics in future numerical simulation, it is necessary to obtain the detail chemical reactions scheme of the fire whirl. Also, based on the numerical simulation, some characteristics of the fire whirl are found. The fuel which is in gas state is pushed to an upper level of the fire as the buoyancy fluid motion of the fire is located at the center. Besides, the thin shapes and the limited horizontal dispersion of the flame could be due to the spinning effect. Furthermore, it can be seen that the radiation feedback to the fuel source increase as the flame occurs straight on top of the fire.

As mentioned in some previous study, there are some significant and unique regarding the internal fire whirl. Experiment and studies has been conducted by Jiao et al. [15] to investigate the instabilities of the fire whirl flame which can be found in the

8

inclined flame revolution stage when the fire is transformed from a normal pool fire to a fully developed fire whirl. It is found that from the experiment observation that the revolution of the flame is an important flame instability during the transformation of the fire whirl. It is also observed that the periodic fluctuations of the inlet velocity disappear and outside the flame core, a local annular external recirculation zone (ERZ) is found in the flame precession stage. Various important findings are deduced from their study. It is found that the flame revolves around the vertical axis of the pool fire and the angular velocity is increased until a critical frequency is reached for the formation of the fire whirl. In contrast with the annular ERZ which is found adjacent to the outer boundary of the flame when the flame precession start, a central recirculation zone (CRZ) and vortex breakdown cannot be found. Also, the inlet velocity fluctuates when the fire whirl is unstable and become the velocity become constant when a stable internal fire whirl is formed. The ambient circulation and the average inlet velocities are in linear proportion among different pool sizes. Furthermore, the flame revolution and precession frequencies is dependent on the average inlet velocity having a Strouhal numbers of 0.42 and 0.80 respectively. Moreover, the rotating direction of the fire whirl flame is same as flame revolution and precession. The unstable variation of the inlet flow is said to be the cause of the flame revolution where the flame precession is seen to be related to the ERZ in the fire whirls.

Apart from the inflow velocity or the air entrainment that causes the formation of the fire whirl, there can also be criteria that affect or even is essential to the formation of the internal fire whirl. From the study by Kuwana et al. [16], a fire whirl experiment is conducted to demonstrate the effect of the fuel burning rate on the formation of fire whirl. A split cylinder set up with fire source inside is used to allow air entrainment

inside the cylinder for the formation of the fire whirl. Two case scenario is being consider in which the first one is using a 3 cm diameter ethanol pool fire as fire source while in the second scenario, methane burner is used as the fire source. The reason for the difference of the fire source is to demonstrate the different burning rate of the fire and to find out how it will affect the formation of fire whirl as the methane burner has a fixed constant burning rate and the burning rate of the free burning ethanol pool can be varied from time to time. From the experiment result, it is observed that when inlet flow is set where air entrain into the cylinder, only the ethanol pool fire demonstrates a tall flame height with about 3 times taller, although both scenario the fire rotates with the help of air circulation. This confirms that the burning rate has a dominant role over the air flow circulation on the influence of formation of fire whirl.

2.2 Previous study on ventilation provision affecting internal fire whirl

As discussed in the previous section of the literature review, air entrainment and ventilation provision is essential for the formation of internal fire whirl. Ventilation provision at the sidewall has been identified as a key point in onsetting a fire whirl as reported.

The effect on the sidewall ventilation provision is being investigated by Zou and Chow [17]. An experiment is conducted where internal fire whirls are generated in a 9m tall vertical shaft model. Flame shapes in burning of a gasoline pool fire is being observed with different opening gap width and size of pool fire. Various parameters are measured in the experiment such as fuel mass of the pool fire, transient air temperature and the internal fire whirl flame height. It is also confirmed that from the experiment that when the gap width is too wide or too narrow, internal fire whirl cannot be formed as shown in the graph below:
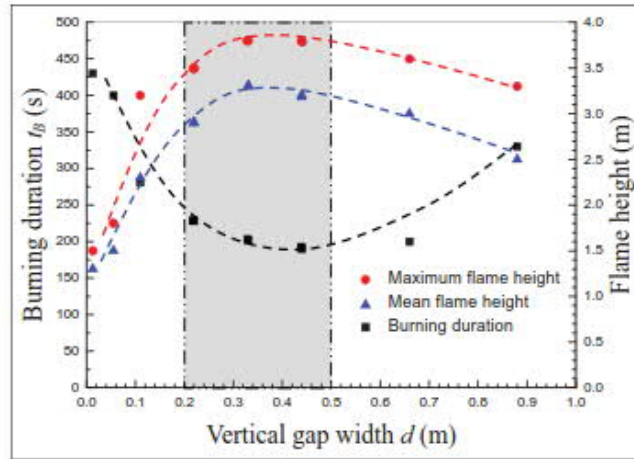
Fig 2.3 Burning duration and mean flame height curves for different gap widths

[17]

There are several conclusions drawn from the experiment study, the first one is that when the gap width is too narrow or too wide, internal fire whirl cannot be formed. Also, in the paper, it is suggested that the internal fire whirl is classified into 5 stages of development: the first stage in which the pool fire is burnt in a way behaving similar to normal pool fire in open air; the second stage is the burning rate of the pool fire start to increase; the third stage is that the swirling flame motion start to develop; the forth stage is that the internal fire whirl become fully mature and stable; the last stage is the decay stage of the internal fire whirl. Also zone are identified as shown in the below experiment observation which are zone I where the flame rotates violently at the bottom part of the fire; zone II is the middle part of the fire whirl which has a slower swirling rate and zone III which is the upper part of the fire whirl where there is no flame rotation. The Heat Release Rate (HRR) of the pool fire is also measured in the experiment; it is found that the HRR of the internal fire whirl is two times than that of a normal pool fire.

Another study on the setting of the corner gap width effect to the internal fire whirl is

done by Chow and Han [18]. In the study, an experiment is conducted by using a rectangular vertical shaft with a small fire size propanol pool fire inside the shaft which is located at the bottom center of the shaft. Different settings of the side gap opening are tested. The width of the gap width is being tested and it is found that when the gap is too narrow which is under 1.5 cm of 34cm of the width of the shaft, no internal fire whirl is formed. As for the gap width from 1.6cm to 3.6 cm, internal fire whirl is formed. Besides varying the gap width, the experiment also studied the effect of whether there will be effect on the vertical position of the gap width. Blockage is being placed in various position of the gap width. It is found that when there is blockage being placed at the bottom of the gap opening, no internal fire whirl is formed due to no air entrainment is allowed to enter into the shaft at the bottom which is essential for the formation of internal fire whirl for the flame rotation. Furthermore, when there is a large blockage at the top of the opening which only provides little opening at the bottom of the gap, internal fire whirl also cannot be formed. This may be due to the lack of air entrainment into the shaft where the flame rotation cannot be favoured.
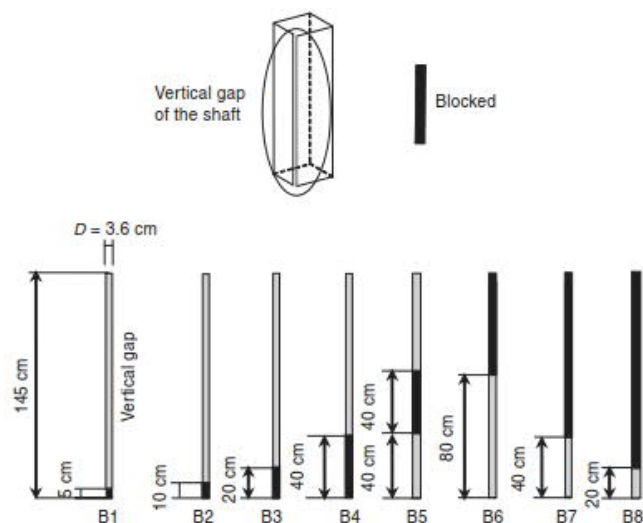

Fig 2.4 Experiment set up to study the effect of corner gap opening on internal fire whirl by Chow and Han [18]

12

Larger scale fire test is also conducted by Chow et al. [9] where internal fire whirls are induced in a 15m tall vertical shaft. Ventilation provision are provided at the side wall in which the width of the opening can be varied. Different diameter of gasoline pool fire up to 0.46m are set up at the center of the floor of the vertical shaft.
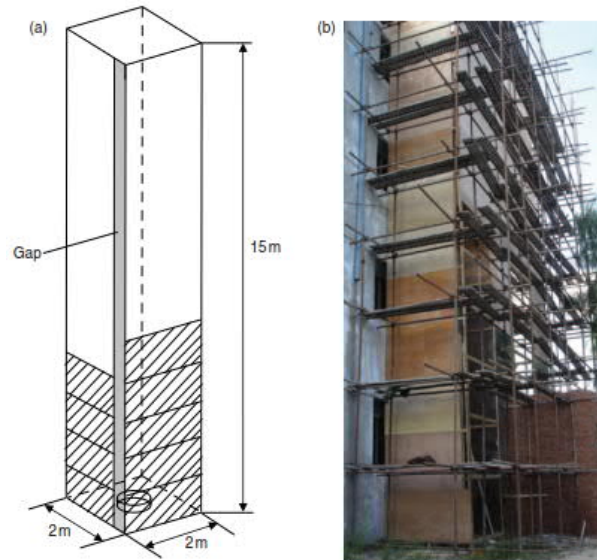
Fig 2.5Vertical shaft setting of large scale internal fire whirl experiment by Chow et al. [9]

The flame height and burning duration are measured. Average flame height of 1 to 4.5m is recorded when internal fire whirl is formed in the vertical shaft. From the experiment it is found that the air supply at the upper part of the shaft is a key factor for the formation of the internal fire whirl. The induced whirling motion of the fire whirl relies on the combustion which is sustain by oxygen therefore the ventilation at the side wall opening is essential and the flame will not have whirling motion if the oxygen supply is not adequate. There are four stages classified for the internal fire whirl which are the flame rising-up stage, stale flame, whirling stage and decay stage. These stages are also mentioned in the previous literature. By using the correlations of flame height of free burning fires, the correlation of the flame height of the fire whirl with fuel mass and other parameters are deduced. Furthermore, CFD modeling is used

as validation of the experiment result and the correlation expression.

Apart from rectangular shaped vertical shaft model to produce internal fire whirl, a hexahedron shaped vertical shaft is being used to study the effect of side openings on the internal fire whirl by Yu. et al. [19]. The experiment in the research used the vertical shaft with six free setting horizontal openings so that the width of the opening can be adjust in different widths to allow different scenarios for the air inlets as shown below:

(a)   (b)   (c)
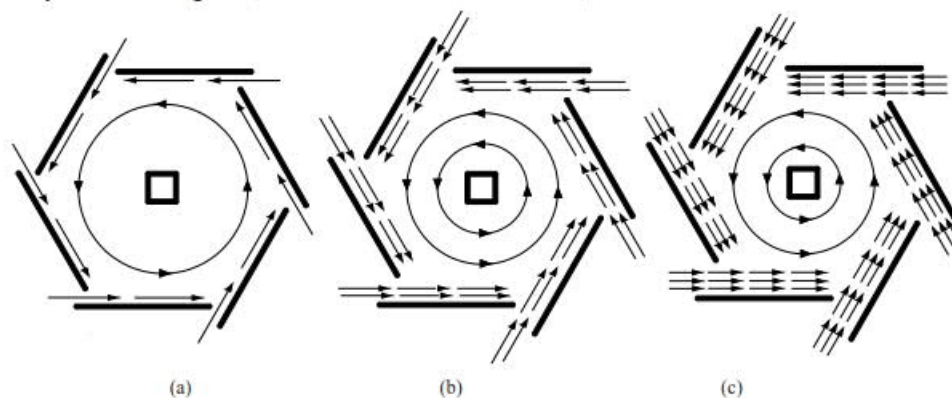
Fig 2.6 Air flow in the vertical shaft with different opening width in experiment conducted by Yu et al. [19]

The experiment results show that when the opening width is too narrow, the formation time of the internal fire whirl is shorter while it increases when the gap width opening is also increased. The integrity and stability reach the optimal stage when the gap opening is about 20 to 30 cm. This means that when the gap is too narrow or too large, internal fire whirl cannot be formed. The paper explain such results by claiming that when the gap opening is too narrow, the air flow around the flames cannot rotate. On the other hand, if the gap opening is too large, the flow velocity will become very slow that cannot sustain the whirling motion of the internal fire whirl so that the fire whirl will be weak and unstable.

2.3 Importance on fire safety for internal fire whirl

Different arrangements to generate a fire whirl inside an enclosure were reported in the literature. The fire whirl is called an internal fire whirl (IFW) in this study to distinguish from the external fire whirl which might move over the burning fuel. An IFW has a fixed physical fire size, and not spread over the fuel surface. An IFW can be created in a vertical shaft for tall buildings with appropriate sidewall ventilation arrangement [18,20-22]. The flame height was extended several times longer with the burning rate increased. Even for a relatively small size of fire would induce an internal fire whirl.

Any condition similar to the arrangement as mentioned in the literature review in an atrium or inside a building like a lift shaft might give chance for creating an internal fire whirl which can have a very tall flame height. If an internal fire whirl is really being on-set inside a building or atria, the consequence will be very serious and disastrous that can leads to human and property lost. Appropriate fire safety measures [23-26] will be needed to counter such possibility of limiting the chance for on setting the internal fire whirl.

However, understanding of the fundamental characteristics of internal fire whirls is still inadequate [27,28] and therefore proposed for further study in this PhD degree project. Correlations of the flame height of IFW with these vortex parameters were investigated through theoretical analysis, experiments and numerical simulation, which can provide fundamentals for further analytical studies

The swirl number [29-32] and Froude number [33-36] are used to study the physics of

vorticity-buoyancy interaction characterizing internal fire whirls. Computational Fluid Dynamics fire models [37-42] will be applied together with appropriate combustion models to study the air flow patterns and flame structure in the vertical shaft. Sources of vorticity [43-45] such as the shearing effect and the baroclinic mechanism can then be better understood by combining all the physical model observations and numerical prediction.

Chapter 3. Correlation between Flame Height of Internal Fire Whirl and Gap Width of Vertical Shaft

3.1 Summary of experimental result of previous study

Large scale fire test on the IFW is carried out by Zou and Chow [22] in which a vertical shaft model of 9m height and square base of side 2.1m in a large burning hall in Harbin, China A vertical gap with adjustable gap width d_g was opened at one corner of the model. Ambient air was sucked via the gap into the shaft when burning started. Two pieces of 4-mm thick glass sheets each of height 1.5 m were inserted on the front wall of the shaft for observing the flame motion and shape (Fig. 3.1).
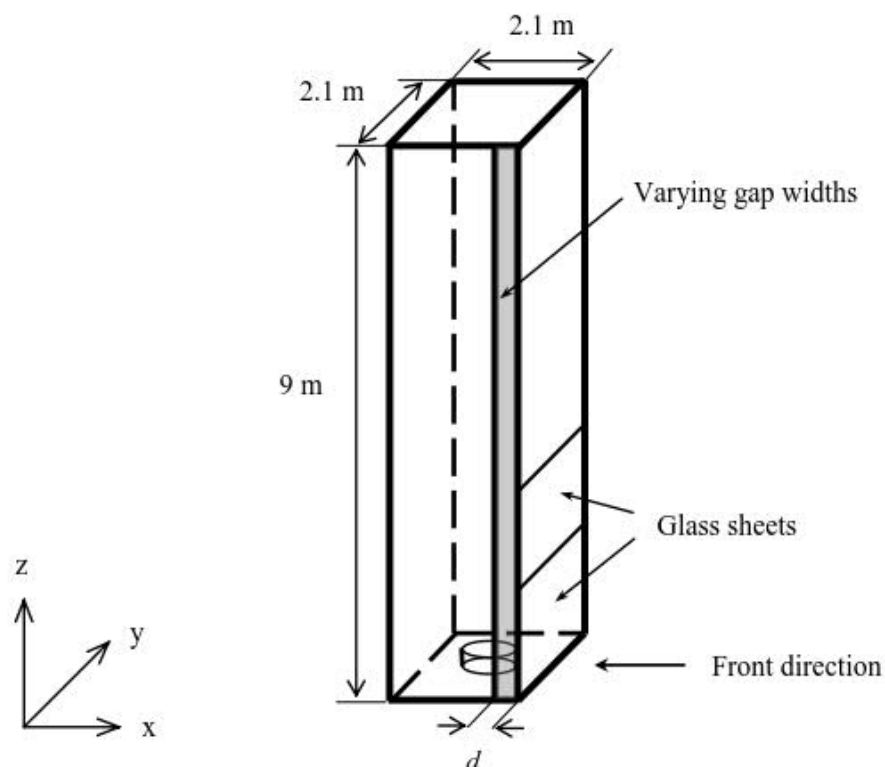

Fig. 3.1: The vertical shaft model with a single corner gap

A liquid pool fire of tray diameter D equal to 0.46 m was placed at the centre of the base of the shaft model as in Fig. 3.1. Gasoline 93[#] was used as fuel in these experiments. The physical parameters of gasoline 93[#] are [46]: heat of combustion 43,070 kJ/kg (10,300 kcal/kg), density from 700 kg/m^3 to 790 kg/m^3, latent heat of vaporization from 290 kJ/kg to 315 kJ/kg, and self-ignition point from 415°C to 530°C.

3.1.1 Experimental result

Stack effect and wind action in a tall building shaft would affect IFW characteristics and depend on atmospheric conditions. The earlier experiments were carried out [22] in a vertical shaft model of height 9 m inside a large burning hall in summer of Harbin, Heilongjiang, China. Stack effect in the shaft model is not significant. Further, low wind in summer would not bring wind action to the indoor shaft model inside the experimental hall. The ambient temperature and pressure during the test were from 21°C to 24°C and 98510 Pa to 99800 Pa, respectively. Experimental observations indicate that an IFW [22] can be generated by a gasoline pool fire burning in a square vertical shaft model with an open roof and a sidewall corner gap of appropriate width.

For gasoline pool fire burning in free space the flame would take a shape shown in Fig. 3.2a. The following phenomena were observed when a pool fire burnt in a vertical shaft under different corner gap widths. For burning in the shaft model with no corner gap, flame did not swirl (Fig. 3.2b). The flame behaved in a manner similar to a pool fire in free space (Fig. 3.2a).

(a) Fire in free space	(b) Fire in shaft without corner gap	(c) Steady internal fire whirl

Fig. 3.2: Flame shape

When the corner gap width was increased to an appropriate value, a steady fire whirl would be developed (Fig. 3.2(c)). The formation of IFW follows a sequence of stages consisting of flame tilting, revolution, rotation (or self-spinning) with precession, and eventually IFW formation (Fig. 3.3(a) through Fig. 3.3(f)). Note that there is no circular motion in the flame for fire burning in free space.

When the corner gap width was increased further, both flame rotation and precession weakened. The pool fire behaved as that in free space again when the gap width was bigger than a certain value.

For a gasoline fire pool of tray diameter of 0.46 m burning in the 9 m tall shaft model [22], no swirling motion was observed for corner gap width less than 0.11 m or larger than 0.66 m. Without the formation of IFW, the flame height of the pool fire in the model was about 1.3 m, similar to the flame height for the pool fire in free space. When an IFW was created, the flame height was dependent on the gap width as

shown in Table 3.1. The data were used in the present work for correlational study in the following sections.
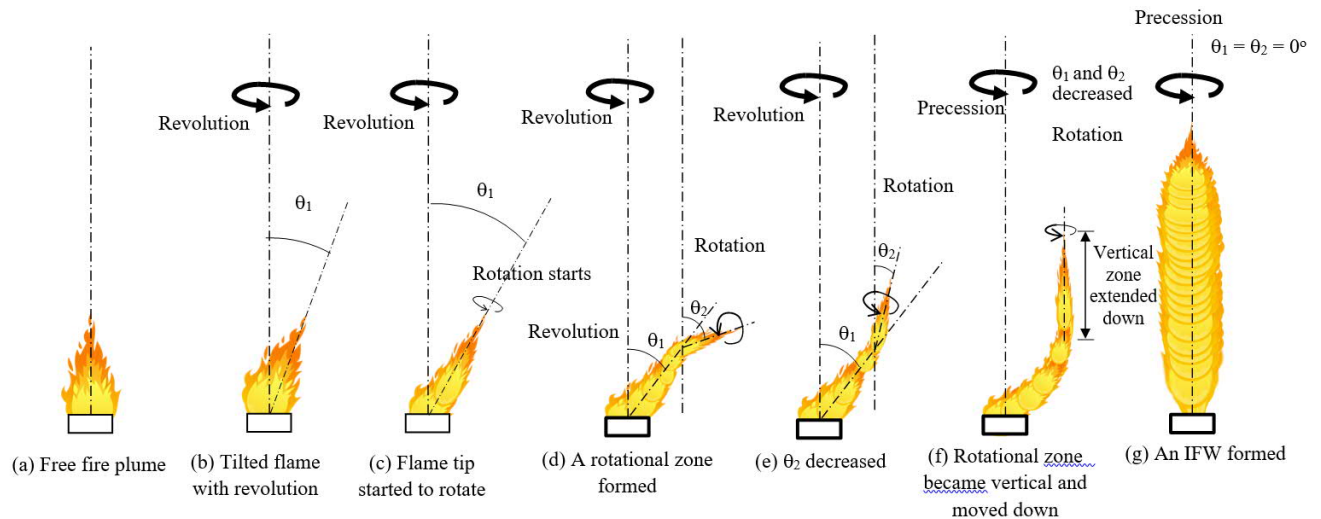
Fig. 3.3: Stages to form an IFW

Table 3.1. Flame characteristics corresponding to a pool fire of diameter 0.46 m in a vertical shaft 9 m high and square base of side 2.1 m by Zou and Chow [22]

Vertical gap width d_g [m]	Mean flame height f_h [m]	$d_g^* = \dfrac{d_g}{a}$	$\ell n d^*$	$f_h^* = \dfrac{f_h}{D}$	$\ell n f_h^*$	Observation on IFW
0.22	2.9	0.1048	-2.2561	6.3043	1.8412	Moderate swirling
0.33	3.2	0.1571	-1.8506	6.9565	1.9397	A clear IFW
0.44	3.1	0.2095	-1.5629	6.7391	1.9079	A clear IFW
0.66	2.9	0.3143	-1.1575	6.3043	1.8412	Moderate swirling
0.88	2.5	0.4190	-0.8698	5.4348	1.6928	Weak swirling

3.2 Basic equation derived from literature

An IFW generated by a rotating disc surrounded by a fine mesh was reported by Emmons and Ying [3] A 10 cm-diameter acetone pool fire was placed at the centre of the disc. A buoyancy-driven upward flow was induced by the pool fire. Air passed through the rotating screen to generate swirling motion. Flame height and fuel consumption rates increased with speed of the disc.

IFW experiments were conducted on spinning a 5-cm-diameter methanol pool fire by Chuah et al. [47,48] Vortex flow around the fire whirl was observed to satisfy the continuity and momentum equations with the appropriate boundary conditions. A mathematical model of Equation (3.1) was proposed to predict the flame height f_h with a simple scaling analysis:

$$f_h = (f_{h,\infty}^2 + A\frac{r_p^4}{c^2})^{1/2} \tag{3.1}$$

In the above equation, $f_{h,\infty}$ is the flame height of pool fire without spin, r_p is pool radius (pan radius), c is radius of vortex core and A is a constant.

IFWs generated in square vertical channel with a gap at each corner were studied by Matsuyama et al. [49], Zhou et al. [50] and Lei et al. [13,51] The temperature distribution of whirling flames, the height of whirling flames, and flow velocity were measured. Different equations were proposed to describe the height of whirling flames.

For heat release rate $\dot{Q}$ of 20 kW, the average flame height H [m] predicted by CFD and experimental data was proposed by Matsuyama et al. [49] in terms of the characteristic fuel size D [m], and the non-dimensional heat release rate $\dot{Q}^*$ as given in Equation (3.2a):

$$\frac{H}{D} = a_0 + a_1 \dot{Q}^{*2/5} \tag{3.2a}$$

where a_0 and a_1 are constants.

For free burning, the equation is expressed as Equation (3.2b):

$$H/D = -1.02 + 3.7\dot{Q}^{*2/5} \tag{3.2b}$$

The average height of whirling flames measured by the experiment was double the values obtained from Equation (3.2b) for free burning.

The dimensionless form of heat release rate $\dot{Q}^*$ can be evaluated by Equation (3.2c) in terms of $\dot{Q}$, density of ambient air ρ_∞ (in kgm^{-3}), specific heat capacity $c_{p,\infty}$ (in kJkg^{-1}K^{-1}), ambient temperature T_∞ (in K), acceleration of gravity g (in ms^{-2}) and diameter of fuel tray D (in m).

$$\dot{Q}^* = \frac{\dot{Q}}{\rho_\infty c_{p,\infty} T_\infty \sqrt{gD}D^2} \tag{3.2c}$$

Equations (3.3) and (3.4) are the average flame height proposed by Zhou et al. [50]

$$ln\,H^* = ln\left[\frac{DK(\,0.37\dot{Q}^*\,)^m}{H_p}\right] + 2.79m\,ln\,\Gamma^* \tag{3.3}$$

or

$$H^* = 0.36\Gamma^{*1.11} \tag{3.4}$$

In Equations (3.3) and (3.4), $\dot{Q}^*$ and H_p are respectively the dimensionless heat release rate and the flame height in free burning, $H^* = H/H_p$ is the dimensionless height of whirling flames, D is fuel tray diameter, $\Gamma^* = \Gamma\sqrt{gD^3}$ is the dimensionless circulations, which is the vorticity, K and m are constants.

Equation (3.5) is the average flame height proposed by Lei et al [13,49]

$$H^* = K(\dot{Q}^* \cdot \Gamma^{*2})^m \tag{3.5}$$

In Equation (3.5), $H^* = H/D$ is the dimensionless height of whirling flames, $\dot{Q}^*$ is the dimensionless heat release rate, K is a comprehensive dimensionless quantity and m is a constant.

Steady axi-symmetric strong fire whirls with axes inclined 30° from the vertical orientation were generated by Chuah et al. [47] in modelling an inclined fire whirl. The rig had six-sided fixed frame wall with two slots. Changes in the velocity profile were assumed to represent a different possible mechanism for extending the flame by

23

correlating flame characteristics to the strong-vortex approximation and its compensating regime, while accounting for the influence of the viscous core. Equation (3.6) was proposed by Klimenko and Williams for prediction of the flame height of IFW with a strong rotation obtained by using the compensating regime of vortical flows.

$$L = \frac{F_z}{\alpha_{\text{eff}} D Z_{\text{st}}} = \frac{u_0 d_0^2}{8\alpha_{\text{eff}} D Z_{\text{st}}} = d_0 \frac{Pe}{8\alpha_{\text{eff}} Z_{\text{st}}} \tag{3.6}$$

In Equation (3.6), L is the flame length, α_{eff} is the effective exponent (in the case of a Burgers vortex $\alpha_{\text{eff}} = 2$), D is the diffusion coefficient, Z_{st} is the stoichiometric value of mixture fraction, r_0 is radius at axial location of the fuel source (a pan in experiments), u_0 is the average velocity, $d_0 = 2r_0$, Pe is the Peclet number which stands for the term of radius at axial location times average velocity over the diffusion coefficient and F_z is the flux of the mixture fraction given by Equation (3.6a):

$$F_z = \int_0^\infty uZ\rho r \, \mathrm{d}r = \rho_0 u_0 r_0^2 / 2 \tag{3.6a}$$

Numerical simulation and laboratory experiment were carried out by Zhou and Wu [52] to illustrate that fire whirls can be generated through the interaction between a central flame surrounded by arranged or randomly distributed flames. The effect of rotation speed on the flame height was studied. Equation (3.7) is a non-dimensional equation proposed to relate the flame height H to the rotation speed ω through the non-rotating flame height $\overline{H}$ and coefficients L_1 and L_2.

24

$$H \sim \overline{H} - L_1\omega + L_2\omega^2 \qquad\qquad (3.7)$$

As summarized above, there were many studies on fire whirls with different physical conditions and geometry affecting flame heights. However, understanding of the mechanism of fire whirls is still not adequate. At the moment, there is no theory which can explain all the results satisfactorily. No general expression of the whirling flame height has been deduced yet. In view of this, fire whirls generated by a simple vertical shaft model with a single corner gap was studied in this paper.

A fire whirl may be taken as a rotational flow in which combustion drives convection through buoyancy. This convection can be simplified by externally imposed circulation and buoyancy interaction. Assume that the flow is axi-symmetric, steady and inviscid. The steady state Euler equations for a perfect gas in the low Mach number limit would give a tractable model with minimal complexity.

3.3 Analytical study

In this study, the Boussinesq model was formulated first, and then the Boussinesq constraint was relaxed by incorporating large density variations. The non-dimensional form of the governing equations and the boundary conditions were formulated. Results for a buoyant plume with and without swirl were then obtained. The section begins with a description of how the plume changes when subjected to different levels of circulation. The differences in plume development using the Boussinesq model and non-Boussinesq model were contrasted.

The stream function equation was solved numerically with appropriate boundary and initial conditions. The equations were discretized using second-order finite differencing for a standard grid formulation. The form of equation was a modified Poisson equation. To facilitate a solution, a pseudo-time implicit discretization scheme was implemented. The domain for the calculations has dimensions $4r_0 \times 20r_0$, for the radial and axial directions, respectively. Due to regions of high gradients, especially near the centreline, a fine grid was used for simulation, giving a total of 256×1024 cells.

For an IFW generated as in Fig. 3.3g, the radial pressure gradient was reduced due to the centrifugal force of circular motion. The vorticity-driven flow would keep the cylinder shape of fire relatively stable in space and time, giving laminar flow to the fire whirl. That means the radial turbulent pulsation of the fire whirl would be greatly reduced. The flame was similar to laminar diffusion flame with an inner fuel-rich zone and an outer air zone separated by a relatively smooth and stable flame surface. Air surrounding the flame was separated by the stable flame, showing typical characteristics of a diffusion flame. As the radial air entrainment of the fire whirl flame was reduced, the fuel-rich region of the fire whirl moved upward to mix with air. Therefore, a flame with a high height-to-diameter ratio was formed.

For a normal pool fire of which the fuel and the pool surface have equal area with air entrainment available from all sides, a high flame engulfment rate at the radial direction for a pool fire would be higher than that of fire whirl. Hence, the flame diameter of the pool fire would be larger than that of the fire whirl.

The flame of an IFW as formed in Fig. 3.3g can be taken as a high-speed rotating cylindrical diffusion flame as shown in Fig. 3.4. Based on this observed pattern, an axis of symmetry was formed along the vertical centreline with air entrained horizontally from all directions.
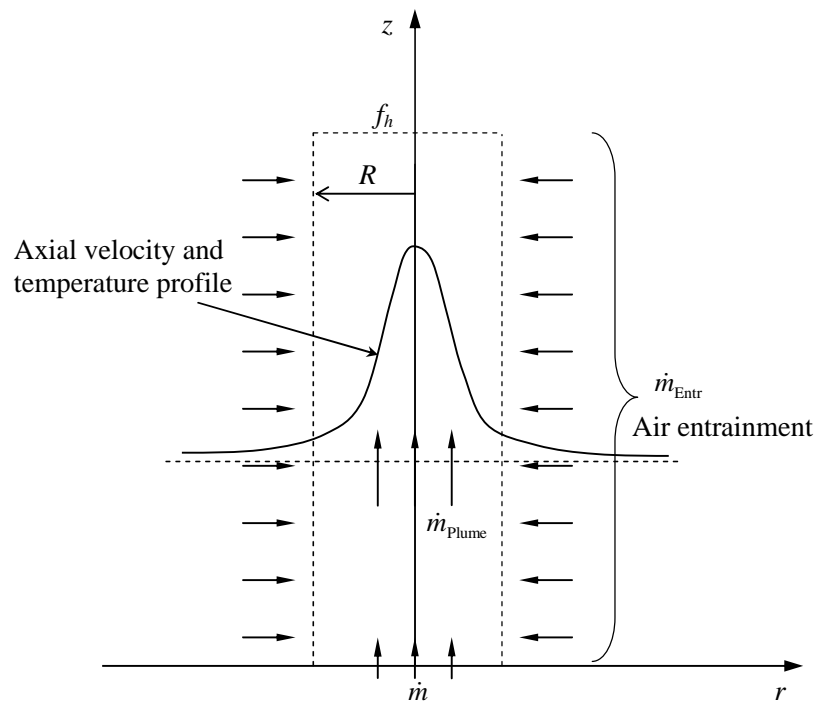

Fig. 3.4: High-speed rotating cylindrical diffusion plume of fire whirl

An IFW is a complex three-dimensional flow field and the surface of the flame has a helical structure. Within an average time, the flow field of the fire whirl can be taken as axi-symmetric.

Compared to a normal pool fire, the flame surface of an IFW is relatively stable without having large-scale eddies and low buoyancy. Centrifugal force and density gradient along the radial direction would give a stable condition. The flame surface of the IFW is smoother due to the stratification effect of turbulent flame. Mixing and

burning of fuel and air would reduce the flame diameter of fire whirl $R(z)$ axially, and then further reduced to the centre axis at the top part of the fire. However, the change in flame diameter is small in a fire whirl with a tall axial height. Hence the flame diameter $R(z)$ was assumed to be a constant R.

Similar to a turbulent fire plume, an IFW has different regions along the axial direction with different radius. Three zones were also observed for the IFW generated in the square vertical shaft with a sidewall corner gap as reported before[22]. Flame pictures observed from the experiments suggested that IFW can be assumed to be high-speed rotating cylindrical diffusion flame. Based on this observation, an axis of symmetry was taken along the vertical centreline with air entrained horizontally from all directions. This is only a simple approximation for easier mathematical analysis. More accurate results can be derived with additional assumptions. However, simple analytical expressions would be difficult and would require more experimental data.

The buoyant axi-symmetric plume mass flow rate $\dot{m}_{\text{Plume}}$ (in kg/s) at some height z above the fuel source in cylindrical coordinates (r, θ, z) can be derived as given in Equation (3.8), in terms of density ρ, axial velocity $V_z(z, r)$ and flame radius R which is also a function of z since it is similar to a fire plume.

$$\dot{m}_{\text{Plume}}(z) = \int_0^\infty (2\pi r)\rho V_z(z, r)\, \mathrm{d}r \approx \int_0^R (2\pi r)\rho V_z(z, r)\, \mathrm{d}r \qquad (3.8)$$

The plume mass flow would be increased steadily with height, since ambient air is continually entrained over the plume height. This mass consists of a mixture of combustion products and ambient air would be entrained into the plume, with most of

the mass from the ambient air entrained and only a small portion from the combustion

products. The plume mass flow rate at the mean flame height f_h can be derived by

Equation (9) as a sum of the burning rate $\dot{m}$ and the total air entrainment rate $\dot{m}_{Entr}$:

$$\dot{m}_{Plume}(z)\big|_{z=f_h} = \dot{m} + \dot{m}_{Entr} \approx \dot{m}_{Entr} \tag{3.9}$$

With $\dot{m}_{Entr}$ is given by Equations (3.10a) and (3.10b):

$$\dot{m}_{Entr} = \int_0^{f_h} \frac{\mathrm{d}\dot{m}_{Plume}}{\mathrm{d}z}\,\mathrm{d}z \tag{3.10a}$$

or

$$\dot{m}_{Entr} = \int_0^{f_h} \frac{\mathrm{d}}{\mathrm{d}z}\left[\int_0^R \rho V_z(2\pi r)\,\mathrm{d}r\right]\mathrm{d}z \tag{3.10b}$$

In this vertical shaft model, the rotation of buoyant flame above a gasoline pool is

induced by incoming tangential airflow from a sidewall corner gap. The total air

entrainment rate can be determined by Equation (3.11) in terms of the air velocity at

corner gap $V_d(z)$ and the width of sidewall corner gap d_g.

$$\dot{m}_{Entr} = \int_0^{f_h} d_g \rho_\infty V_d \,\mathrm{d}z \tag{3.11}$$

Equation (3.12) is the general form of the combustion reaction.

$$\nu_{Fuel}\ \text{Fuel} + \nu_{Air}\ \text{Air} \rightarrow \sum_i \nu_{Pro,i}\ \text{Products} \tag{3.12}$$

The numbers ν_i are the stoichiometric coefficients for the overall combustion process in which fuel reacts with air (oxygen) to produce a number of products. The stoichiometric Equation (3.12) implies that the mass consumption rates for fuel and oxidizer per unit volume ($\dot{m}'''_{Fuel}$ and $\dot{m}'''_{Air}$) are related to the molecular weights M_{Fuel} and M_{Air} as described by Equation (3.13).

$$\frac{\dot{m}'''_{Fuel}}{\nu_{Fuel} M_{Fuel}} = \frac{\dot{m}'''_{Air}}{\nu_{Air} M_{Air}} \tag{3.13}$$

The stoichiometric air-fuel ratio s is defined by Equation (14) as:

$$s = \frac{\nu_{Air} M_{Air}}{\nu_{Fuel} M_{Fuel}} \tag{3.14}$$

Assuming that a constant proportion γ of entrained fresh air would react with fuel in flame, the burning rate $\dot{m}$ (in kg/s) can be determined by Equation (3.15) as:

$$\dot{m} = \frac{\gamma \, \dot{m}_{Entr}}{s} \tag{3.15}$$

If the burning rate $\dot{m}$ and effective heat of combustion $\Delta H_{c,\,eff}$ are known, the heat release rate $\dot{Q}$ (in kW) of a pool fire can be calculated[23] by Equation (3.16):

$$\dot{Q} = \dot{m} \Delta H_{c,\,eff} (1 - e^{-k\beta D}) \tag{3.16a}$$

Substituting Equation (3.15) into Equation (3.16a) and since the air above the flame height will not burn with the fuel, $\dot{Q}$ can be evaluated by Equation (3.16b) or (3.16c).

$$\dot{Q} = \frac{\gamma}{s} \dot{m}_{\text{Entr}} \Delta H_{c,\text{eff}} (1 - e^{-k\beta D})$$

(3.16b)

or

$$\dot{Q} = \frac{\gamma}{s} \Delta H_{c,\text{eff}} (1 - e^{-k\beta D}) d_g \rho_\infty \int_0^{f_h} V_d \, \mathrm{d}z$$

(3.16c)

If the distribution of the velocity $V_d(z)$ is known, then the relation between heat release rate $\dot{Q}$, width of corner gap d_g and flame height f_h can be estimated. Several assumptions were made and justified in the following section.

Although the combustion of an IFW is very fast, the gas-production rate of liquid fuel combustion is much smaller than air entrainment rate and can be neglected. In comparing with the free plume for burning a gasoline pool fire in open space, plume mass flow rate of the gasoline pool fire in this test was calculated to be about 3.51 kg/s. Burning rate of the gasoline pool fire of diameter 0.46 m is 0.0029 kg/s. Therefore, the burning rate of gasoline pool fire burning in open air is much lower than plume mass flow rate. For the developed IFW of diameter 0.46 m, the fuel consumption rate increased to 0.0192 kg/s, which is still less than 3.51 kg/s for a free plume. The fire whirl has a strong entrainment effect to draw much more ambient air than a free plume. Therefore, burning rate of fuel in an IFW is much less than the air entrainment rate for a stable IFW.

Further, the dimensional heat release rate (mass burning rate) was assumed to be unchanged with gap distance. From the earlier results [22], transient burning duration

31

and the mean flame height of the IFW were roughly the same when sidewall corner width was lying between 0.3 and 0.5 m. The burning duration was about 190 s to 210 s when an IFW was created. This change is very small compared to the burning duration in open air. It is acceptable to assume the mass burning rate to be unchanged with gap distance when a strong IFW was generated.

3.4 Air entrainment velocity

Three models of air entrainment, corresponding to three different assumptions on variation of air entrainment velocity along the radial direction V_d with height z, were considered in this study. It has been tried before that considering the air velocity alone the whole gap will not provide a well fitted result, thus the air velocity should be studied up to the flame height. The first model as given in Equation (3.17), take V_d as a constant up to the flame height f_h and then at zero above that:

$$V_d = \begin{cases} V_0 & z \le f_h \\ 0 & z > f_h \end{cases} \tag{3.17}$$

Substituting Equation (3.17) into Equation (3.16c), $\dot{Q}$ can be determined by Equation (3.18) in terms of the fuel tray diameter D (in m), corner gap width d_g (in m), empirical constant $k\beta$ (m^{-1}), mean flame height f_h (in m), effective heat of combustion $\Delta H_{c,eff}$ (in kJkg^{-1}), ρ_∞, constant air velocity at corner gap V_0 (in ms^{-1}), constant proportion entrained fresh air which reacts with fuel γ, stoichiometric air-fuel ratio s.

$$\dot{Q} = \frac{\gamma}{s} V_0 \rho_\infty \Delta H_{c,eff} (1 - e^{-k\beta D}) f_h d_g \tag{3.18}$$

A dimensionless flame height f_h^* (in terms of D), and a dimensionless gap width d_g^* (in terms of vertical shaft width a) are respectively defined by Equations (3.19a) and (19b).

$$f_h^* = \frac{f_h}{D} \qquad (3.19a)$$

$$d_g^* = \frac{d_g}{a} \qquad (3.19b)$$

Then Equation (3.20) can be derived for determination of $\dot{Q}^*$.

$$\dot{Q}^* = K_1 f_h^* d^* \qquad (3.20)$$

where K_1 is a constant given by Equation (3.21).

$$K_1 = V_0 a D \frac{\gamma}{s} \frac{\Delta H_{c,\text{eff}} (1 - e^{-k\beta D})}{c_{p,\infty} T_\infty \sqrt{gD} D^2} \qquad (3.21)$$

Assume $\dot{Q}^*$ is constant once an IFW with vigorous swirling is generated. Then Equations (3.22a) and (3.22b) can be applied.

$$f_h^* d_g^* = \text{constant} \qquad (3.22a)$$

or

$$\ell n f_h^* + \ell n d_g^* = \text{constant} \qquad (3.22b)$$

The second model assumes that V_d is constant below the flame height but varies with $1/z^{\alpha_1}$ at height z above the flame height as given in Equation (3.23).

$$V_d = \begin{cases} V_0 & z \leq f_h \\ \dfrac{V_0}{z^{\alpha_1}} & z > f_h \end{cases} \qquad (3.23)$$

The heat release rate can be defined by Equation (3.24);

$$\dot{Q} = \begin{cases} \dfrac{\gamma}{s} \rho_\infty \Delta H_{c,\text{eff}} (1 - e^{-k\beta D}) V_0 f_h d_g & z \leq f_h \\ \dfrac{\gamma}{s} \rho_\infty \Delta H_{c,\text{eff}} (1 - e^{-k\beta D}) \dfrac{V_0}{1-\alpha_1} f_h^{(1-\alpha_1)} d_g & z > f_h \end{cases} \qquad (3.24)$$

and in Equation (3.25) in dimensionless form.

$$\dot{Q}^* = \begin{cases} K_1 f_h^* d_g^* & \dfrac{z}{D} \leq f_h^* \\ K_2 (f_h^*)^{1-\alpha_1} d_g^* & \dfrac{z}{D} > f_h^* \end{cases} \qquad (3.25)$$

where K_2 is a constant given by Equation (3.26).

$$K_2 = \frac{V_0}{1-\alpha_1} a D^{(1-\alpha_1)} \frac{\gamma}{s} \frac{\Delta H_{c,\text{eff}} (1 - e^{-k\beta D})}{c_{p,\infty} T_\infty \sqrt{gD} D^2} = \frac{D^{-\alpha_1}}{1-\alpha_1} K_1 \qquad (3.26)$$

Assume $\dot{Q}^*$ is constant once an IFW was generated as given in Equation (3.27). Then $f_h^* d_g^*$ is constant with a relation similar to Equation (3.22b):

$$\begin{cases} \ell nf_h^* + \ell nd_g^* = \text{constant} & \dfrac{z}{D} \le f_h^* \\[2mm] (1-\alpha_1)\ell nf_h^* + \ell nd_g^* = \text{constant} & \dfrac{z}{D} > f_h^* \end{cases} \tag{3.27}$$

The third model of Equation (3.27) assumes that V_d is proportional to power α_3 of z

(z^{α_3}) as in studying wind effects,[6] though there is no clear theoretical basis:

$$V_d = A\,z^{\alpha_3} \tag{3.28}$$

The heat release rate can be determined by Equation (3.29);

$$\dot{Q} = \frac{\gamma A}{s(\alpha_3+1)}\rho_\infty \Delta H_{c,\text{eff}}(1-e^{-k\beta D})f_h^{\alpha_3+1}d_g \tag{3.29}$$

and Equation (3.30) in dimensionless form.

$$\dot{Q}^* = K_3(f_h^*)^{\alpha_3+1}d_g^* \tag{3.30}$$

where K_3 is a constant as given by Equation (3.31).

$$K_3 = \frac{AaD^{\alpha_3+1}}{\alpha_3+1}\frac{\gamma}{s}\frac{\Delta H_{c,\text{eff}}(1-e^{-k\beta D})}{c_{p,\infty}T_\infty\sqrt{gD}D^2} \tag{3.31}$$

Assume $\dot{Q}^*$ is constant once an IFW is generated. Then Equation (3.32) is derived.

$$(\alpha_3+1)\ell nf_h^* + \ell nd_g^* = \text{constant} \tag{3.32}$$

35

Under the three different models or assumptions described above, Equation (3.33) is obtained:

$$\alpha \, \ell n f_h{}^* + \ell n d_g{}^* = \text{constant} \tag{3.33}$$

where α is a constant.

In all three models for air entrainment proposed above, the plot of $\ell n f_h{}^*$ against $\ell n d_g{}^*$ should give a straight line if an IFW is created. However, no IFW was observed if d_g is too large or too small (gap too wide or too narrow). Thus another assumption based on physical observation would be needed.

3.5 Derive of correlation between Flame height and corner gap width

The flame height f_h can be estimated from Equation (3.16c), if the velocity distribution $V_d(z)$ is known. However, the detailed distribution of the velocity $V_d(z)$ is difficult to determine accurately from experiment. In view of this and also due to limitation in resources, $V_d(z)$ was not measured in this study. Rather, the computational fluid dynamics (CFD) software, Fire Dynamics Simulator (FDS), was used to determine $V_d(z)$ the vertical shaft model as shown in Fig. 1. A gasoline pool fire of tray diameter 0.46 m and sidewall corner gap 0.35 m was simulated. Grid distribution is shown in Fig. 3.5, the size of coarse mesh was 5.0 cm, and that of fine mesh was 2.5 cm.
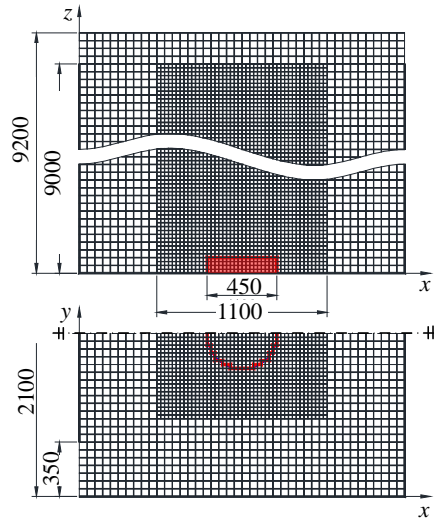
36

Fig. 3.5: Grid distribution in FDS for a gasoline pool fire of tray diameter 0.46 m

and sidewall corner gap 0.35 m

A mixture fraction combustion model is incorporated in the FDS. The model assumes that combustion is mixing-controlled, and that the reaction of fuel and oxygen is infinitely fast.

Table 3.2 Characteristic length D* and cell size of different HRR in experiment

Test	Diameter of Fuel tray D(m)	HRR (kW)	cell size x (cm)	D*				D*/x			
				HRRx1	HRR x 0.9	HRR x 0.8	HRR x 0.7	HRRx1	HRR x 0.9	HRR x 0.8	HRR x 0.7
Free burning	0.46	247.3	2.5	0.55	0.528	0.503	0.477	22	21.12	20.12	19.08
Stage I	0.46	253.9	2.5	0.556	0.534	0.508	0.481	22.24	21.36	20.32	19.24
Stage II	0.46	355	2.5	0.636	0.61	0.582	0.551	25.44	24.4	23.28	22.04
Stage IV	0.46	473.4	2.5	0.713	0.684	0.653	0.619	28.52	27.36	26.12	24.76

Test	Diameter of Fuel tray D(m)	HRR (kW)	cell size x (cm)	D*				D*/x			
				HRRx1	HRR x 0.9	HRR x 0.8	HRR x 0.7	HRRx1	HRR x 0.9	HRR x 0.8	HRR x 0.7
Free burning	0.46	247.3	5	0.55	0.528	0.503	0.477	11	10.56	10.06	9.54
Stage I	0.46	253.9	5	0.556	0.534	0.508	0.481	11.12	10.68	10.16	9.62
Stage II	0.46	355	5	0.636	0.61	0.582	0.551	12.72	12.2	11.64	11.02
Stage IV	0.46	473.4	5	0.713	0.684	0.653	0.619	14.26	13.68	13.06	12.38

The parameter of mixture fraction in FDS was used to show air/fuel ratio. The value of the mixture fraction was equal to 1 in a region corresponding to burning of pure

fuel while the value equal to 0 corresponds to pure oxidized air was thus generated, leading to a stoichiometric value that is typically very small, less than 0.1.

The flame height could be defined assuming that the tip of the fire is the point where the mixture fraction reaches its stoichiometric value [43]. The mixture fraction level 0.05 in FDS was used to define an iso-surface for a fire in this study, this value suggested by previous researcher [43]. Considering the characteristic length D*[53], which is given as:

$$D^* = \left(\frac{\dot{Q}}{\rho c T \sqrt{g}} \right)^{\frac{2}{5}}$$

(3.34)

where ρ, c, T and g are the air density, air thermal capacity, ambient air temperature and gravitational acceleration respectively.

In considering D* and the size of the cell x used in FDS, Table 3.2 tabulates the HRR at different stages and the characteristic length D* as well as the cell size x. Normally, the ratio of D*/x should be lying between 4 and 16 [54], the higher the value means a more fine simulation. Thus, it can be seen that for the finer grid size of the FDS simulation, which is 2.5 cm grid size, the D*/x ratio is higher than the said range and hence showing that a better result will be obtained. The predicted transient flame heights are shown in Fig. 3.6. For gasoline pool fire of tray diameter 0.46 m and vertical gap width 0.33 m, the mean flame height predicted by FDS was 3.25 m, which was very close to the experiment result of 3.2 m.
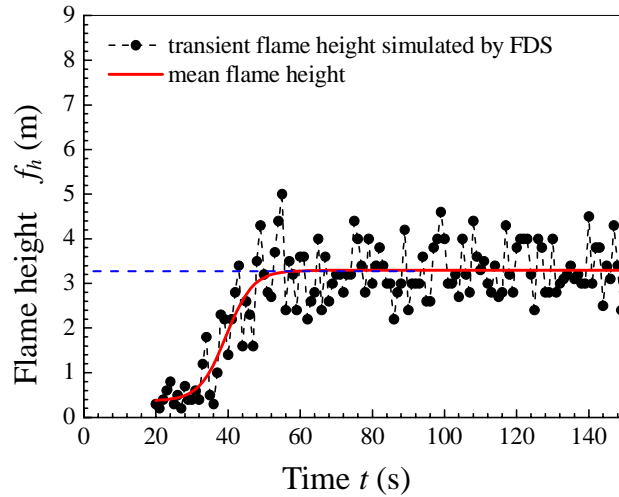
Fig. 3.6: Flame height simulated by FDS for a gasoline pool fire of tray diameter 0.46 m and sidewall corner gap 0.35 m

Air entrainment velocities along the radial direction $V_d(z)$ predicted by FDS are shown in Fig. 3.7. As shown in Fig. 3.7(a), distribution of entrainment velocity at different height along the horizontal direction was uniform. Vertical distribution of velocity at vertical center line of corner gap can be divided into two zones: flame zone and plume zone as in Fig. 3.7(b). In the flame zone, the velocity $V_d(z)$ was roughly a constant V_0 for tray diameter 0.46 m and sidewall corner gap 0.35 m.

Coordinate at corner gap y (m)
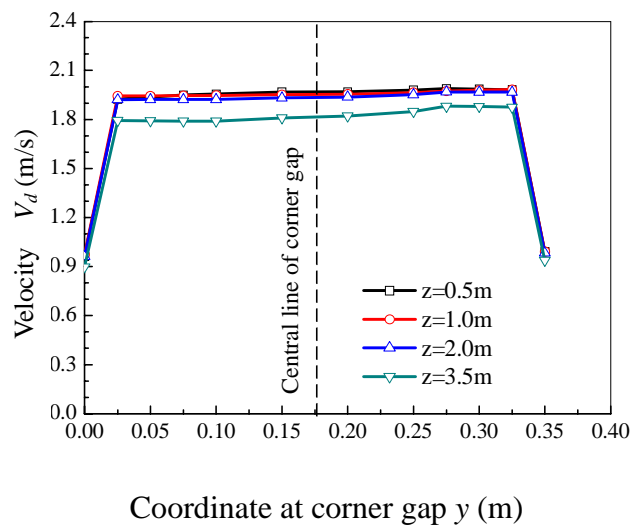
(a) Horizontal distribution of velocity at different height
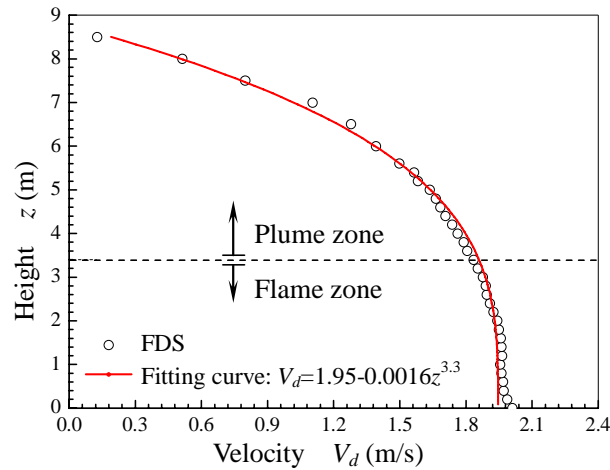
(b) Vertical distribution of velocity at centre line of corner gap

Fig. 3.**7: Air velocity at corner gap induced by fire plume**

As shown in Fig. 3.7(a), distribution of entrainment velocity at different height along the horizontal direction was uniform. Vertical distribution of velocity at vertical centre line of corner gap can be divided into two zones: flame zone and plume zone as in Fig. 3.7(b). In the flame zone, velocity $V_d(z)$ was roughly a constant V_0 for tray diameter 0.46 m and sidewall corner gap 0.35 m.

Since there is no big enough computer system capable of doing the simulations with more refining girds, 5cm grid is used to capture the boundary layer effect. The boundary layer effects could still be observed as air speed was very low on both sides of the slit, as shown in Fig. 3.7(a).

Since CFD might not simulate combustion well, it is assumed there was no flame and combustion reaction in the upper smoke zone due to reduction in buoyancy, a reduction in the vertical distribution of velocity at the centre line occurred, as shown in Fig. 3.7(b).

As observed from experiments [22] in the vertical shaft model, an IFW would be generated only when d_g was lying between a lower limit d_{gl} and an upper limit d_{gu}. Peak flame height was observed at a value d_{go}. Therefore, Equation (3.35a) is proposed to modify expression (3.22a) on $f_h^* d_g^*$.

$$f_h^* X = \text{constant} \tag{3.35a}$$

where X is a dimensionless parameter given by Equation (3.35b).

$$X = \begin{cases} \dfrac{d_g}{a} & d_{gl} < d_g \leq d_{go} \\ \dfrac{2d_{go} - d_g}{a} & d_{go} < d_g \leq d_{gu} \end{cases} \tag{3.35b}$$

Fig. 3.8 shows the plot of $\ell n f_h^*$ against X for fuel tray diameter D of 0.46 m in the 9-m tall shaft model [22]. A fitted line with correlation coefficient of 0.9995 was obtained, indicating a high degree of correlation as given by Equation (3.36).

$$\ell n f_h^* = 1.77349 + 0.31187 \ell n X \tag{3.36}$$

Equation (3.36) was obtained by line fitting using experimental data from reference [22]. The goodness of fit (high correlation coefficient) shows that the relation between $\ell n f_h^*$ and $\ell n X$ is linear. Thus the linear relation between $\ell n f_h^*$ and $\ell n X$ shown in Equation (3.35b) was from $\ell n d_g^*$ in Equation (3.22b) and experimental observation; having a gap width not too narrow nor too wide, as obtained by theoretical analysis, and supported by experimental results.
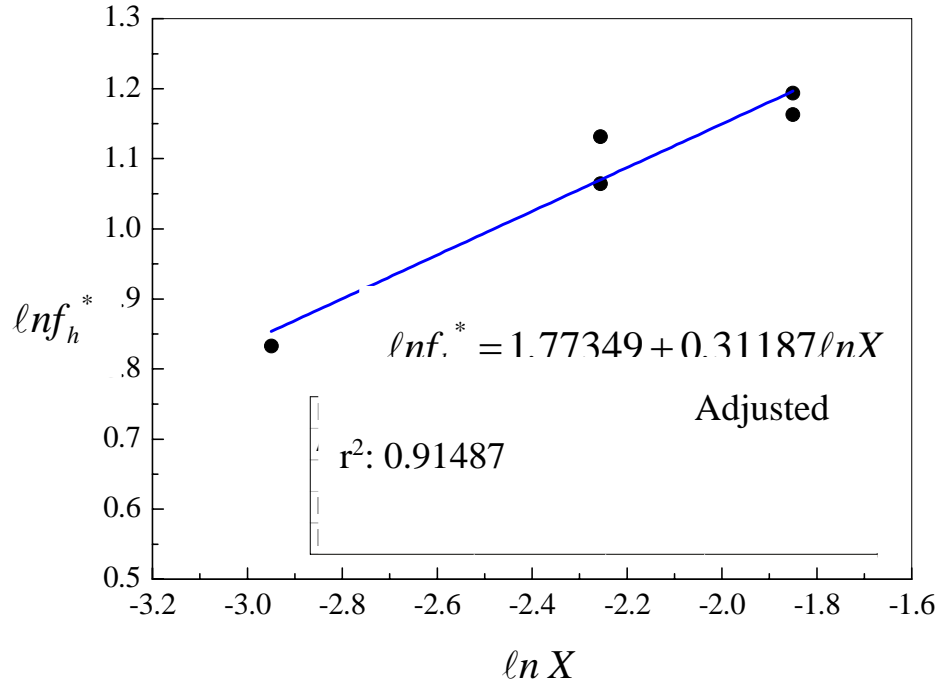
$$\ell nf.^* = 1.77349 + 0.31187\ell nX$$

Adjusted

$r^2: 0.91487$

Fig. 3.8: Correlation of flame height with parameter X

If the distribution of the velocity $V_d(z)$ is known (see Equation (3.16c)), then the relation between heat release rate $\dot{Q}$, width of corner gap d_g and flame height f_h can be estimated without making assumption on velocity. Equation (3.22a) or Equation (3.22b) shows a correlation between dimensionless flame height f_h^* and dimensionless corner gap d_g^*.

Experimental data in Fig. 3.8 were summarized for each test [22] The data are adequate to determine the correlation expression from experimental observation, pointing out an approach to further study. Also, for further verifying the result, the measurement of air velocity alone the gap in experiment should be done.

Chapter 4.

Observation of Internal Fire Whirl Using High Speed Camera

In a vertical shaft with a corner gap, the gap width affects the ventilation and hence the air supply rate to the fire, which changes the burning rate. Once the burning rate is changed, the hydrodynamics induced by the fire is also changed, giving swirling flame characteristics. A correlation expression of the IFW flame height in a 9-m tall vertical shaft with corner gap width has been discussed in Chapter 3.

Swirling flame patterns were observed using a high-speed camera in this chapter. Flame heights measured were compared with those observed from a normal camera. As a high-speed camera can provide more details in the development of swirling flame patterns, it is possible to identify different stages of IFW development more accurately.

4.1 Experimental setup and study

A vertical shaft model used was of section 35 cm by 34 cm (with the gap) and height 145 cm, as shown in Fig. 4.1(a). The model was made of wood with a transparent plastics sheet for observing the flame shape and taking pictures.

A 1.6-kW pool fire of diameter D of 7 cm and containing 25 ml propanol was placed on the ground at the centre of the shaft model. The burning time t_B (in s) for the same pool fire in outside air was about 400 s. The average heat release rate was 1.6 kW with maximum flame height of 40 cm and average flame height of 20 cm while burning the pool fire outside.

43

There were 18 tests labeled T1 to T18 with different gap widths d_g (in cm) of values 0.0 cm (gap closed), 1.0 cm, 2.0 cm, 3.0 cm, 4.0 cm, 4.3 cm, 6.8 cm, 8.5 cm, 10.0 cm, 11.5 cm, 12.8 cm, 14 cm, 16 cm, 17 cm, 18.4 cm, 20 cm, 23 cm and 34 cm (gap fully opened, that is, with one wall was removed) respectively. The ratio d_g/a of gap width d_g to wall width a (of 34 cm) lies between 0 and 1. A summary of the 18 tests is shown in Table. 2.

The burning time of the propanol pool fire varied from 144 s to 400 s, depending of gap width.
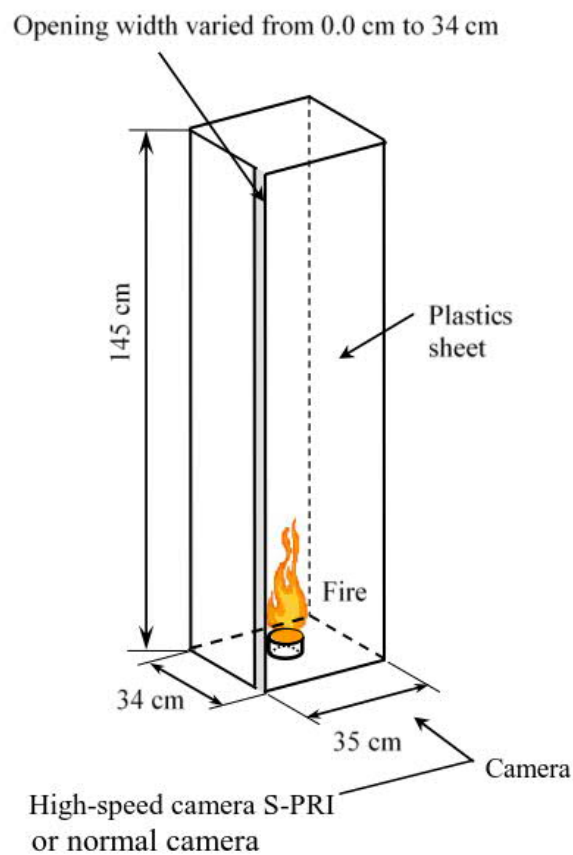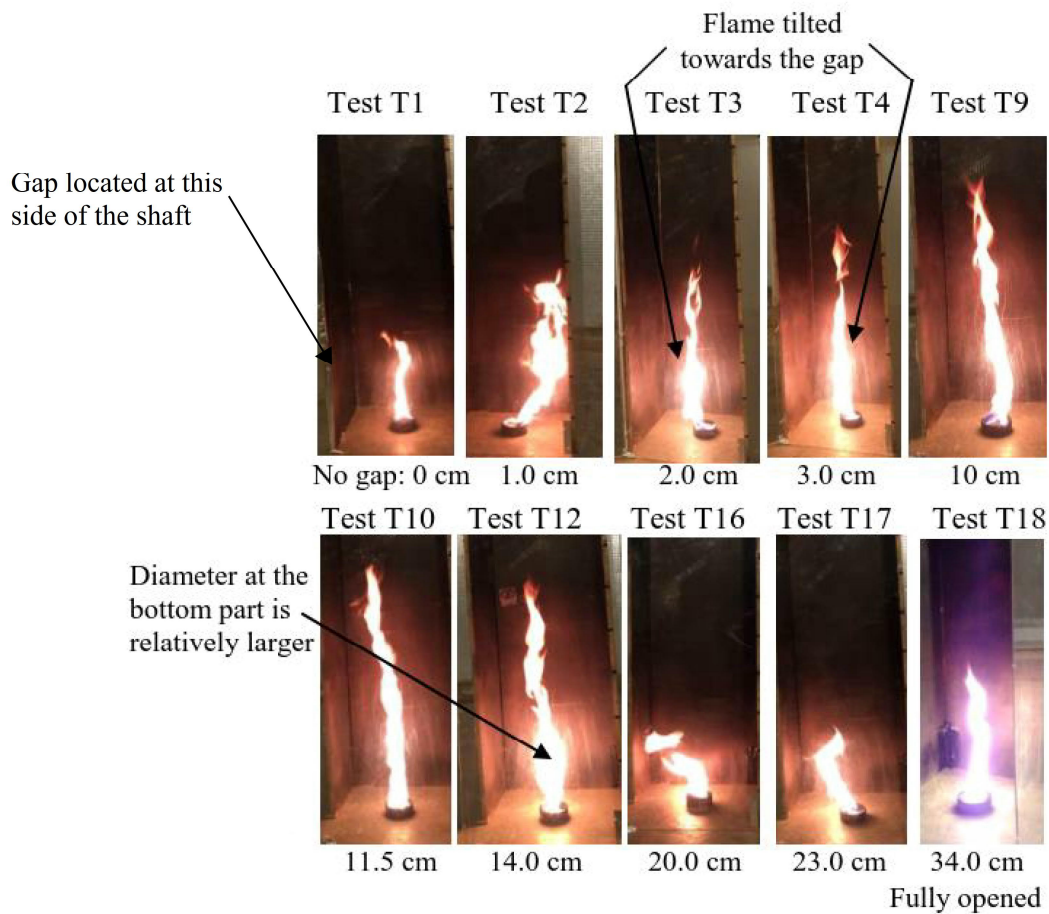

Fig. 4.1a The vertical shaft model

44

Fig 4.1b Flame height taken using a normal camera

4.2 Observation Using Normal Camera

Videos and photographs were taken using a normal digital camera through the transparent surface for each test to determine the flame lengths of the propanol pool fire in the vertical shaft under different corner gap widths.

The flame shapes during steady burning for some of the 18 tests are shown in Fig. 4.1(b). For pool fire in the shaft model with no corner gap, flame did not swirl. The flame behaved in a manner similar to that of a pool fire in free space.

In the case of 1-cm gap opening, the amount of air that could be entrained into the shaft was relatively small and no IFW was formed. However, the flame revolved in counterclockwise direction as shown in photographs and video captured using a normal camera (Fig. 4.2).

(sequence of photographs taken starting from left to right)
(a) Captured from a normal camera
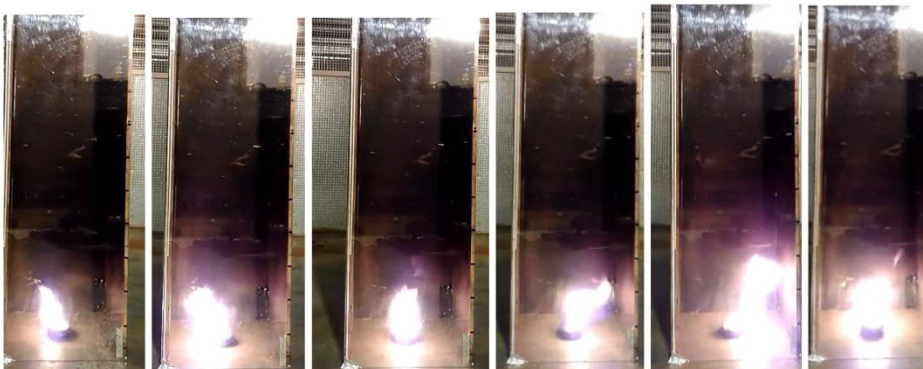
(sequence of photographs taken starting from left to right)
(b) Captured from video

Fig. 4.2: Flame revolved in counterclockwise direction for test T2 with 1-cm gap width

Table 4.1: Results for the tests with different gap width

Parameters / Test No.	Vertical gap Width d_g / cm	Vertical gap width ratio d_g / a	Burning time t_B / s	Fire whirl generated (Y/N?)	Stable IFW (Y/N?)	Fire whirl start time / s	Fire whirl duration / s	Maximum flame height f_{max} / cm	Average flame height f_h / cm	Average mass loss rate over t_B $\dot{m}_{av1}$ / g/s	Average mass loss rate over fire whirl $\dot{m}_{av2}$ / g/s	Average mass loss rate by measuring transient mass $\dot{m}_{av3}$ / g/s
T1	0.0	0	380	N	N	-	0	40	20	0	-	-
T2	1.0	0.03	252	NA	N	-	NA	50	25	0.029	-	-
T3	2.0	0.06	150	Y	Y	15	130	80	55	0.131	0.151	0.124
T4	3.0	0.09	144	Y	Y	9	130	85	65	0.136	0.151	0.125
T5	4.0	0.12	150	Y	Y	6	140	85	65	0.131	0.140	0.136
T6	4.3	0.13	150	Y	Y	8	140	85	65	0.131	0.140	0.133
T7	6.8	0.20	155	Y	Y	6	145	80	60	0.127	0.135	0.121
T8	8.5	0.25	180	Y	Y	6	160	75	55	0.109	0.123	0.114
T9	10	0.29	180	Y	Y	7	160	70	55	0.109	0.123	0.098
T10	11.5	0.33	180	Y	Y	5	160	65	50	0.109	0.123	0.096
T11	12.8	0.38	180	Y	Y	5	160	65	45	0.109	0.123	0.070
T12	14	0.42	180	Y	Y	6	160	60	40	0.109	0.123	0.069
T13	16	0.46	180	Y	Y	6	160	60	40	0.109	0.123	0.061
T14	17	0.50	250	NA	N	-	NA	55	30	0.079	-	-
T15	18.4	0.54	300	NA	N	-	NA	50	25	0.065	-	-
T16	20	0.58	360	N	N	-	0	45	22	0.055	-	-
T17	23	0.67	395	N	N	-	0	40	20	0.050	-	-
T18	34	1	400	N	N	-	0	40	20	0.049	-	-

Note: NA indicates there might be unstable fire whirl with short duration

As the gap width increased to 2 cm and 3 cm in tests T3 and T4, an IFW was formed. In addition, the flame tilted slightly towards the gap opening as shown in Fig. 4.2(b). Regarding the cases with gap width of 4 cm to 10 cm, an IFW was also formed. The IFW was much stable as the flame kept rotating about the central axis and did not appear to tilt to other directions.

Compared to the IFW formed in the cases with gap width of 4 cm to 10 cm, the IFW formed in the cases with gap width of 11.5 cm to 16 cm was slightly less stable as it again tilted towards the gap opening. Moreover, the flame diameter at the lower part of the IFW was slightly larger as shown in Fig. 4.2(b).

The flame tilted towards the gap for d_g of 2 cm to 3 cm in tests T3 and T4 because the IFW was not stable enough and so affected by incoming air movement from the gap. The larger flame diameter at the lower part of the IFW for tests with larger gap width because it allowed more air to enter the shaft model to support more vigorous combustion.

There are three types of flame characteristics observed for the different gap widths:
- No fire whirl was observed and flames moved round occasionally about a vertical axis for the tests with an opening width over 19 cm or less than 1 cm.
- Swirling motions were observed for a short time or unstable fire whirls were created for the tests with an opening width from 1 cm to 2 cm, and from 16 cm to 19 cm.
- Stable internal fire whirls were observed for the tests with an opening width from 2 cm to 16 cm, or d_g/a ratio from 1/17 to 8/17.

When the corner gap width increased beyond 16 cm, both flame rotation and precession were weakened. The pool fire behaved as that in free space again when the gap width was bigger than 19 cm.

For gap width half the width of the shaft model (that is, width of 17 cm or d_g/a of 0.5), more air was entrained into the shaft model. This would disturb the stable IFW motion. Therefore, 17 cm is a critical value beyond which the IFW inside the shaft would

become unstable or even disappear.

4.3 Observation using high-speed camera

The behavior and flame shape of the IFW was also observed using a high-speed camera which is able to take up to 1000 frames per second (fps). A normal camera cannot capture the fast whirling of flame because it took much less than 1 s for one revolution of the IFW. Moreover, a maximum of 2700 pictures can be stored for each test using high-speed camera. The flame shape observed was found to depend on gap widths.

A high-speed camera was used to take photographs for test T10. Two tests were conducted in the shaft with a 11.5-cm vertical gap width:

- Test T10h1: 250 fps for 2700 frames with testing duration of 10.8 s (high-speed camera)

- Test T10h2: 60 fps for 2700 frames with testing duration of 45 s (normal camera)

For easy comparison of the flame shape, 105 (15×7) frames with test duration of 105/250=0.42 s are put in one graph for T10h1, each frame of time interval ($\frac{0.42}{105}$)s or 0.004 s. For test T10h2, test duration of 105/60=1.75 s, with each frame of time interval of ($\frac{1.75}{105}$)s or 0.0167 s are put in one graph.

The captured pictures for test T10h1 by 250 fps are shown in Fig. 4.3 (3.66 s to 4.08 s) with 105 frames of time interval of 0.004 s.

Some photos at the transition stage (to tall flame height) and steady burning stage for test T10h2 are shown in Fig. 4.4 (the transition from randomly revolving to flame swirling 14 s to 15.75 s). The critical time periods at transition from randomly swinging flame to a fire whirl are from 23.25 s to 25.00 s and from 25.00 s to 26.75 s. The following were observed from the captured pictures for the two tests:

- Test T10h1: about 2.5 revolutions per second (rps) with 90 frames for 1 revolution before generating the fire whirl.

- Test T10h2: about 2 rps with 30 frames for 1 revolution before generating the fire whirl.

The swirling rate was about 2 rps to 2.5 rps before going to the steady fire whirl stage in the shaft model with a vertical gap of 11.5 cm. The whirl rate was faster than 3 rps for steady fire whirl stage.

It is difficult or even impossible to observe the fire whirls within one revolution with a normal speed camera as shown in the above figures. However, one common point for all the IFW is that the IFW flame rotated in counterclockwise direction as the air was entrained inside the shaft through the gap which created a counterclockwise circulation of air inside the shaft and generated the IFW in this direction.

Pictures for tests at 25 s, 50 s, 100 s and 150 s by a high-speed camera were compared with those by a normal camera in Fig. 4.5. It is observed that there are two flame vortex tubes as in Fig. 4.5(b) and 4.5(c). The observed pattern was enlarged in Fig. 4.6 to show two vortex tubes moving over the horizontal pool surface as in Fig. 4.6(b). A schematic of vortex lines in a thermal plume in rotation was also suggested [55].

From the observation above, more developed detailed schematic diagrams based on Fig 3.3 can be drawn as shown in Fig 4.7. It is observed that while increasing the corner gap width to an appropriate value (with d_g/a ratio from 1/17 to 8/17) in this model, a steady fire whirl would be developed in a sequence of stages as in Fig. 4.7. A fire plume was formed initially as in Fig. 4.7(a), flame tilted with revolution about the central pool fire axis as in Fig. 4.7(b), rotation (or self-spinning) with precession started about the tilted flame axis with two vortex tubes as in Fig. 4.7(c), further tilted as in Fig. 4.7(d) with revolution at an angle θ_2 to vertical axis. Then θ_2 decreased as in Fig. 4.7(e), a vertical flame part formed as in Fig. 4.7(f), and eventually an IFW formed as in Fig. 4.7(g). The two vortex tubes were observed as shown in the figure. The motion of the vortex tubes can be further explained using the theory proposed by Church et al. [56].

A primary anchoring zone (PAZ) above a pool fire was observed by Venkatesh et al. [57]. Using video camera of 30 frames per second, flame shapes of an IFW of 5-cm diameter pool fire was also observed by Chuah and Kushida [47] to have some air regions above the burning fuel surface. An air region was observed in an IFW from a 5-cm diameter methanol pool fire by Chuah et al. [48]. Spinning of flame base of a 3-cm diameter ethanol pool fire would give higher burning rate as reported by Kuwana et al. [58]. There was also an air region observed, though the flame vortex tubes could not be seen clearly.

The maximum flame heights f_{max} (in cm) and average flame height f_h (in cm) are shown in Table. 4.1.

Fig. 4.3: Test T10h1 at time 3.66 s to 4.08 s (duration of 0.42 s for 105 frames), frame interval 0.004 s captured using a high-speed camera
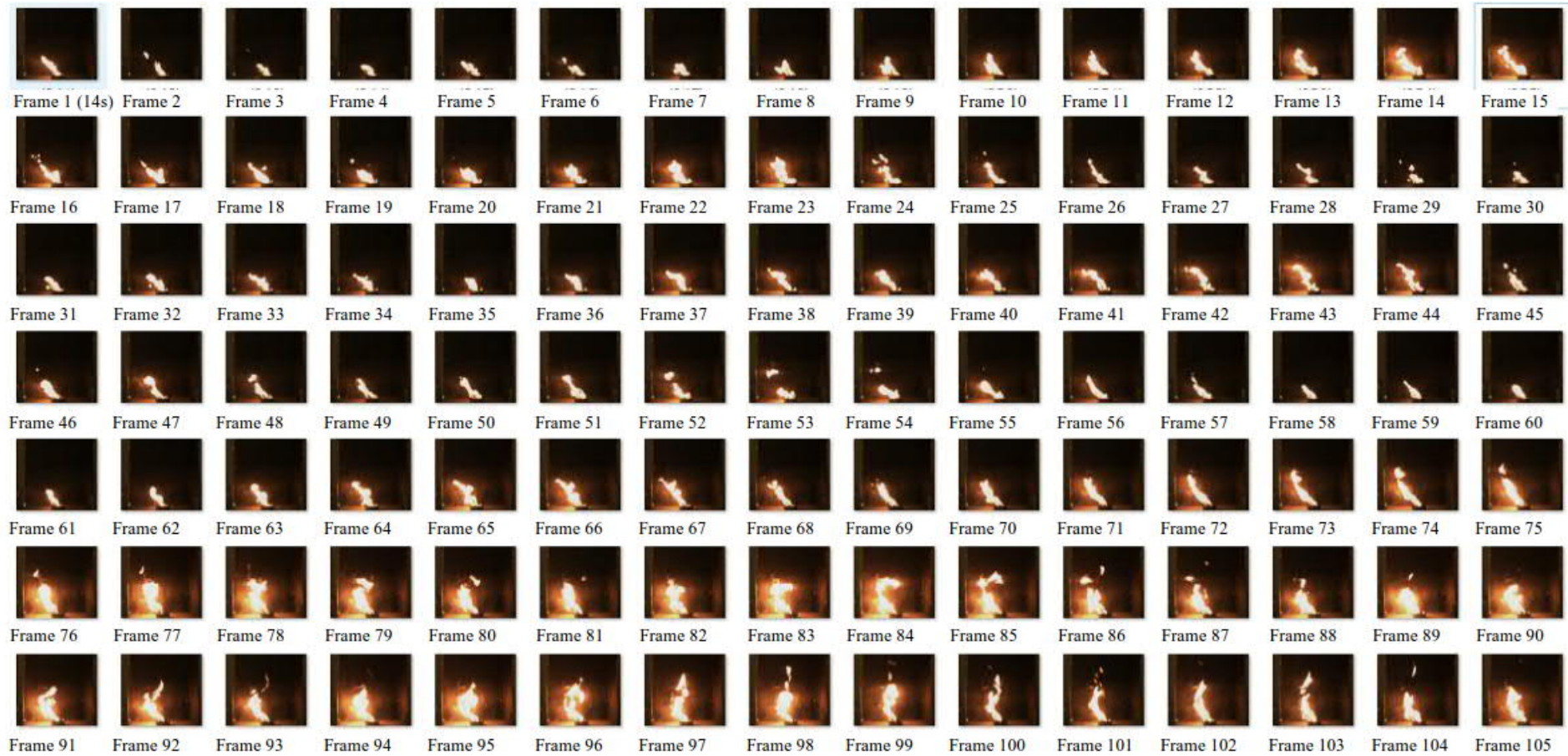
Fig. 4.4: Test T10h2 from 14 s to 15.75 s (duration of 1.75 s for 105 frames), frame interval 0.0167 s captured using a high-speed camera
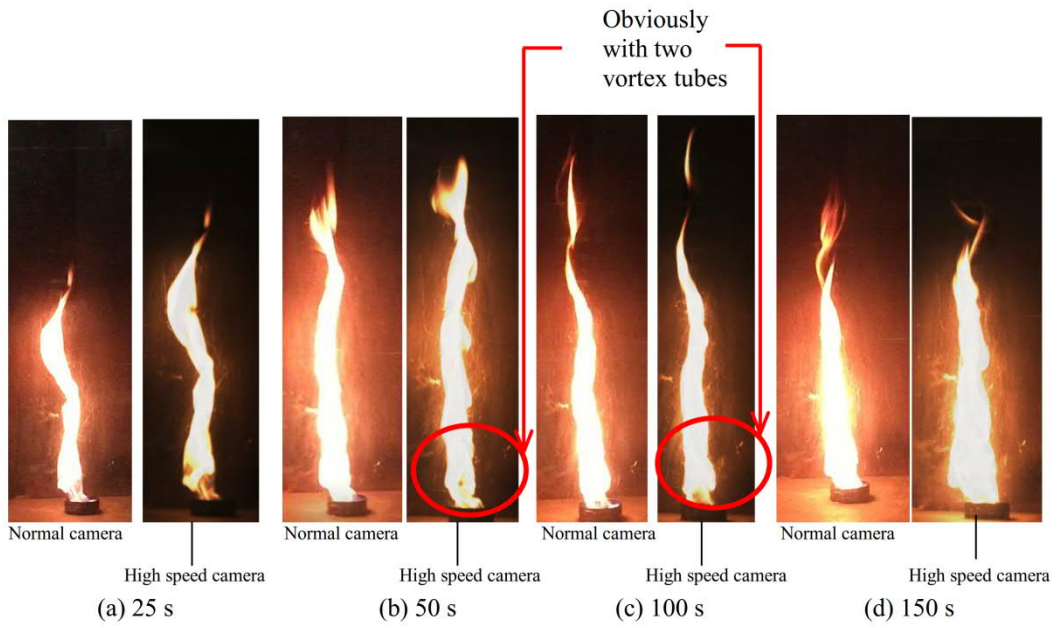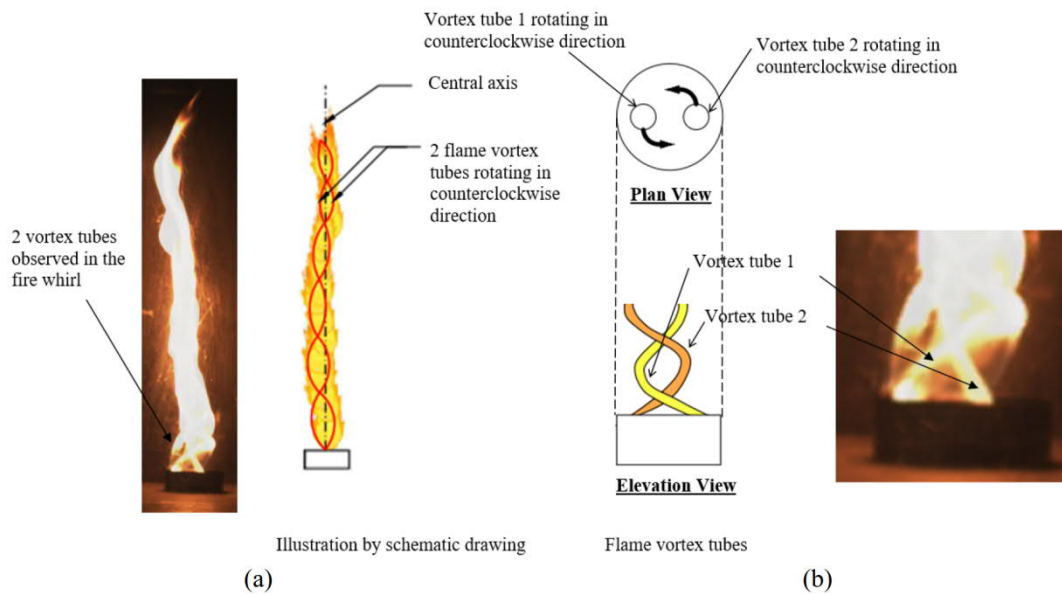
Normal camera   High speed camera   Normal camera   High speed camera   Normal camera   High speed camera   Normal camera   High speed camera

(a) 25 s   (b) 50 s   (c) 100 s   (d) 150 s

Fig 4.5 Pictures from a normal camera and a high-speed camera in test T10

Vortex tube 1 rotating in
counterclockwise direction

Vortex tube 2 rotating in
counterclockwise direction

Central axis

2 flame vortex
tubes rotating in
counterclockwise
direction

Plan View

2 vortex tubes
observed in the
fire whirl

Vortex tube 1

Vortex tube 2

Elevation View

Illustration by schematic drawing

Flame vortex tubes

(a)   (b)

(a) Photograph taken by a high-speed camera at 45 s

(b) Enlarged high-speed camera photgraph showing the rotating flame vortex tube

Fig 4.6 Flame core observed in an IFW using a high speed camera
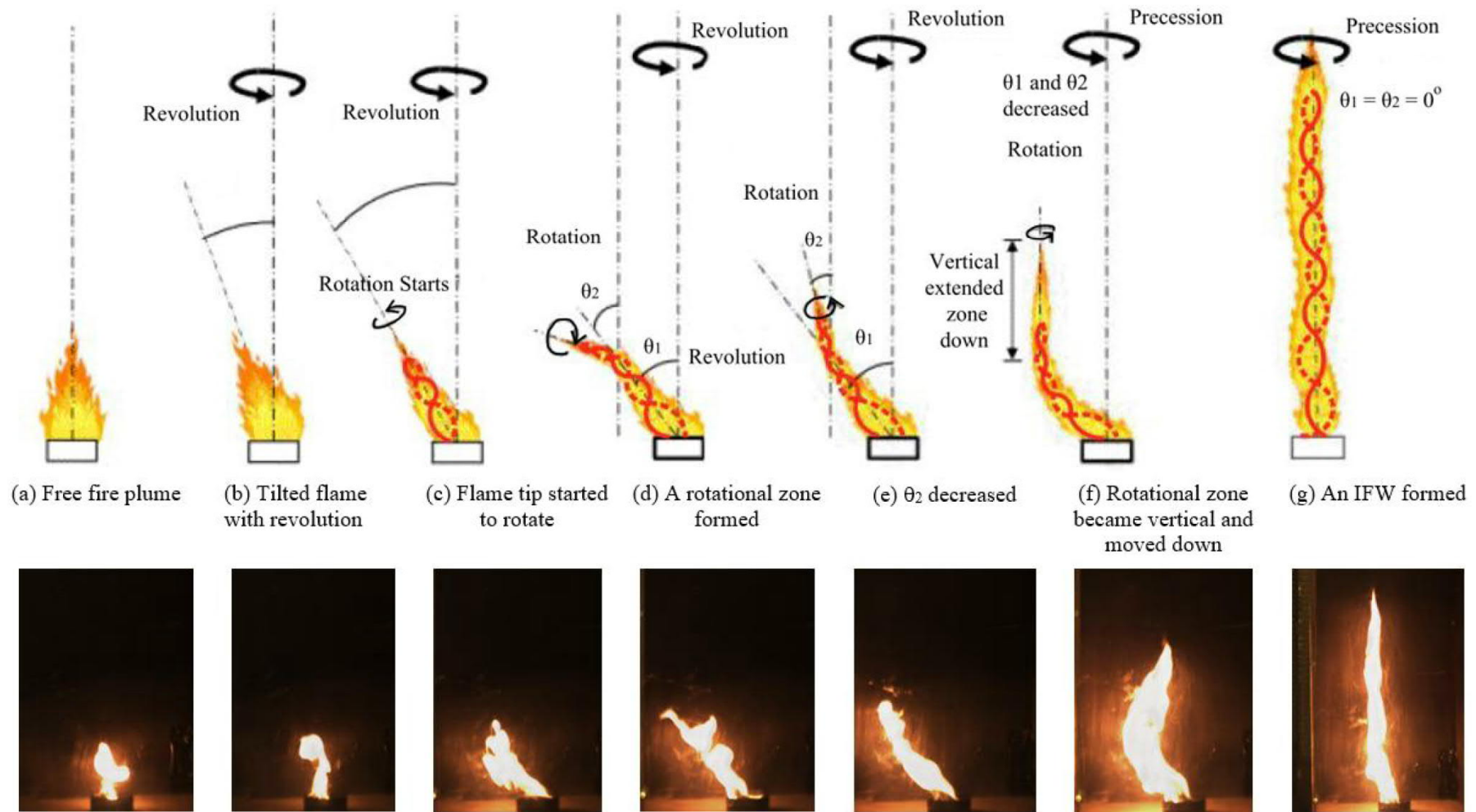
Fig 4.7 Stages to form an IFW from a high-speed camera

4.4 Empirical Expression Derived from Experimental Observation

The flame of an IFW as formed in Fig. 4.7(g) can be taken as a fast rotating cylindrical diffusion flame. Based on this observed pattern, an axis of symmetry is formed along the vertical centerline with air entrained horizontally from all directions. An IFW is a complex three-dimensional flow field and the surface of the flame has a helical structure. Within an average time, the flow field of the fire whirl can be taken as axis-symmetric.

Comparing with a normal pool fire, the flame surface of an IFW is relatively stable without having large-scale eddies and low buoyancy. Centrifugal force and density gradient along the radial direction would give a stable condition as discussed in Chapter 3. High-speed camera used can observe a better swirling flow generation patterns of the fire whirl. The flame surface of the IFW is smooth without so many wrinkles due to turbulent stratification effect. Mixing and burning of fuel and air would reduce the flame diameter of fire whirl $R(z)$ axially, then further reduce it to almost the central axis at the top part of the fire. However, the change in flame diameter is small in a fire whirl with a tall axial height. Hence, the flame diameter $R(z)$ is assumed to be a constant *R*.

Series of equation have been discussed in Chapter 3.3 on the plume mass flow rate and flame height and the burning rate in equation (3.8) to (3.15). The study approach is a good starting point aims at describing the correlations between the upward plume motion, air entrainment, combustion product flow and air intake from the shaft gap.

Although air entering through the gap might not enter into the flame directly, circular motion will be induced to affect indoor air flow pattern. Part of the air flow rate coming from this single gap would sustain combustion. A starting point of analysis is to introduce a specific proportion for this ratio. Mass burning rate of the fuel and air flow rate entrained from the gap might not be linearly correlated. Therefore, a log-log fitting is then used for further analysis.

The mass loss rate of the fuel $\dot{m}$ is assessed to relate to a power of dimensionless flame height and critical gap width $f_h^* d_g^*$ with some exponent. The power law can be justified by plotting log-log fitting.

Base on equation (3.15) in chapter 3.3, If distribution of the velocity $V_d(z)$ is known, then the relation between burning rate $\dot{m}$, width of corner gap d_g and flame height f_h can be estimated. Several assumptions have been made and justified in Chapter 3 while studying variation of air velocity through the gap along the radial direction V_d with height z with the maximum flame height is also discussed in the chapter. The following expression was suggested in terms of a constant K after derivation:

$$\dot{m}_{In} = K f_h^{*} d_g^{*} \tag{4.1}$$

Let us recall the dimensionless flame height f_h^{*} in terms of D, and d_g^* in terms of vertical shaft width a (in m) with the gap are given by equation (3.19a) & (3.19b) in chapter 3.4. Therefore, plotting $\ell n \dot{m}_{In}$ against $\ell n f^* d_g^{*}$ should give a straight line.

4.5 Three Mass Loss Rate Averages

The change of fuel mass with time was measured by placing the pool on an electronic balance with accuracy of 0.001g. The average burning rate was estimated by three values $\dot{m}_{av1}$ and $\dot{m}_{av2}$ based on the burning duration t_B and fire swirling time shown in Table 4.1 and Fig. 4.8(a):

$$\dot{m}_{av1} = \frac{\text{Mass of fuel lost}}{t_B} \tag{4.2}$$

$$\dot{m}_{av2} = \frac{\text{Mass of fuel lost}}{\text{Swirling time}} \tag{4.3}$$

From the table, $m_{av1}= 19.6g/t_B$ and $m_{av2}= 19.6g/t_{fw.}$

Another value m_{av3} was also estimated based on the average of the transient mass loss rates over the swirling time with a fire whirl.

The following linear expressions are fitted in this study with correlation coefficient being 0.886 and 0.705 respectively (Fig. 4.8(b)).

$$\ell n \dot{m}_{av1} = -0.152 \ell n f_h{}^* d_g{}^* - 2.064 \tag{4.4}$$

$$\ell n \dot{m}_{av2} = -0.150 \ell n f_h{}^* d_g{}^* - 1.959 \tag{4.5}$$

Further, $\dot{m}_{av3}$ based on the transient mass loss of propanol is also fitted using the following expression, the correlation coefficient being 0.44596.

$$\ell n \dot{m}_{av3} = -0.372 \ell n f_h{}^* d_g{}^* - 2.127 \tag{4.6}$$

The above correlations suggested that equation (4.1) holds in estimating $\dot{m}$ by equation (3.15) in chapter 3.

Mass loss rate fluctuated at transient stages. It is difficult to compare the flame heights and mass loss rates at any quasi-steady state for different test scenarios. Average values of flame heights and three estimates on average mass loss rates as in above under typical conditions including total burning duration and total whirling time.
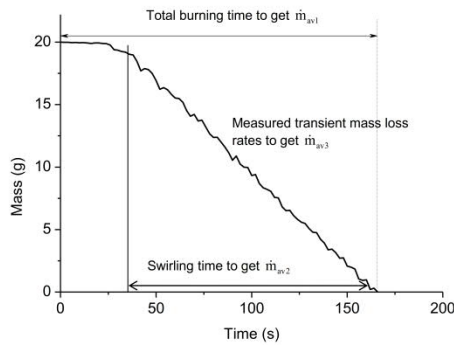
(a) Example for mass loss rates
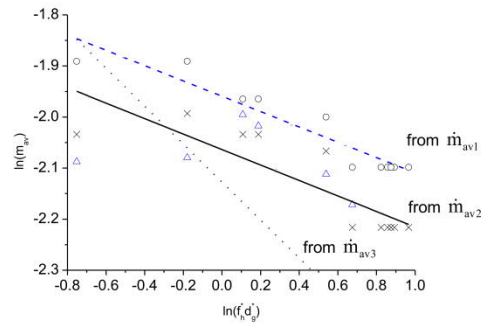
(b) $\ln(m_{av})$ Vs $\ln(f^* d^*)$
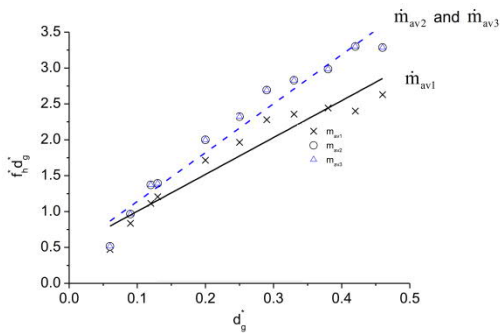
(c) Mean flame heights

Fig. 4.8 Fitted curves

Further, correlation of flame height of IFW with the gap width can be deduced by plotting $f_h^* d_g^*$ against d_g^*. As shown in Fig. 4.8(c), a line is fitted for using data $\dot{m}_{av1}$ with high value of correlation coefficient of 0.9544.

$$f_h^* d_g^* = 6.82 d_g^* + 0.458 \tag{4.7}$$

For using data $\dot{m}_{av2}$ and $\dot{m}_{av3}$ together because they are based on the same flame swirling stage, another line with correlation coefficient 0.9141 can be fitted.

$$f_h{}^* d_g{}^* = 5.14 d_g{}^* + 0.489 \qquad (4.8)$$

Therefore, air flow rate across the gap $\dot{m}_{In}$ is related to $d_g{}^*$.

One of the goals of this long-term research is to study the correlation of the flame height of an IFW with the corner gap width. A more general correlation can be derived by introducing critical gap width (ratio) and dimensionless flame height which involved the effect of the fuel pool diameter.

$\dot{m}_{In}$ is related to $d_g{}^*$.

Chapter 5.

Internal Fire Whirl in a Vertical Shaft with Partially Opened Roof

In chapter 3 and 4, the correlation between the flame height and the corner gap width is being discussed with support of analytical equations and some in depth look by using high speed camera. In this chapter, the effect on the setting of the vertical shaft to the IFW will be further investigated by means of varying the setting of the roof of the vertical shaft.

5.1 Experimental setup

A vertical shaft model of 34cm width, 35cm length and 145cm height is used in the experiment. The vertical shaft has a 3.6cm corner gap as shown in Fig. 5.1. There are marks labeled in the vertical shaft model to indicate the flame height with a 5 cm interval. In the experiment, temperature and transient mass and image are recorded.

There are different types of visualizing technology based on the refraction of light travelling in different media. Shadowgraph method, Schlieren Photography and optical holography is some of the examples. Background-oriented Schlieren (BOS) [59] is a Schlieren Photography technique applied for studying fluid flow fields. As shown in Fig. 5.2, the light is travelled through a fluid with motion from a background light source to a digital camera, the light would then be refracted and then deviated from the original path to the sensor denoted by the dotted line with deviation $\triangle h$. The $\triangle h$ can be found when the image with and without passing through fluid at the photosensitive sensor is compared with the aid of Particle Image Velocimetry (PIV) image processing technique. By using integral effects of the optical light path, the flow field can be measured by means of BOS technique.

As reviewed in the literature [60-62], the fluid density ρ is related to the refractive index n through a Gladstone-Dale constant (in m3/kg) $G(\lambda)$:

$$\frac{n-1}{\rho} = G(\lambda)$$ (5.1)

$G(\lambda)$ for air studied in this paper is expressed by:

$$G(\lambda) = 2.2244 \times 10^{-4}\left[1 + \left(\frac{6.7132 \times 10^{-8}}{\lambda}\right)^2\right]$$ (5.2)

The typical value of $G(\lambda)$ is lying between 0.1×10^{-3} and 1.5×10^{-3}. The deviation distance Δh (in m) can be expressed in terms of the focal length of the lens f (in m) and the wavelength of light λ (in m) through optical path lengths lb, lc and h (all in m):

$$\Delta h = \frac{1}{n}\left(\frac{l_b f}{l_b + l_c - f}\right)\int_{l_b - \Delta l_b}^{l_b + \Delta l_b} \frac{\partial n}{\partial r}dl$$ (5.3)

Fig 5.3 shows a typical illustration of a room fire in which hot gas will move out from the upper part of the opening and ambient cooler air will come in from the lower part of the opening. Since for different temperature of gas and air, their refractive indices are different due to their temperature difference. BOS technique can then be used to find out the boundary location of hot gases and cool air, which is the neutral plane postion of the opening in a compartment fire [60-61]. Thus, by using BOS technique the flow pattern of the air exchange across the corner gap of the shaft model could be determined. In order to define the neutral plane height, we can take use of the location of zero air flow at gap which is in general slightly different from the smoke layer interface height within the room model as shown in Fig 5.3. Location of the neutral plane height across the corner gap determined was then be compared with the air temperature variation measured by thermocouples.

Inside the shaft, the fuel is placed at the center middle of the model. It is a 7cm diameter fuel pool with 20ml of n-propanol to provide sufficient burning time. The reason for n-propanol is used because it will not produce black smoke which will affect the image taken as well as the amount of heat generated throughout the process is appropriate. The transient mass of the fuel is being recorded every second by an electronic scale. 2 scenarios are being studied with different roof opening arrangement as shown in Fig 5.1. The name for the setting are labeled as Scenario FHC for front half of the roof covered and Scenario RHC for rear half of the roof covered respectively while a normal free burning test is denoted as FS.

5.2 Formation of IFW

As shown in Fig 5.4, photos were taken to show the formation of the IFW at different stages for the 2 experiment FHC and RHC. There are 8 photos taken for each test showing the formation of the IFW from start to end. The burning times of the fuel for FHC and RHC are 221s and 220s respectively. When the fuel is burn in the free space which serves as a control, the flame height is steady with 18cm recorded and burning time of 369s

For both FHC and RHC, there is no swirling flame initially, the flame gradually started to swirl at 26s and 23s for FHC and RFC respectively. Whether the roof is opened in front or rear does not affect the formation of the IFW in the shaft as IFW is formed in both FHC and RHC. The flame height varies during the burning process with an average 40cm flame height and maximum 60cm flame height recorded.
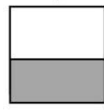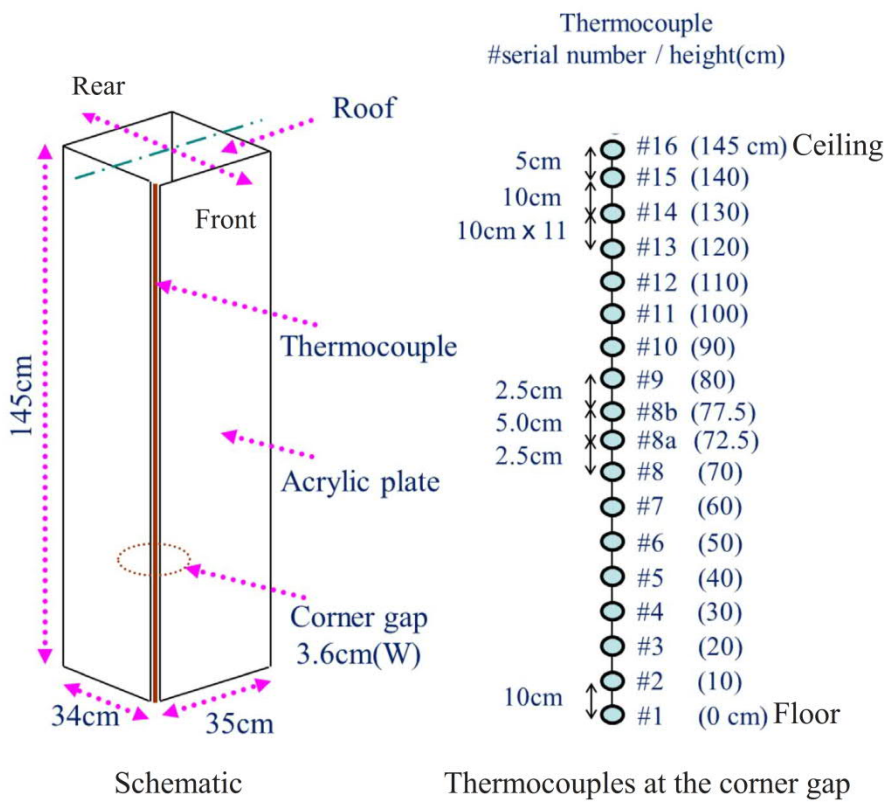
Front-half covered : FHC
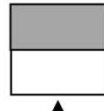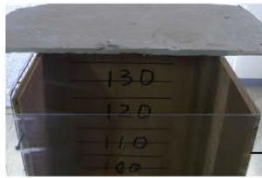
Rear-half covered: RHC

Photograph

(a) Scenarios

Thermocouple
#serial number / height(cm)

5cm	#16 (145 cm) Ceiling
10cm	#15 (140)
10cm x 11	#14 (130)
	#13 (120)
	#12 (110)
	#11 (100)
	#10 (90)
2.5cm	#9 (80)
5.0cm	#8b (77.5)
2.5cm	#8a (72.5)
	#8 (70)
	#7 (60)
	#6 (50)
	#5 (40)
	#4 (30)
	#3 (20)
10cm	#2 (10)
	#1 (0 cm) Floor

Schematic

Thermocouples at the corner gap

(b) Shaft model

Fig 5.1 Experimental Scenario in the shaft model
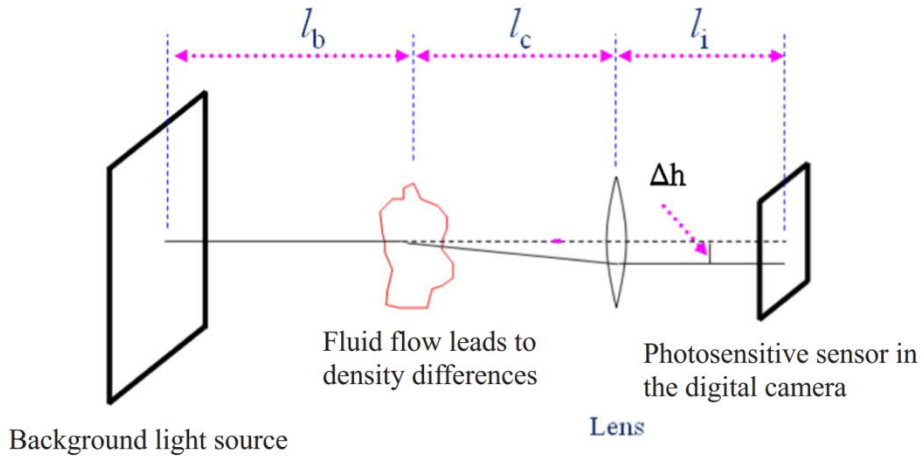
Fig. 5.2 Optical path
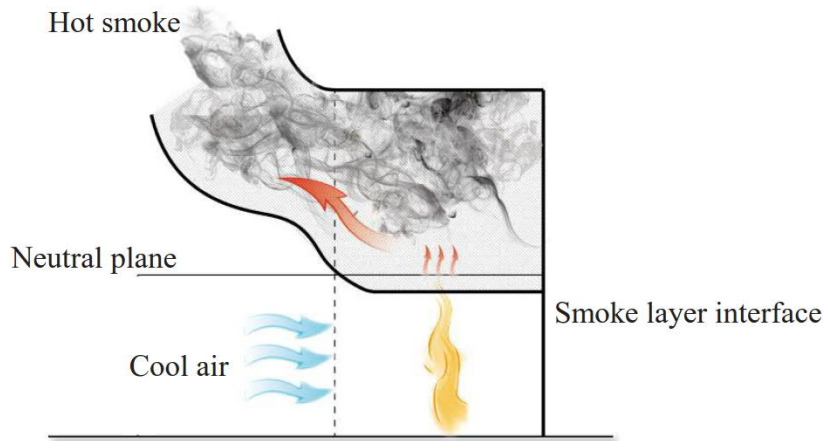
Fig. 5.3 Neutral plane and smoke layer interface height

Air is entrained through the corner gap during the burning process. If the roof is completely closed, the hot air will need to be escaped through the same gap. Thus, a hot smoke layer will be formed as shown in Fig. 5.3.

Fig. 5.5 shows the mass loss curve of the fuel in the 3 scenario FS, FHC and RHC respectively. As shown in the chart, the mass loss curve for FHC and RHC is relatively similar. However their curves drop much faster than that of FS due to stack effect for enclosing part of the roof. Furthermore, the mass loss rate of FHC and RHC increased when the IFW is formed and it leads to a shorter burning time. In

65

comparison, the burning time of FS is 369s which is 1.89 times to that of FHC and RHC. Also, it can be seen that the mass loss rate is much faster for FHC and RHC once the IFW is formed, which is 0.084g/s compared to 0.044g/s of FS.
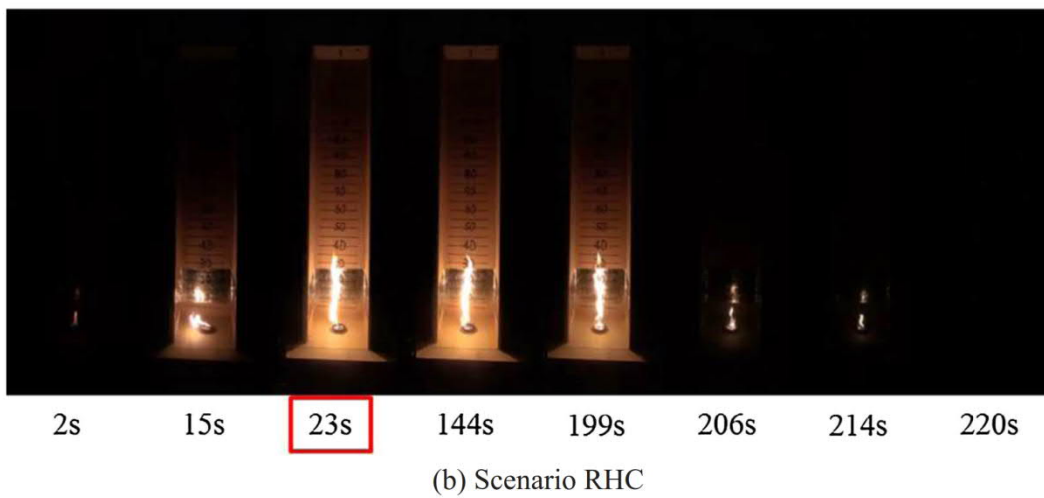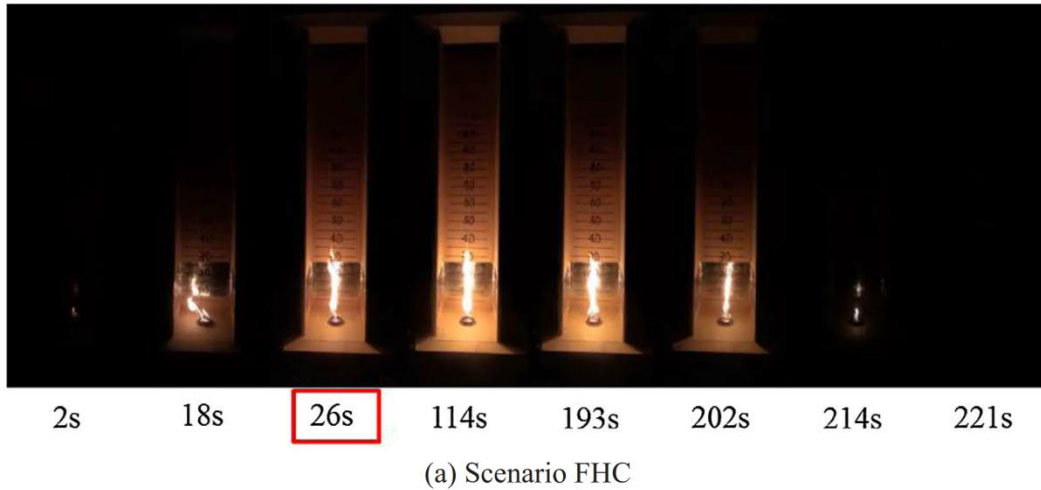

(a) Scenario FHC

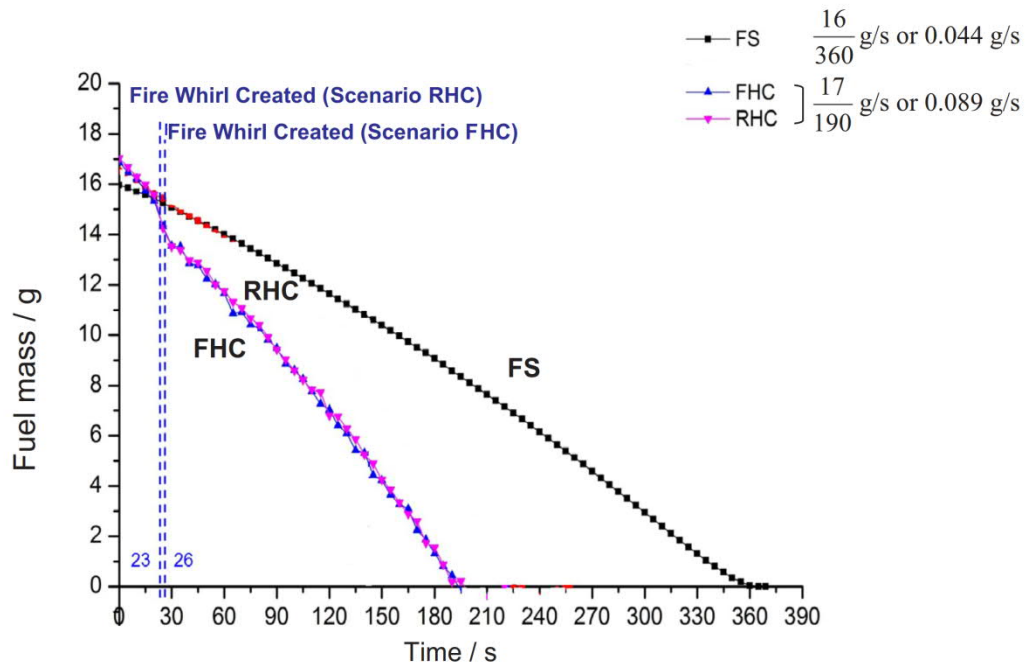(b) Scenario RHC

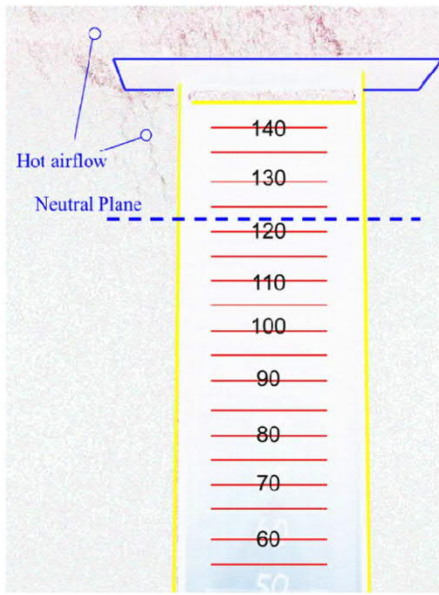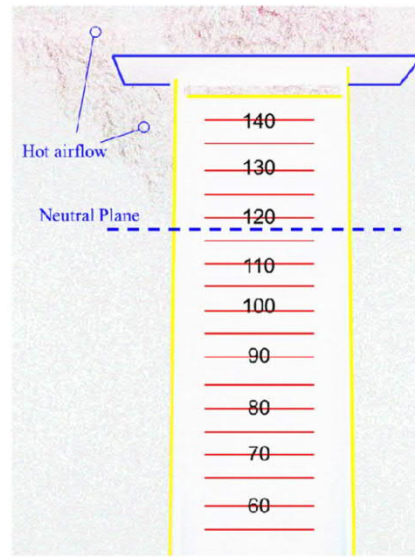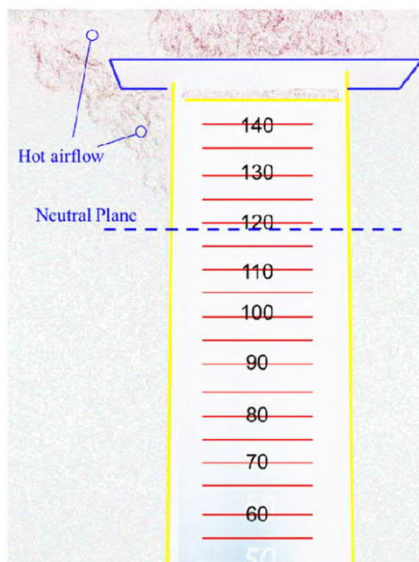**Fig 5.4 Photos taken for the experiments at different time interval**

Fig. 5.5 Fuel mass loss rate against time

(a) At 10s
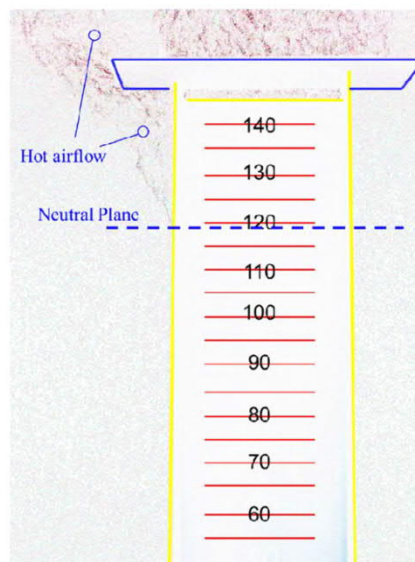
(b) At 26s

(c) At 46s

(d) At 86s

Fig 5.6 image of BOS on scenario FHC

(a) At 10s   (b) At 23s
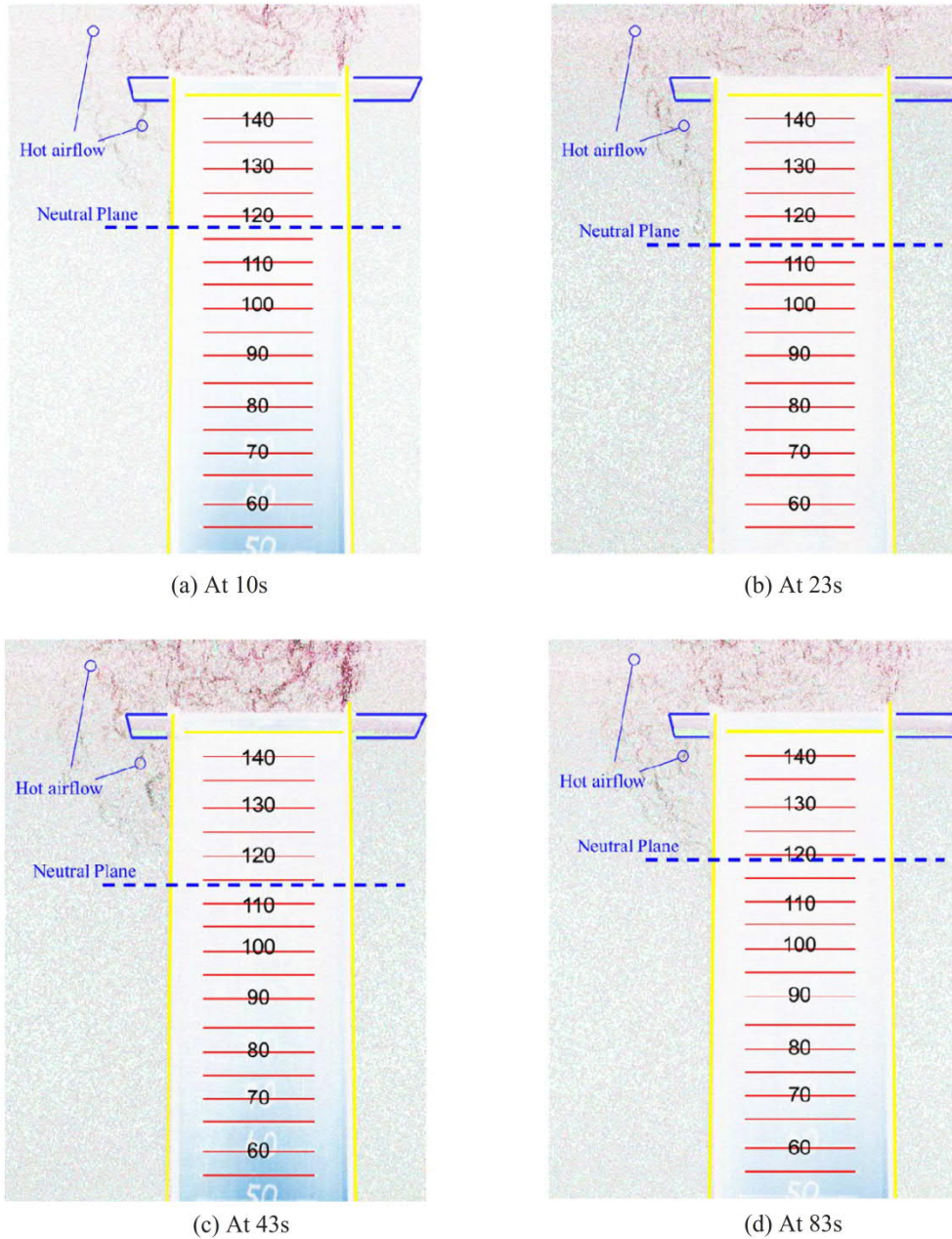
(c) At 43s   (d) At 83s

Fig 5.7 image of BOS on scenario RHC

5.3 Neutral Plane Heights and Air Temperature Measured

By using the BOS technique, the outflow of the hot air from the corner gap at the shaft is being recorded. The image recorded are illustrated in Fig. 5.6 and 5.7 for scenario FHC and RHC respectively. It can be seen that both the neutral plane height for FHC and RHC is similar with the plane height located at 122cm after 10s of burning and then dropped to 118cm when the IFW is formed at 26s. After that, it

remained at the height until 86s. As compared to study carried out before[53] which is a closed roof shaft, the neutral plane height is lower and the burning time is longer for a closed roof shaft model.

As for the air temperature changes at the corner gap width, air temperature are recorded at the time instant 10s after burning began; at the point when the IFW is formed; 20s after IFW is formed and 40s after IFW is formed. Detail can be seen in Fig 5.8. Regarding scenario RHC, the max air temperature of the hot smoke layer rises from 34°C to 36°C from 10s to 26s. The temperature of the hot smoke layer reaches the maximum of 55°C at 83s at 122.5cm; As for scenario FHC, the max air temperature of the hot smoke layer rises from 34°C to 49°C from 10s to 26s. The temperature of the hot smoke layer reaches the maximum of 66°C at 46s at 122.5cm. Hence, it can be seen that the max smoke layer temperature for RHC is slightly lower than that of FHC. The reason behind this is due to the hot smoke for RHC setting can escape at the corner gap at the front part of the vertical shaft. As compared to the earlier reported case [60], for the fully closed roof shaft model the maximum hot smoke layer temperature can reach 121°C, giving a much higher temperature as compared.
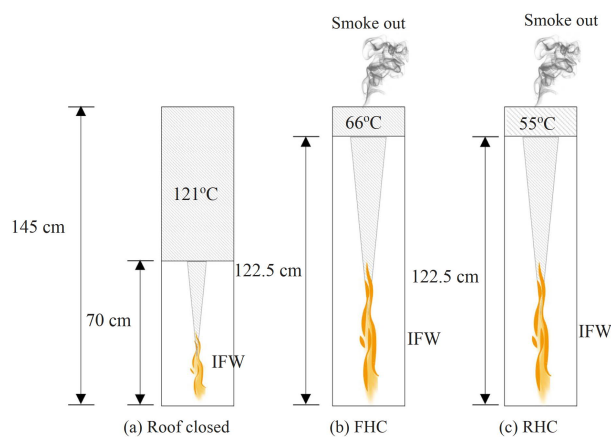

Fig. 5.8 Summary of the result

Chapter 6.

Mathematical Analysis on Attenuation of Swirling Motion of a Fire Whirl in a Vertical Shaft

As discussed in previous chapters, a fire whirl can be generated under appropriate conditions even inside a building, such as a vertical shaft. Scale models of circulating buoyant plumes were studied by different groups [15,52,63-65]. Updates include the behavior of a fire whirl generated using a burner and examined using Particle Image Velocimetry by Hartl and Smits [36]. Flame precession (or wandering) in fire whirl was further studied by Satoh, Liu and their associates [66] with precession frequency measured and analyzed using simplified models. Simple analysis and simulation were used [12] to verify the validity of applying classical theory in fire whirl scaling. The flame height was found to be proportional to heat release rate and circulation, unrelated to viscosity and turbulent conditions [12]. Flame height of fire whirl was assumed [47] to be dependent on the fuel burning rate which was in turn dependent on burning temperature, vortex core diameter and flame shape. Differences between rotational flow and irrotational flow were presented. The thermal radiation of rotational flame was stronger. A possible mechanism on why fire whirling resulted in higher flame height was proposed. One reason was due to heat feedback to the fuel surface, thus enhancing fuel vaporization. Another reason was due to the interaction of swirling flow and flame. The increase in heat radiation caused by flame circulation made more air pulled into the flame for combustion. Fire whirl height can be determined [48] by vortex core diameter because the average heat transfer rate to combustion surface was inversely proportional to vortex core diameter. A smaller

vortex core diameter (higher swirling velocity) would provide more heat to the fuel surface and enhance vaporization.

For fire whirls with weak swirling, the flame height depends on [16] fuel combustion characteristics such as fuel pool diameter, fuel type and burning rate, but not on hydrodynamic parameters such as circulation Γ. Flame height was found to be dependent on fuel vaporization in another study [51], which is consistent with literature results.

The ratio of fire whirl flame height to ordinary pool fire height was found to be determined by fuel surface mass vaporization rate [50]. The circulation Γ would enhance vaporization because the fuel surface would have stronger heat transfer ability in the presence of whirl.

Scale modeling experiments on fire whirl created by liquid pool fires in a vertical shaft with a single sidewall gap were reported in previous study [18]. It was observed that a fire whirl could be generated when the gap width lies within a suitable range of values. The experiment was extended to bigger scales by a pool fire burning in a vertical shaft of height 15 m in another study [9]. Correlation between the flame height and swirling velocity in the latter study was reported in ref. [67]. In order to make comparison of the studies [9,18,67], the main experimental conditions and flame heights compiled in Table 6.1. The critical lateral wind velocity that would generate the most intense fire whirl was determined in these studies. The effect of flow circulation on the increase in flame height was discussed in a number of studies [16, 68-70].

Attenuation of swirling velocity of the fire whirl along the vertical fire axis was studied by including variation in axial velocity and viscous dissipation using the basic equations of vorticity. A similar approach on assessing the same velocity field as in a Burgers vortex was also reported on fire whirl of different scenario and scale [71]. Momentum implications for buoyant diffusion flames and the formulated rule of vertical movement speed above fire pool surface by McCaffrey [72] were also employed in the study.

Table 6.1: Conditions of three experimental studies and flame height

Conditions	Vertical shaft scale (cm)	$\dfrac{\text{gap width}}{\text{channel width}} = \text{dimensionless gap}$	Fuel type	Maximum flame height (cm)	Average flame height (cm)	Oil pool diameter (cm)
Reference 15	35×34×145	$\dfrac{1.8 \sim 3.0}{35} = 0.05 \sim 0.1$	Propanol	75-85	35-65	7.0
Reference 16	200×200×1500	$\dfrac{14,28,56}{200} = 0.07,0.14,0.28$	gasoline	240,380,450	170,210,220	26,36,46
Reference 17	200×200×1500	28×15/200=0.14×0.075 (dimensionless width* dimensionless height)	gasoline	400	300	46
This article	210×210×900	$\dfrac{33 \sim 42}{210} = 0.16 \sim 0.20$	gasoline	300,360,450	185,225,320	20,26,46

6.1 Experimental details

Experiments on fire whirl were carried out in open roof vertical shafts of 2.1 m square and height up to 9 m (Fig. 6.1(a). A typical example showing increased flame height of fire whirl compared with non-whirling fire is given Fig. 6.1(b). A gap was opened in a side wall for supplying air. The wall gap was of width 0.33-0.44 m. M and C are thermocouple trees. Two glass panes of size 2.1 m by 1.5 m were installed on one side for observing the flame characteristics. Three experiments labelled SW-S, SW-M, SW-L for pool fire diameters of 0.2 m, 0.26 m and 0.46 m respectively were performed. The fuel depth in the pool was kept at 4 cm to have gasoline volumes of 1.25 litres, 2.12 litres and 6.65 litres respectively.
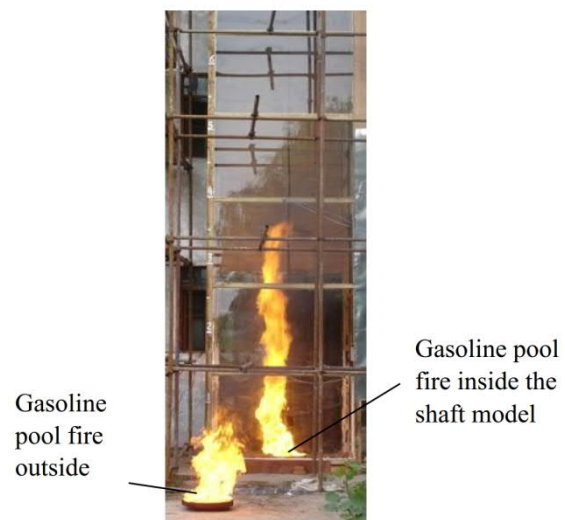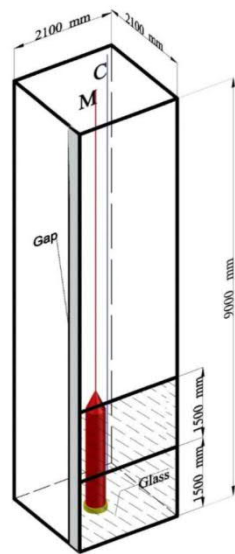
(a) Geometry of test shaft   (b) Fire height with and without whirl

Fig. 6.1: Geometry of shaft.

Fig. 6.2(a) is a fire whirl scenario and Fig. 6.2(b) shows the longitudinal thermocouple tree located at the central axis with 22 temperature measuring points. The temperatures were acquired with armoured thermocouple K type, and captured by DAQ data acquisition system and computer. The measured temperatures at different times are shown in Fig. 6.2(c).

(a) Fire whirl moment

(b) Positions of 22 thermocouple temperature measurement points along the central axis
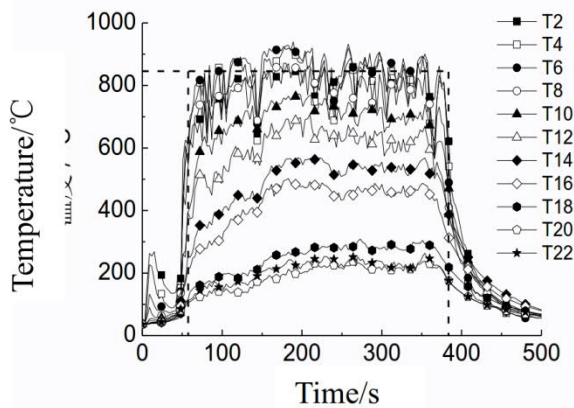
(c) Temperature profile

Fig. 6.2: Typical experimental temperature measurement and profile (0.2 m diameter oil pan with 93# gasoline)

From Fig. 6.3 on variation of temperature with height, correlation between flame height, swirling diameter and heat release rate can be deduced. The flame heights were 1.85 m and 2.25 m for pool diameters of 0.2 m and 0.26 m respectively. For pool diameter of 0.46 m, the flame height was over 3.20 m. The flame height of a fire whirl

depends on the pool diameter (or heat release rate) and the strength of flame rotation or vorticity Γ.

As observed from the transient flame heights of the fire whirl in this study, circular motions at the bottom and top parts were different. For example, air swirled at the bottom, but only moved upward at the upper part. Five zones H1 to H5 can be identified in a typical fire whirl as shown in Fig. 6.4. The flame movement trajectories at each zone are very different as shown in the figure. The tilted angle to the horizontal of the swirling motion increased from 0° in the lowest zone H1 to 90° in the uppermost zone H5.

Flame height as in Figs. 6.1 and 6.2 can be determined from the red flame edge of the video using transient flame spectrum of about 3.32 µm wavelength, or about 600℃ with naked eye observation. Photographs taken at intervals of 1 s were extracted.

Gas movement in zone H5 was vertically upward and in zone H1 it was basically horizontal, as shown in Fig. 6.4(a). Solenoidal movement was observed in zones H2, H3 and H4, as shown in Fig. 6.4(b) and Fig. 6.4(c). All these geometric features of flaming regions are the resultant effects of baroclinic force and buoyancy on swirling motion. A mathematical model is developed in this paper from such experimental observations. Fig. 6.4 shows the instantaneous video view and photos. In the photo, a part of the carbon black particle trajectory that does not burn completely is visible, and can be seen from different angles of rotation.
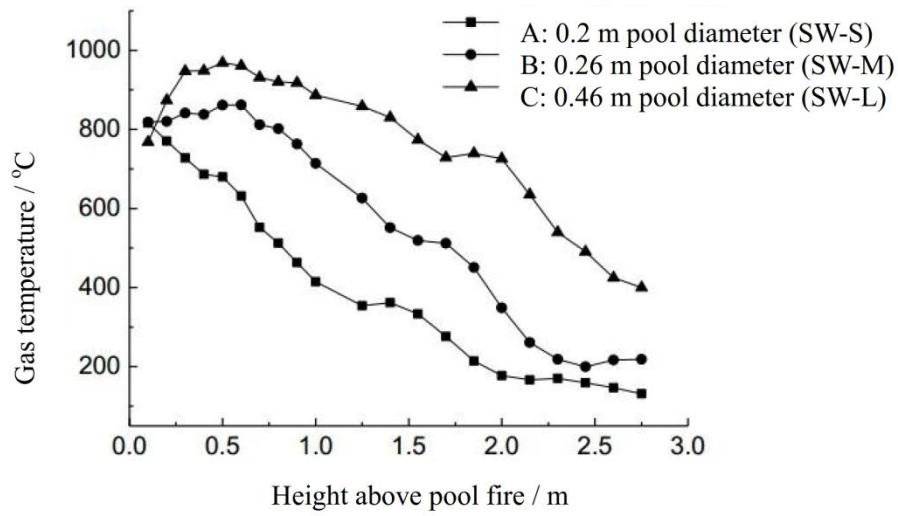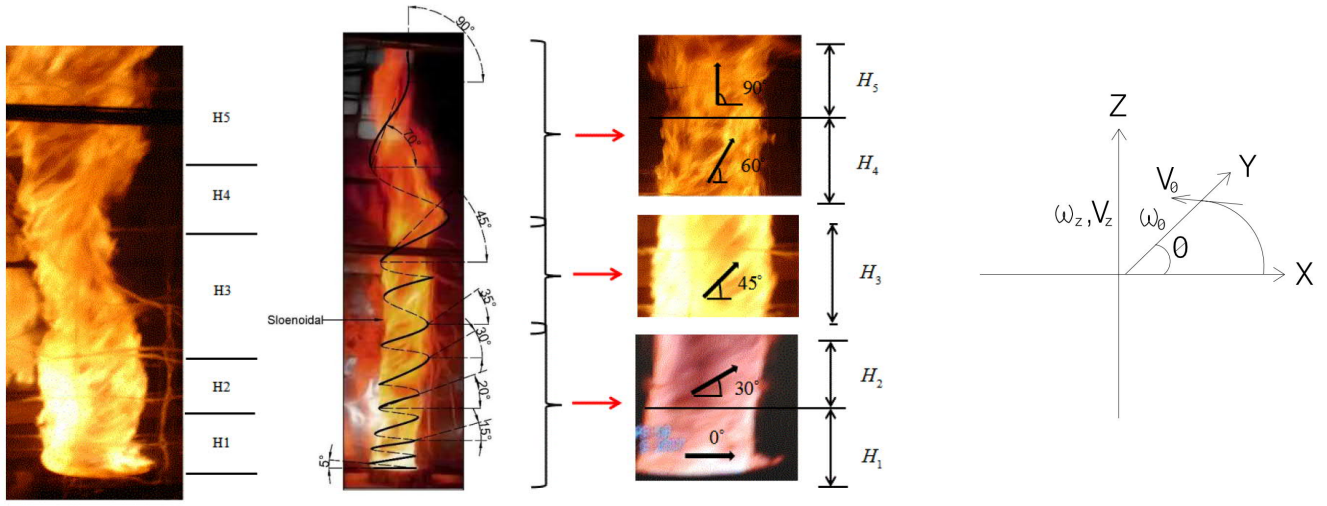
(a) Vertical gas temperatures at pool fire central axis
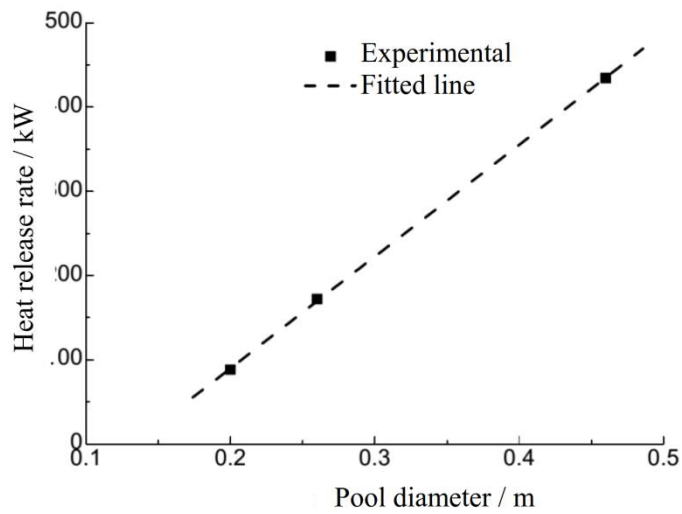
(b) Heat release rate

Fig. 6.3: Experimental results on the three different pool diameters

(a)Experimental observation   (b)Solenoidal movement   (c) Five zones   (d) Velocity and angular component

Fig. 6.4: Flame trajectories in five zones of a typical fire whirl and schematic diagram of solenoidal movement and the velocity and angular velocity component illustration

A summary of forces driving the gas motion in the five zones is shown in Table 6.2. $V_z, V_\theta, \omega_z, \omega_\theta$ are the velocity components and angular velocity along z and θ -direction respectively as shown in Fig.6.4(d).

Baroclinic force dominates in the lowest zone H1, but buoyancy is the key factor in the uppermost zone H5. Flame features in the zones in between are results of the relative magnitudes of baroclinic force and buoyancy.

In view of Table 6.2, baroclinic force is important in zone H1. The temperature difference between inside and outside the flame will be the driving force. When $\nabla\left(\frac{1}{\rho}\right)$ is perpendicular to ∇p, baroclinic force is the maximum. When z increases, zone H2 has $\nabla\left(\frac{1}{\rho}\right)$ and ∇p inclined at an angle of about 60°, baroclinic force is reduced here but buoyancy increases. For zone H3, $\nabla\left(\frac{1}{\rho}\right)$ and ∇p are inclined at 45°, and baroclinic force is very close to buoyancy.

When z increases further (zone H4), the angle between $\nabla\left(\frac{1}{\rho}\right)$ and ∇p is about 30°, and baroclinic force is smaller than buoyancy. When $\nabla\left(\frac{1}{\rho}\right)$ is parallel to ∇p, baroclinic force is zero and the plume is driven solely by buoyancy. In practice, only changes in V_z is considered. For $\nabla\left(\frac{1}{\rho}\right)$ and ∇p inclined at angles from 5° to 85°, it is adequate to study the three zones H2, H3and H4 only. The main driving force for circular motion occurs at the burning surface when the angle between $\nabla\left(\frac{1}{\rho}\right)$ and ∇p is larger than 45°.

Swirling flames result from inclination of contour surfaces of density and pressure. Vortex motion is generated from convection along the tangential direction with thermal differences. Baroclinic force would change the directions of fluid motion, and hence generate circular motions. Buoyancy due to density difference would drive fluid to move along the upward directions. Therefore, the relation between the tangential velocity and the vertical velocity of the rotating fluid reflects the relative magnitudes of buoyancy and baroclinic force. For baroclinic force greater than buoyancy, $V_\theta > V_z$ as in zone H2 of Table 6.2. For baroclinic force of similar magnitude to buoyancy, $V_z \approx V_\theta$ as in zone H3 of Table 6.2. For baroclinic force smaller than buoyancy, $V_z > V_\theta$ as in H4 region of Table 6.2.

The Froude number Fr is taken as the ratio of the baroclinic force to buoyancy. Upon generation of a fire whirl, Fr varies from infinity to 0 from the bottom to the top of flame.

The swirling motion of fire whirl was studied analytically using a simple mathematical model in the following sections. Classical models with analytical solutions were applied by focusing on the variations of angular velocity ω_z and tangential velocity V_θ along the radial direction *r*.

For dimensionless gap width (defined in Table 6.1) of 0.16 to 0.20, very stable swirling motion resulted, giving the tallest flame height and highest air temperature under pool diameter of 0.2 m, 0.26 m and 0.46 m. Typical flame pictures in the four stages (initial, ascent, stabilization and declining stage) for the 0.2 m-diameter pool fire are shown in Fig. 6.5. Putting these results into the semi-empirical expressions would give some insights on how circular motion changes along both *r* and *z.*

Zone	Velocity characteristics	Vertical velocity $\mathbf{V}_z$	Tangential velocity $\mathbf{V}_\theta$	$\mathbf{V}_z/\mathbf{V}_\theta$	Rotational angular velocity ω_z /ms^{-2}	Stretching force $\mathbf{F}_c = \omega_z \dfrac{\partial \mathbf{V}_z}{\partial z}$	Buoyancy force $\mathbf{F}_b = \sigma \mathbf{g}$, $\sigma = \rho - \rho_d$	$\mathbf{F}_c/\mathbf{F}_b$	Baroclinic force $\nabla\left(\dfrac{1}{\rho}\right)\times\nabla p$ $=\dfrac{1}{r}\dfrac{\partial p}{\partial \theta}\dfrac{\partial}{\partial r}\left(\dfrac{1}{\rho}\right)-\dfrac{\partial p}{\partial r}\dfrac{1}{r}\dfrac{\partial}{\partial \theta}\left(\dfrac{1}{\rho}\right)$ $p_1 > p_2 > p_3 > p_4$, $\rho_1 > \rho_2 > \rho_3 > \rho_4$	$\gamma\nabla^2\omega = \gamma\left(\nabla^2\omega_\theta + \nabla^2\omega_z\right)$ $\tau = \tau_\theta + \tau_z$	Remarks
H5		$\mathbf{V}_z = \mathbf{V}_{z\max}$	$\mathbf{V}_\theta = 0$	$\tan 90^\circ = \infty$	$\omega_z = 0$	$\omega_z = 0$, $\dfrac{\partial \mathbf{V}_z}{\partial z}=0$	$\sigma \mathbf{g}\left(\begin{array}{c}H_1 + H_2 + H_3 \\ + H_4 + H_5\end{array}\right)$	$\to 0$	$\mathbf{V}_\theta = 0$, $\dfrac{\mathbf{n}_p}{\mathbf{n}_p} = \tan 0^\circ$	$\gamma\nabla^2\omega_z = 0$, $\gamma\nabla^2\omega_\theta = \tau_{\theta\max}$	Baroclinic force $\ll$ Buoyancy force $\mathbf{F}_c \ll \mathbf{F}_b$
H4		$\dfrac{\mathbf{V}_{z\max}}{2} < \mathbf{V}_z < \mathbf{V}_{z\max}$	$0 < \mathbf{V}_\theta < \dfrac{\mathbf{V}_{\theta\max}}{2}$	$\tan 60^\circ = 1.732$	$0 < \omega_z < \dfrac{\omega_{z\max}}{2}$	$\omega_z < \dfrac{\omega_{z\max}}{2}\dfrac{\partial \mathbf{V}_z}{\partial z}$	$\sigma \mathbf{g}\left(\begin{array}{c}H_1 + H_2 \\ + H_3 + H_4\end{array}\right)$	$(0,1)$	$\dfrac{\mathbf{n}_p}{\mathbf{n}_p} = \tan 30^\circ$	$\tau_\theta > \tau_z$	Baroclinic force $<$ Buoyancy $\mathbf{F}_c < \mathbf{F}_b$
H3		$\dfrac{\mathbf{V}_{z\max}}{2}$	$\dfrac{\mathbf{V}_{\theta\max}}{2}$	$\tan 45^\circ = 1$	$\dfrac{\omega_{z\max}}{2}$	$\dfrac{\omega_{z\max}}{2}\dfrac{\partial \mathbf{V}_z}{\partial z}$	$\sigma \mathbf{g}(H_1 + H_2 + H_3)$	1	$\dfrac{\mathbf{n}_p}{\mathbf{n}_p} = \tan 45^\circ$	$\tau_\theta \approx \tau_z$	Baroclinic vorticity induced velocity $\mathbf{v}_\theta$ and buoyancy induced velocity $\mathbf{v}_z$ are comparable to the solenoidal component of the velocity
H2		$0 < \mathbf{V}_z < \dfrac{\mathbf{V}_{z\max}}{2}$	$\dfrac{\mathbf{V}_{\theta\max}}{2} < \mathbf{V}_\theta < \mathbf{V}_{\theta\max}$	$\tan 30^\circ = 0.577$	$\dfrac{\omega_{z\max}}{2} < \omega_z < \omega_{z\max}$	$\omega_z < \omega_{z\max}\dfrac{\partial \mathbf{V}_z}{\partial z}$	$\sigma \mathbf{g}(H_1 + H_2)$	$(1,+\infty)$	$\dfrac{\mathbf{n}_p}{\mathbf{n}_p} = \tan 60^\circ$	$\tau_\theta < \tau_z$	$\mathbf{F}_c > \mathbf{F}_b$
H1		$\mathbf{V}_z = 0$	$\mathbf{V}_\theta = \mathbf{V}_{\theta\max}$	$\tan 0^\circ = 0$	$\omega_z = \omega_{z\max}$	$\omega_{z\max}\dfrac{\partial \mathbf{V}_z}{\partial z}$	$\sigma \mathbf{g}(H_1)$ When $H_z \to 0$, $\mathbf{F}_b \to 0$	$\to +\infty$	$\dfrac{\mathbf{n}_p}{\mathbf{n}_p} = \tan 90^\circ$	$\gamma\nabla^2\omega_z = \tau_{z\max}$, $\gamma\nabla^2\omega_\theta \approx 0$	Baroclinic *force* $\gg$ *Buoyancy* $\mathbf{F}_c \gg \mathbf{F}_b$ *No buoyancy baroclinic vorticity,* ω_z *would be the largest.*

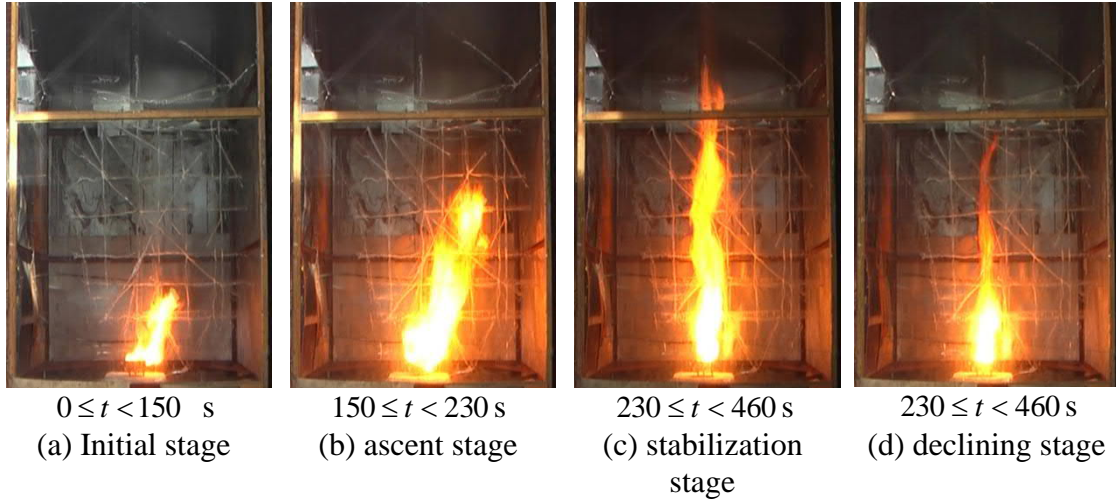| $0 \le t < 150$ s	$150 \le t < 230$ s	$230 \le t < 460$ s	$230 \le t < 460$ s
(a) Initial stage	(b) ascent stage	(c) stabilization stage	(d) declining stage

Fig. 6.5: Typical flame pictures at four stages of SW-S with 0.2 m diameter pool.

6.2 Analytical Solution for Vorticity and Angular Velocity

The vorticity transport equation can be written as:

$$\frac{\partial \boldsymbol{\omega}}{\partial t} + \mathbf{V} \cdot \nabla \boldsymbol{\omega} = \boldsymbol{\omega} \cdot \nabla \mathbf{V} + \nu \, \nabla^2 \boldsymbol{\omega} \tag{6.1}$$

Equation (6.1) was applied to zones H1 to H5 and summarized in Table 6.2, with the baroclinic term given in greater detail.

Equation (6.1) is transformed into cylindrical coordinates (r, θ, z), with z being the axis for circular motion. In this way, ω_r and ω_θ are zero, and equation (6.1) becomes:

$$\frac{\partial \omega_z}{\partial t} + V_r \frac{\partial \omega_z}{\partial r} + \frac{V_\theta}{r} \frac{\partial \omega_z}{\partial \theta} + V_z \frac{\partial \omega_z}{\partial z} = \omega_z \frac{\partial V_z}{\partial z} + \nu \left(\frac{1}{r} \frac{\partial}{\partial r} r \frac{\partial \omega_z}{\partial r} + \frac{1}{r^2} \frac{\partial^2 \omega_z}{\partial \theta^2} + \frac{\partial^2 \omega_z}{\partial z^2} \right) \tag{6.2}$$

Assuming ω_z does not vary with θ, then

$$\frac{\partial \omega_z}{\partial t} + V_r \frac{\partial \omega_z}{\partial r} + V_z \frac{\partial \omega_z}{\partial z} = \nu \left(\frac{1}{r} \frac{\partial}{\partial r} \left(r \frac{\partial \omega_z}{\partial r} \right) + \frac{\partial^2 \omega_z}{\partial z^2} \right) + \omega_z \frac{\partial V_z}{\partial z} \tag{6.3}$$
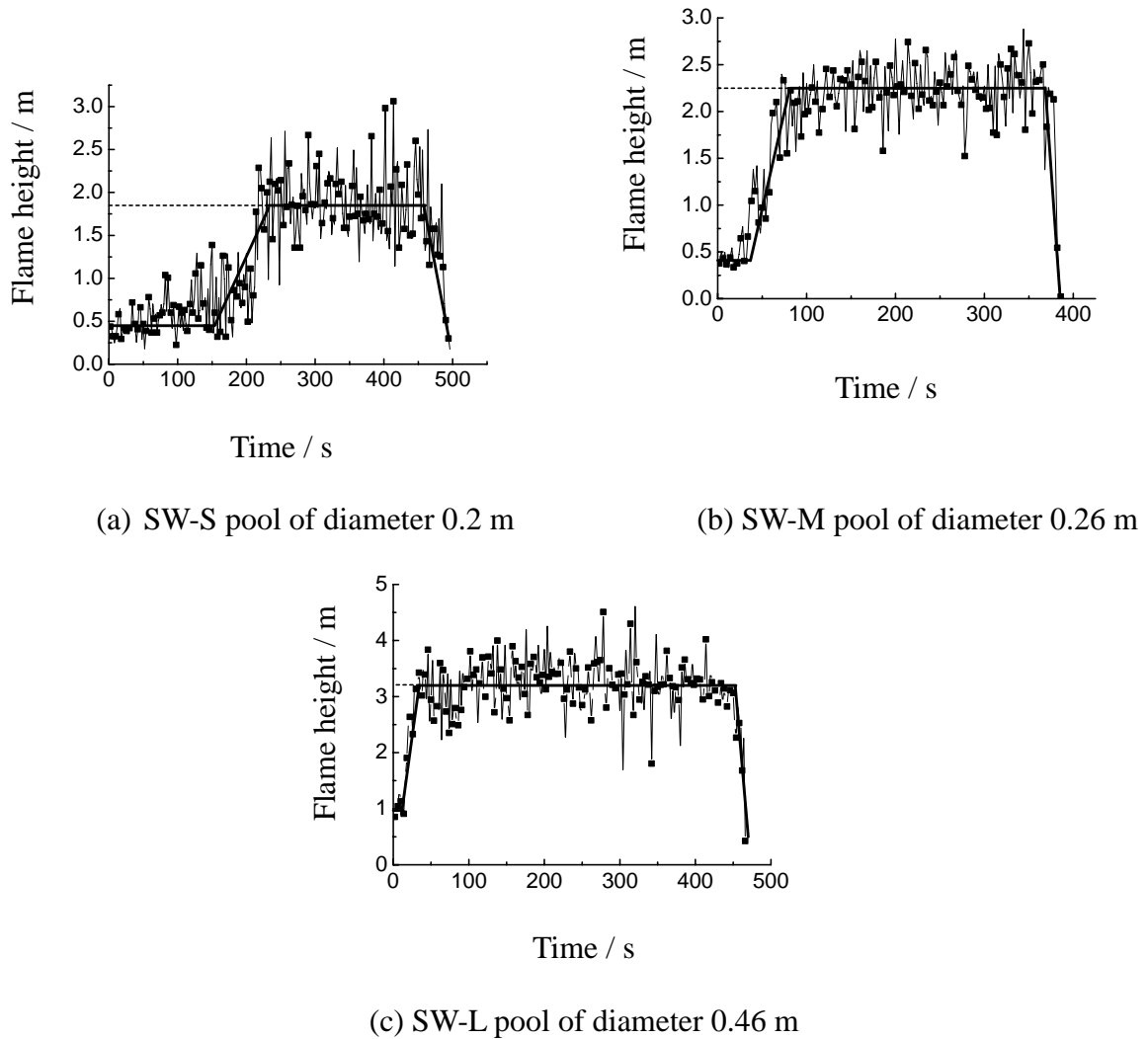
Applying the experimental results shown in Fig. 6.2 to Fig. 6.6, flame swirling at steady state can be separated into the parts $\omega_{zr}(r)$ and $\omega_{zz}(z)$ along the r- and z-directions, i.e.,

$$\omega_z(r,z) = \omega_{zr}(r)\omega_{zz}(z) \tag{6.4}$$

Assuming that $\omega_{zr}(r)$ and $\omega_{zz}(z)$ are not related, equation (6.3) becomes:

$$V_r \frac{\partial \omega_z}{\partial r} = \bar{v}_r \frac{1}{r} \frac{\partial}{\partial r}\left(r \frac{\partial \omega_z}{\partial r}\right) \tag{6.5}$$

$$V_z \frac{\partial \omega_z}{\partial z} = \bar{v}_z \frac{\partial^2 \omega_z}{\partial z^2} + \omega_z \frac{\partial V_z}{\partial z} \tag{6.6}$$

(a) SW-S pool of diameter 0.2 m

(b) SW-M pool of diameter 0.26 m

(c) SW-L pool of diameter 0.46 m

Fig. 6.6: Transient flame heights with different pool of diameter.

84

In the above equations, $\overline{V}_z$ is the dissipation of ω_z along the z-direction, and is much greater than the kinematic viscosity V. $\overline{V}_z$ depends on z and includes minimum dissipative effects due to ω_z and reduction in baroclinic force due to gravity. Combining all experimental observations related to dissipation of circular motion, $\overline{V}_z$ is related to h_0. $\overline{V}_r$ can be taken as the variation of ω_z dissipation along r. Equations (6.5) and (6.6) will be solved analytically in this paper.

Variation of ω_z along the r-direction and the effects of V_r and $\overline{V}_r$ are governed by equation (6.5), independent of θ and z.

Variation of ω_z under $\overline{V}_z$, upward motion V_z, and $\dfrac{\partial V_z}{\partial z}$ along the z-direction is governed by equation (6.6). From Table 1 and Fig. 6.3, ω_z has the highest value at the flame base (z=0). At the top of flame ($z=h_0$), ω_z is zero. Variation of ω_z is also affected by the average dissipation $\overline{V}_z$, not just V_z and $\dfrac{\partial V_z}{\partial z}$.

For a buoyant flame and a free plume, buoyancy force causes vertical acceleration of the flow inside the flame zone. The stretching term $\omega_z \dfrac{\partial V_z}{\partial z}$ causes the amplification of non –zero vorticity ω_z. For an upward accelerating flow, $\dfrac{\partial V_z}{\partial z}$ is positive, giving an increase of ω_z, provided that non-zero background vorticity is introduced. This is the explanation of the development of a rotating core in a rising buoyant flow for positive value of $\dfrac{\partial V_z}{\partial z}$.

The term $\omega_z \dfrac{\partial V_z}{\partial z}$ becomes negative in the upper plume where vertical velocity decreases with height. In this region, the vortex tubes are not stretched, but expanded due to decreasing vorticity, since vorticity could be reduced by $\overline{V}_r$ and $\overline{V}_z$ Meanwhile the baroclinic torque and dilatation are also responsible for the reduction.

The axisymmetric flow is considered for which the transport equation for ω_z takes the form (6.3) with the baroclinic and dilation terms equal to zero. V_z at different z in a buoyant flame and a plume is assumed:

$$V_z = \alpha z + b \tag{6.7}$$

Such a complicated swirling problem in fire whirl cannot be solved by a single step. In this study, the upward velocities at the flame base with and without swirling are assumed to be similar based on Fig. 6.7. This is indicated in zones H1 and H2 at the bottom of fire whirl (Fig. 6.4), where the baroclinic effect is the key part and buoyancy effect has little effect. The effect of swirling would give longer flame height due to buoyancy and very small V_z value.
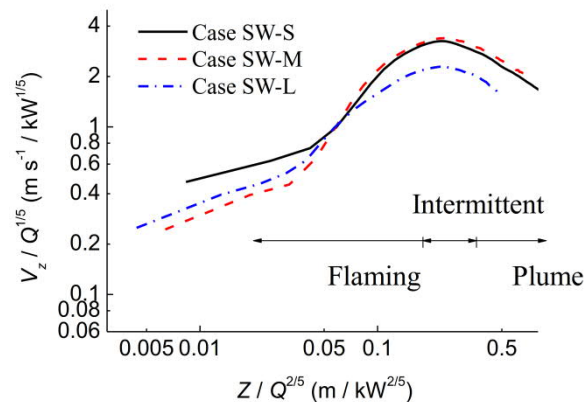

Fig. 6.7: Variation of vertical velocity with height and heat release rate of fire whirl.

As ω_{zr} is a function of r only, equation (6.5) becomes:

$$\frac{\alpha r}{2}\frac{\partial(\omega_{zr})}{\partial r}+\bar{v}_r\left(\frac{\partial^2 \omega_{zr}}{\partial r^2}+\frac{1}{r}\frac{\partial \omega_{zr}}{\partial r}\right)=0 \tag{6.8}$$

At $r=0$, ω_z reaches a maximum value, and $\omega_{zr}(r)$ can be expressed as:

$$\omega_{zr}(r)=\omega_{zr}(r=0)\exp\left(-\frac{\alpha r^2}{4\bar{v}_r}\right) \tag{6.9}$$

Solving equation (6.9), by conservation of mass and boundary condition gives limited

value V_r at $r=0$,

$$V_r=-\frac{\alpha}{2}r \tag{6.10}$$

Combining equations (6.4) and (6.7) with equation (6.6) would give a key equation on

circular motion:

$$\frac{\mathrm{d}^2\omega_{zz}}{\mathrm{d}z^2}-\left(\frac{\alpha}{v_z}z+\frac{b}{v_z}\right)\frac{\mathrm{d}\omega_{zz}}{\mathrm{d}z}+\frac{\alpha}{v_z}\omega_{zz}=0 \tag{6.11}$$

Taking the first three terms of the solution of (6.11) gives:

$$\omega_{zz}(z)\approx\omega_{z\max}(1-\frac{1}{2}\frac{\alpha}{v_z}z^2-\frac{1}{6}\frac{\alpha b}{v_z^2}z^3-\frac{1}{24}\frac{\alpha^2}{v_z^2}z^4-\frac{1}{24}\frac{\alpha b^2}{v_z^3}z^4-\frac{1}{40}\frac{\alpha^2 b}{v_z^3}z^5-\frac{1}{120}\frac{\alpha b^3}{v_z^4}z^5 \tag{6.12}$$
$$-\frac{1}{240}\frac{\alpha^3}{v_z^3}z^6-\frac{1}{120}\frac{\alpha^2 b^2}{v_z^4}z^6-\frac{1}{720}\frac{\alpha b^4}{v_z^5}z^6)=C_2\cdot\omega_{z\max}$$

Results on C_2 of equation (6.12) for small, medium and large pools are shown in

Table 6.3. Similar results obtained without keeping the higher order terms.

87

Table 6.3: Results on keeping the first three terms in equation (6.12) and magnitude of higher order terms

Test	z / m	C_1	C_2	Δ (%)
Small pool SW-S	0.3	0.973404	0.973402	0.000204
	0.8	0.81235	0.812423	-0.00897
	1.0	0.619307	0.610127	1.482215
Medium pool SW-M	0.3	0.982105	0.982105	5.19×10^{-5}
	0.8	0.87302	0.873031	-0.00136
	1.0	0.767017	0.764775	0.292329
	1.5	0.420601	0.40176	4.479495
Large pool SW-L	0.3	0.991145	0.991145	1.63×10^{-5}
	1.0	0.900666	0.900633	0.003728
	1.5	0.657352	0.641158	2.463494

Using the boundary conditions $\omega_z(r=0, z=0)$, and let $\omega_{z\max}$ be the maximum

value of ω_z, equation (6.12) gives:

$$\omega_z(r,z) \approx \omega_{z\max} \exp\left(-\frac{\alpha r^2}{4\overline{v}_r}\right)\left[1 - \frac{\alpha}{2\overline{v}_z}z^2 - \frac{b\alpha}{6\overline{v}_z^2}z^3 - \frac{\alpha^2}{24\overline{v}_z^2}z^4 - \frac{b^2\alpha}{24\overline{v}_z^3}z^4\right] = C_1 \cdot \omega_{z\max} \exp\left(-\frac{\alpha r^2}{4\overline{v}_r}\right)$$

$$(6.13)$$

The expression in equation (6.13) gives the variation of $\omega_z(r,z)$ along r- and z-directions. $\omega_z(r,z)$ will be affected by dissipation of $\overline{V}_r$ and $\overline{V}_z$. The values of α and b come from equation (6.7). Equation (6.11) has a steady–state solution $\omega_z(r,z)$, which depends on r and z. Results for C_1 are also shown in Table 6.3.

Putting in $r_{0r}^2 = 4\overline{V}_r \big/ \alpha$ and $r_{0z}^2 = 4\overline{V}_z \big/ \alpha$, equation (6.13) can be written as:

$$\omega_z(r,z) \approx \omega_{z\max} \exp\left(-\frac{r^2}{r_{0r}^2}\right)\left[1 - 2\frac{z^2}{r_{0z}^2} - \frac{2}{3}\frac{b}{\overline{V}_z}\frac{z^3}{r_{0z}^2} - \frac{2}{3}\frac{z^4}{r_{0z}^4} - \frac{2b^2}{3\overline{V}_z\alpha}\frac{z^4}{r_{0z}^4}\right] \tag{6.14}$$

In general,

$$\omega_z = \frac{1}{r}\frac{\partial}{\partial r}(rV_\theta) = \frac{1}{r}\frac{\partial}{\partial r}\left(\frac{\Gamma}{2\pi}\right) \tag{6.15}$$

Using the solution from equation (6.13), the variation of V_θ with z is also deduced.

Solving equation (6.15) gives:

$$V_\theta \approx \frac{\Gamma_0 r}{2\pi r_{0r}^2}\left(1 - \exp\left(\frac{-r^2}{r_{0r}^2}\right)\right)\left[1 - 2\frac{z^2}{r_{0z}^2} - \frac{2}{3}\frac{b}{\overline{V}_z}\frac{z^3}{r_{0z}^2} - \frac{2}{3}\frac{z^4}{r_{0z}^4} - \frac{2b^2}{3\overline{V}_z\alpha}\frac{z^4}{r_{0z}^4}\right] \qquad (r \le r_{0r}) \tag{6.16}$$

$$V_\theta \approx \frac{\Gamma_0}{2\pi r}\left(1 - \exp\left(\frac{-r^2}{r_{0r}^2}\right)\right)\left[1 - 2\frac{z^2}{r_{0z}^2} - \frac{2}{3}\frac{b}{\overline{V}_z}\frac{z^3}{r_{0z}^2} - \frac{2}{3}\frac{z^4}{r_{0z}^4} - \frac{2b^2}{3\overline{V}_z\alpha}\frac{z^4}{r_{0z}^4}\right] \qquad (r \ge r_{0r})$$

Equation (6.16) can be simplified by using the following expression for the vorticity Γ:

$$\Gamma \approx \Gamma_0\left(1 - \exp\left(-\frac{r^2}{r_{0r}^2}\right)\right)\left[1 - 2\frac{z^2}{r_{0z}^2} - \frac{2}{3}\frac{b}{\overline{V}_z}\frac{z^3}{r_{0z}^2} - \frac{2}{3}\frac{z^4}{r_{0z}^4} - \frac{2b^2}{3\overline{V}_z\alpha}\frac{z^4}{r_{0z}^4}\right] \tag{6.17}$$

However, Γ still varies with z.

Equation (6.17) gives the variation of Γ along the z-direction. It is observed that the velocity along the θ-direction decreases when z increases. On the plane of $z = 0$, $r = r_{0r}$:

$$\omega_{z\max}(z=0) = \frac{\Gamma_0}{\pi}\frac{\alpha}{4\bar{v}_r} = \left.\frac{\Gamma_0}{\pi r_{0r}^2}\right|_{z=0} \tag{6.18}$$

Similarly,

$$V_{\theta\max}(z=0) = \left.\frac{\omega_{z\max}r_{0r}^2}{2r}\right|_{r=r_{0r}} = \frac{r_{0r}}{2}\omega_{z\max} = \frac{\Gamma_0}{2\pi}\frac{1}{r_{0r}} = \frac{\Gamma_0}{2\pi}\sqrt{\frac{\alpha}{4\bar{v}_r}} = \frac{\Gamma_0}{2\pi}\frac{\sqrt{\dfrac{dV_z}{dz}}}{\sqrt{4\bar{v}_r}} \tag{6.19}$$

The two-dimensional attenuation at the viscous vortex core is similar to Oseen vortex [65,66], the total vorticity being conserved,

$$\Gamma_0 = \int_0^\infty 2\pi r \omega_z \, dr \tag{6.20}$$

When r_0 changes with time, the basic motion would be fluid moving from outside to inside, then upward along z with $v = 0$ at the symmetric axis $r = 0$.

Suppose V_θ reaches the maximum value $V_{\theta\max}$ at radius r_m, where r_m is determined by flame radius for swirling flame.

To obtain the maximum value from the second expression (for $r \geq r_{0r}$) in equation (6.16),

$$\left.\frac{dV_\theta}{dr}\right|_{r=r_m} = 0 \tag{6.21}$$

Solving gives r_m in terms of equivalent diameter r_{0r}:

$$r_m \approx 1.1207\sqrt{\frac{4\bar{v}_r}{\alpha}} \approx 1.1207 r_{0r} \tag{6.22}$$

90

Putting equation (6.22) in the second expression of equation (6.16),

$$V_{\theta\max}\left(z, r=r_m\right) \approx 0.1016\frac{\Gamma_0}{r_{0r}}\left[1-2\frac{z^2}{r_{0z}^2}-\frac{2}{3}\frac{b}{\overline{v}_z}\frac{z^3}{r_{0z}^2}-\frac{2}{3}\frac{z^4}{r_{0z}^4}-\frac{2b^2}{3\overline{v}_z\alpha}\frac{z^4}{r_{0z}^4}\right] \tag{6.23}$$

It can be observed from equation (6.23) that $V_{\theta\max}$ is dissipating along the height z.

Taking r_m as the vortex radius, for regions in the vortex, $r \ll 1.1207\sqrt{\dfrac{4\overline{v}_r}{\alpha}}$,

$$V_\theta \approx \frac{\alpha\Gamma_0 r}{8\pi\overline{v}_r}\left[1-2\frac{z^2}{r_{0z}^2}-\frac{2}{3}\frac{b}{\overline{v}_z}\frac{z^3}{r_{0z}^2}-\frac{2}{3}\frac{z^4}{r_{0z}^4}-\frac{2b^2}{3\overline{v}_z\alpha}\frac{z^4}{r_{0z}^4}\right] \tag{6.24}$$

At $z=0$, equation (24) is similar to Rankine vortex [66], where the angular speed $\dfrac{\alpha\Gamma_0}{8\pi\overline{v}_r}$ is taken as rigid body revolution. For $r \gg 1.1207\sqrt{\dfrac{4\overline{v}_r}{\alpha}}$,

$$V_\theta \approx \frac{\Gamma_0}{2\pi r}\left[1-2\frac{z^2}{r_{0z}^2}-\frac{2}{3}\frac{b}{\overline{v}_z}\frac{z^3}{r_{0z}^2}-\frac{2}{3}\frac{z^4}{r_{0z}^4}-\frac{2b^2}{3\overline{v}_z\alpha}\frac{z^4}{r_{0z}^4}\right] \tag{6.25}$$

At $z=0$, equation (6.25) is also similar to Rankine vortex (viscous vortex distribution of velocity) along the tangential direction.

It is obvious that V_θ decreases along z. Although vorticity is dispersed upward, vortex energy is supplied by motion from outside to inside, compensating the energy lost.

From equation (6.13),

$$\frac{\omega_z\left(r,z\right)}{\omega_{z\max}} \approx \exp\left(-\frac{\alpha r^2}{4\overline{v}_r}\right)\left[1-\frac{\alpha}{2\overline{v}_z}z^2-\frac{b\alpha}{6\overline{v}_z^2}z^3-\frac{\alpha^2}{24\overline{v}_z^2}z^4-\frac{b^2\alpha}{24\overline{v}_z^3}z^4\right] \tag{6.26}$$

From equations (6.16), (6.19) and (6.25) gives:

$$\frac{V_\theta}{V_{\theta\max}} \approx \frac{r}{2}\sqrt{\frac{\alpha}{\bar{v}_r}}\left(1-\exp\left(\frac{-\alpha r^2}{4\bar{v}_r}\right)\right)\left[1-\frac{\alpha}{2}\frac{z^2}{\bar{v}_z}-\frac{\alpha^{3/2}}{12}\frac{b}{\bar{v}_z^{5/2}}z^3-\frac{\alpha^2}{24}\frac{z^4}{\bar{v}_z^2}-\frac{\alpha}{24}\frac{b^2}{\bar{v}_z^3}z^4\right]$$

$$(r \le 2\sqrt{\frac{\bar{v}_r}{\alpha}})$$

$$\frac{V_\theta}{V_{\theta\max}} \approx \frac{2}{r}\sqrt{\frac{\bar{v}_r}{\alpha}}\left(1-\exp\left(\frac{-\alpha r^2}{4\bar{v}_r}\right)\right)\left[1-\frac{\alpha}{2}\frac{z^2}{\bar{v}_z}-\frac{\alpha^{3/2}}{12}\frac{b}{\bar{v}_z^{5/2}}z^3-\frac{\alpha^2}{24}\frac{z^4}{\bar{v}_z^2}-\frac{\alpha}{24}\frac{b^2}{\bar{v}_z^3}z^4\right]$$

$$(r \ge 2\sqrt{\frac{\bar{v}_r}{\alpha}})$$

(6.27)

In approximating $\omega_z(r,z)$ by $\omega_{zr}(r)\cdot\omega_{zz}(z)$, $\omega_{zr}(r)$ and $\omega_{zz}(z)$ are assumed to have no correlation. In practice, ω_z depends on r too, though not too sensitive, particularly at height near $z=0$. Although the variation of ω_z with z is included and agrees with experimental vorticity characteristics, there are still inadequacies, particularly when the limits $r \to \infty$ and $z \to \infty$, lead to $V_r \to -\infty, V_z \to \infty$. Such problems appear in both Burgers and Oseen vortices. Taking V_z as

$$(\alpha z + b)\left[\exp\left(-\frac{\alpha r^2}{4\bar{v}_r}\right)\right]$$ would avoid having a divergent solution, but resulting in an equation more difficult to solve.

6.3 Experimental and Numerical Results for Swirling Flames

Variation of vertical velocity with height above the fuel surface was estimated in the three cases SW-S, SW-M and SW-L, with results plotted in Fig. 6.7. The vertical velocity was less than 1 ms^{-1} at the flame base, increased with height to a maximum

value before dropping down to a lower value. The estimated maximum vertical velocities for all three cases were lower than the experimental values. The upper flame part was an intermittent region with flame jumping up and down. Note that the three curves in Fig. 6.8 for the three cases are different, with maximum vertical velocity occurring at different times. The rate of rise in vertical velocity and the maximum vertical velocity depended on the heat release rate per unit pool surface area. Higher vertical velocity values were observed for higher heat release rates. As indicated in Fig. 6.7 and Fig. 6.8, the maximum vertical velocity was found in the intermittent region below the maximum flame height.
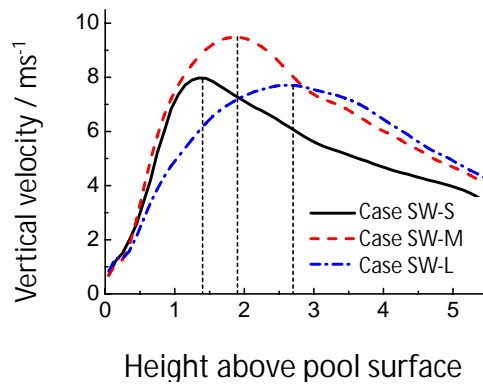
Fig. 6.8: Variation of vertical velocity with height of fire whirl. Dotted lines indicate the average flame height of fire whirl.

The velocity component V_θ could not be measured accurately. Variation of V_z, maximum flame height h_0 and radius of the swirling r_m were estimated from the three cases in Fig. 6.8 to give the variation of V_z with height z in Fig. 6.7 by taking heat release rates into account. Variation of vertical velocity with height for a swirling flame is similar to the variation of heat release rate.

It is easy to observe the flame height when a fire whirl is generated. With a simple theory and estimated method, indirect rotating angular velocity can be determined more conveniently than using sophisticated instrument. It is because the angular velocity in the flaming region is difficult to measure.

Variation of the ratio of axial velocity V_z to tangential velocity V_θ with height in a flame surface is plotted in Fig. 6.9. Based on this ratio the flaming region can be divided into three zones:

- Zone I : Vigorous swirling flame, $V_z/V_\theta < 0.8$, baroclinic force dominates as in H2 region of Table 1.
- Zone II : Flame transition zone, $0.8 \le V_z/V_\theta < 1.2$, baroclinic force similar to buoyancy as in H3 region of Table 1.
- Zone III : Buoyant flame zone, $V_z/V_\theta \ge 1.2$, buoyancy greater than baroclinic force as in H4 region of Table 6.1.
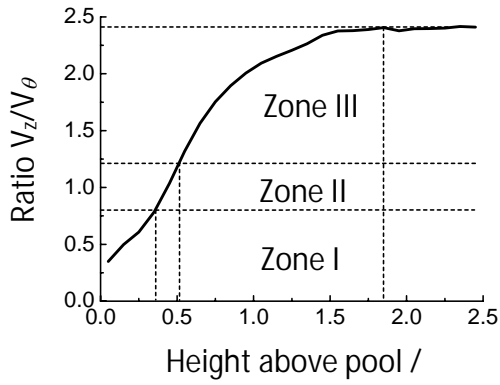
(a) SW-S
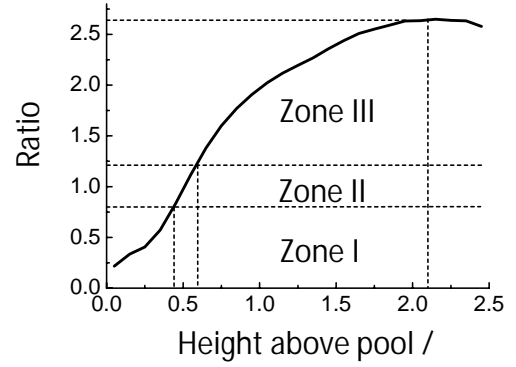
(b) SW-M
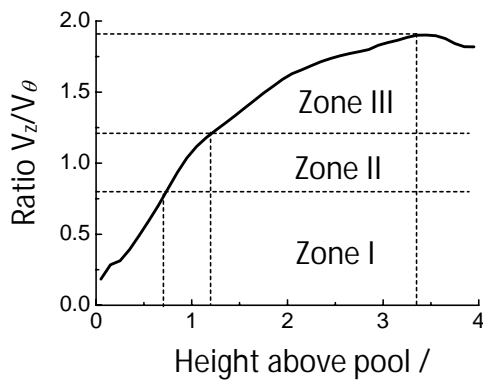
(c) SW-L

Fig. 6.9: Variation of the ratio of V_z/V_θ with height

Note that the five zones in Fig. 6.4 show typical movement of flame in the fire whirl. The angles 0°, 30°, 45°, 60°, 90° angles chosen just for illustrating typical cases.

To simplify the analysis for the flame height (taken as h_0), take $\omega_{zz}=0$ at $z=h_0$.

Taking the first two terms on the right-hand side of equation (6.12),

$$\bar{v}_z \approx \frac{\alpha h_0^2}{2}$$

From equation (6.19),

$$\bar{V}_r \approx \frac{\alpha r_m^2}{4 \times 1.1207^2}$$

In general, r_m can be taken as the flame swirling radius rather than the pool fire radius.

V_θ reaches the maximum value $V_{\theta max}$ at the swirling radius r_m as shown in equation (6.23). Note that $\dfrac{dV_z}{dz}$ in equation (6.19) can be determined from experimental data.

6.4 Empirical Expressions for Pool Fires of Different Size

By dividing the flame into three sections following the above equations, three relations on vertical velocity were deduced from the fire whirl experiments of the three pool fires in Fig. 6.10:

Small pool (SW-S):

$$\left[\begin{array}{lll} V_z = \alpha_1 z + b_1 = 4.63z + 0.52 & 0\ \text{m} < z \le 0.49\ \text{m} & \\ V_z = \alpha_2 z + b_2 = 9.07z - 1.65 & 0.49\ \text{m} < z \le 0.94\ \text{m} & (6.28) \\ V_z = \alpha_3 z + b_3 = 3.33z + 3.74 & 0.94\ \text{m} < z \le 1.27\ \text{m} \end{array} \right.$$

Medium pool (SW-M):

$$\left[\begin{array}{lll} V_z = \alpha_1 z + b_1 = 4.56z + 0.39 & 0\ \text{m} < z \le 0.39\ \text{m} & \\ V_z = \alpha_2 z + b_2 = 9.37z - 1.49 & 0.39\ \text{m} < z \le 0.9\ \text{m} & (6.29) \\ V_z = \alpha_3 z + b_3 = 3.64z + 3.67 & 0.9\ \text{m} < z \le 1.54\ \text{m} \end{array} \right.$$
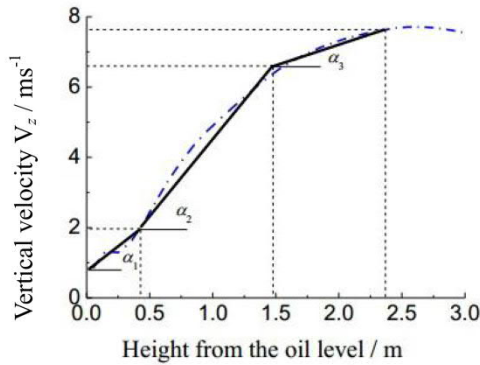
Large pool (SW-L):

$$
\left[
\begin{array}{ll}
V_z = \alpha_1 z + b_1 = 2.67z + 0.81 & 0 \text{ m} < z \leq 0.43 \text{ m} \\
V_z = \alpha_2 z + b_2 = 4.42z + 0.06 & 0.43 \text{ m} < z \leq 1.48 \text{ m} \\
V_z = \alpha_3 z + b_3 = 1.18z + 4.85 & 1.48 \text{ m} < z \leq 2.36 \text{ m}
\end{array}
\right. \tag{6.30}
$$
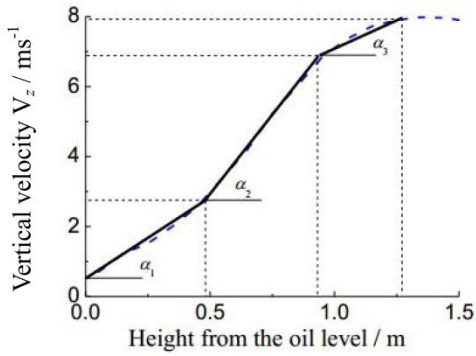
(a) Small pool SW-S
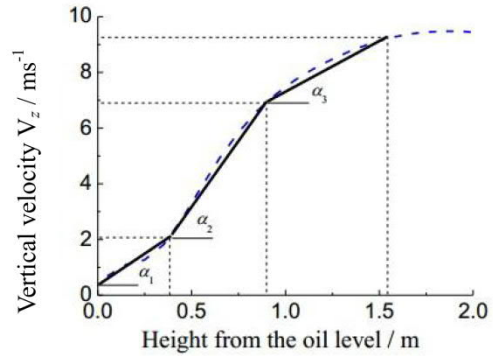
(b) Medium pool SW-M

(c) Large pool SW-L

Fig. 6.10: Vertical velocity in different sections (The blue dotted line is actually calculated, and the black straight solid line is assumed according to the assumption (6.28-6.30))

The dotted lines in Fig. 6.10 come from estimation and experimental correlation in Fig. 6.9.

In equations (6.28) to (6.30), the rotational motions at different heights are assumed to depend on α and b. Five zones are used to describe the properties of swirling

motions. Experimental results above suggested that dividing into is convenient. When

V_z tends to zero, ω_z is approximately maximum at the burning surface, and V_z is

maximum far away from the pool surface, with ω_z approaching zero at h_0. Simple

examples with only baroclinic force or buoyancy were discussed in many textbooks

[71], but both forces are considered in this paper. From the experiments of three pool

fire sizes L, M, S, three solutions for $\dfrac{\partial V_z}{\partial z}$ were obtained for the swirling motion with

viscosity $\overline{V}_r$ and $\overline{V}_z$. Variations of ω_z and V_θ along the z direction are then

deduced. All these results are due to the interactions of baroclinic force and buoyancy

in the three zones. Ignoring cases with V_z being zero or maximum, knowing the

variations of $\dfrac{\partial V_z}{\partial z}$ in three zones are adequate to solve the equation. Variation of $\dfrac{\partial V_z}{\partial z}$

can be deduced from Table 4 in this study. Otherwise, $\omega_z \dfrac{\partial V_z}{\partial z}$ in equation (6.6)

cannot be solved to get the variation of ω_z along z. Equations (6.11) and (6.12) are

then solved. Analytical solutions obtained previously in the literature were of the

Rankine vortex type with the same rotating speed along z. The z change of equations

(6.28-6.30) is limited to the flame length shown in Table 6.4. This can be applied to

tornado, but cannot be applied to strong fire whirl with high temperature difference

between high and low levels.

The pool fire radius r_m for the three experiments SW-S. SW-M and SW-L were 0.1 m,

0.13 m and 0.23 m. Flame heights h_0 were 1.85 m, 2.25 m and 3.2 m as shown as Fig.

6.5 and Fig. 6.6. From equations (6.28) to (6.30), and the measured flame height h_0,

values of α and b can be deduced. Hence, the values of $\overline{V}_r$ and $\overline{V}_z$ are estimated

and given in Table 6.4.

Table 6.1 shows the important different experimental conditions of previous studies to this study. The common quantity measured is the flame height. Meanwhile the corresponding the values of α and b are obtained from equation (6.7). The corresponding values of α, $α_1$, $α_2$, and $α_3$ of the three regions at different times are shown in Fig. 6.10. For $\dfrac{\partial V_z}{\partial z}$ were obtained for the swirling motion with the viscosity dissipation coefficient $\overline{V}_r$ and $\overline{V}_z$ corresponding to different $α$ and b in Table 6.4.

$ω_z(r,z)$ is affected by dissipation of $\overline{V}_r$ and $\overline{V}_z$. Variations of $ω_z$ and $V_θ$ along the z direction are then deduced。How accurate is the valuation velocity depend on V_z and $V_θ$, $α$ and the slope of the line $\dfrac{\partial V_z}{\partial z}$, And the different in Table 6.4 and Fig. 6.10 of $α$ and b.

From equations (6.28) to (6.30) and Table 6.2, variation of $\dfrac{ω_z}{ω_{z\max}}$ and $\dfrac{V_θ}{V_{θ\max}}$ for flame swirling can be deduced. The radial variations of $\dfrac{ω_z}{ω_{z\max}}$ for the three pool fires at different heights are shown in Fig. 6.11(a) to (c). The value of $\dfrac{ω_z}{ω_{z\max}}$ at r = 0 is different, but $\dfrac{ω_z}{ω_{z\max}}$ is lower than 1 when the flame height is less. $\dfrac{ω_z}{ω_{z\max}}$ decreases as the distance away from flame axis increases, and the differences of $\dfrac{ω_z}{ω_{z\max}}$ become smaller and approaches zero eventually. Upon generating a fire whirl, the flame radius

r_m becomes smaller than the pool fire radius. The positions at which $\dfrac{\omega_z}{\omega_{z\max}}$ becomes

0 are 0.2 m, 0.26 m and 0.46 m for the fire pools SW-S, SW-M and SW-L. From these

values, it can be seen that in fire whirl, $\dfrac{\omega_z}{\omega_{z\max}}$ is reduced to zero at radial distance

twice the vortex radius.

Table 6.4: Parameters related to variation of v_z

Tests	Parameters	0 m < z ≤ 0.49 m	0.49 m < z ≤ 0.94 m	0.94 m < z ≤ 1.27 m
SW-S		4.63	9.07	3.33
	b	0.52	-1.65	3.74
	h_0		1.85 m	
	$\overline{v}_z$	7.92	15.52	5.70
	r_m		0.1 m	
	$\overline{v}_r$	0.0092	0.0181	0.0066
	Parameters	0 m < z ≤ 0.39 m	0.39 m < z ≤ 0.9 m	0.9 m < z ≤ 1.54 m
SW-M	α	4.56	9.37	3.64
	b	0.39	-1.49	3.67
	h_0		2.25 m	
	$\overline{v}_z$	11.54	23.72	9.21
	r_m		0.13 m	
	$\overline{v}_r$	0.0153	0.0315	0.0122
	Parameters	0 m < z ≤ 0.43 m	0.43 m < z ≤ 1.48 m	1.48 m < z ≤ 2.36 m
SW-L	α	2.67	4.42	1.18
	b	0.81	0.06	4.85
	h_0		3.2 m	
	$\overline{v}_z$	13.67	22.63	6.04
	r_m		0.23 m	
	$\overline{v}_r$	0.0281	0.0465	0.0124

(a) Small pool SW-S

(b) Medium pool SW-M

(c) Large pool SW-L

(d) At 1 m above fire pool surface
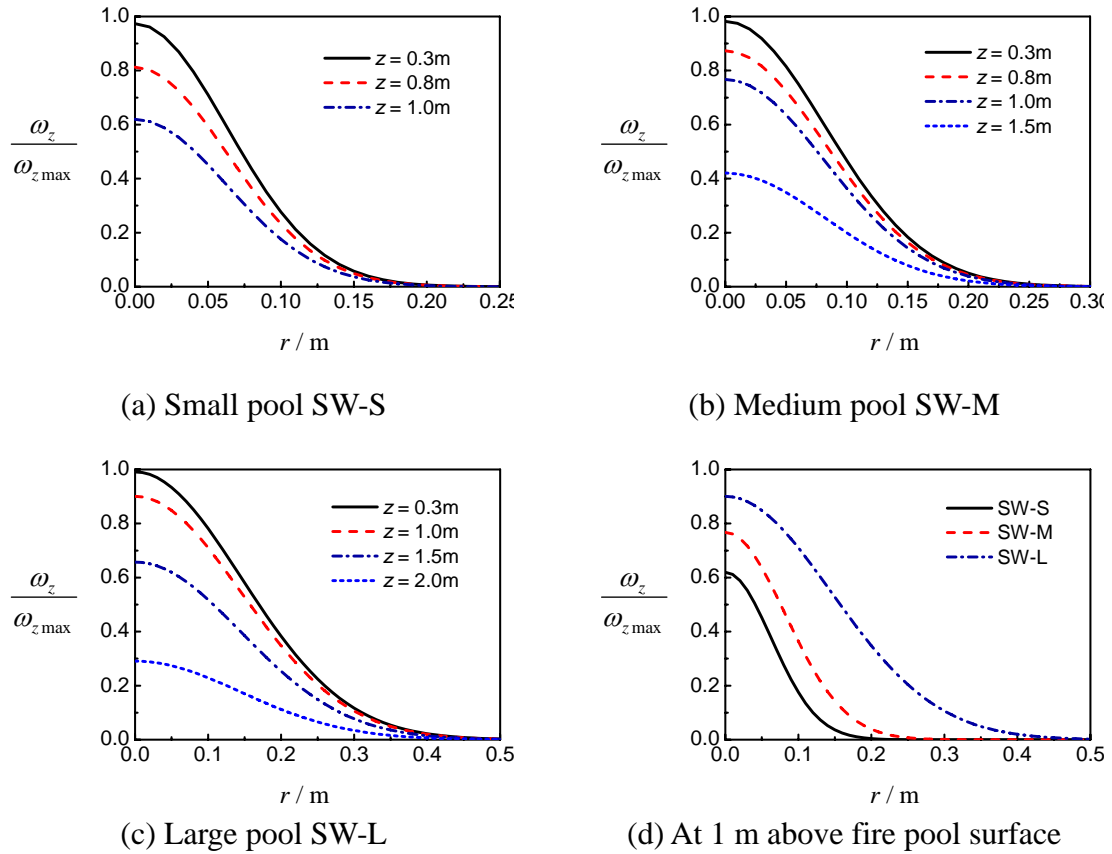
Fig. 6.11: Radial variation of $\dfrac{\omega_z}{\omega_{z\,max}}$ in a fire whirl

Radial variation of $\dfrac{\omega_z}{\omega_{z\,max}}$ for the three experiments at 1 m height are shown in Fig.

6.11(d). The attenuation trends are similar but the value of $\dfrac{\omega_z}{\omega_{z\,max}}$ at $r = 0$ is different.

The value of $\dfrac{\omega_z}{\omega_{z\,max}}$ at $r = 0$ is determined by the heat release rate of the pool fire.

The flame height increases as the heat release rate increases. In equation (6.6), the

$\overline{V}_z$ is the momentum dissipation of ω_z along the z-direction. Small swirling flame

height means the less dissipation. Value of $\dfrac{\omega_z}{\omega_{z\max}}$ is near to 1. For larger pool fires,

the value of $\dfrac{\omega_z}{\omega_{z\max}}$ at $r = 0$ is larger.

The vertical variation of $\dfrac{V_\theta}{V_{\theta\max}}$ for the three experiments in fire whirl is shown in Fig.

6.12. The flame has the largest swirling velocity and giving a value $\dfrac{V_\theta}{V_{\theta\max}}$ of 1 at $z = 0$.

When height is increased, V_θ is reduced, and thus $\dfrac{V_\theta}{V_{\theta\max}}$ is also reduced. With

different pool fire heat release rates and at different heights, the variations of $\dfrac{V_\theta}{V_{\theta\max}}$

are different. At 0.5 m, the small pool fire gives $\dfrac{V_\theta}{V_{\theta\max}}$ a value of 0.93, the medium

pool fire, 0.95, and the large pool fire, 0.97. At 1 m, the values of $\dfrac{V_\theta}{V_{\theta\max}}$ for the small,

medium and large pool fires are 0.66, 0.79 and 0.9, respectively, with a corresponding

decrease of 34%, 21% and 10%, compared with the value at 0.5 m. Thus a higher heat

release rate would give a lower rate of attenuation of $\dfrac{V_\theta}{V_{\theta\max}}$.
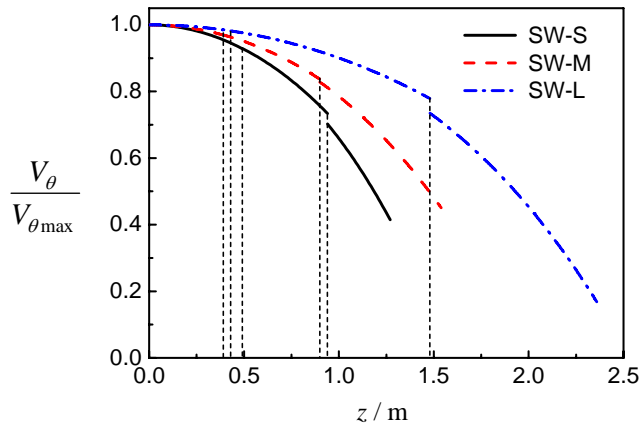
Fig. 6.12: Vertical variation of $\dfrac{V_\theta}{V_{\theta\,max}}$ **in a fire whirl**

As shown in Fig. 6.12, there are two points of discontinuity on each line. The presence of discontinuity points arises from the artificial division of the flame region into the three sections.
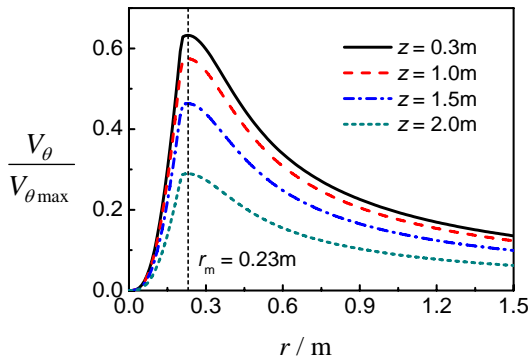
V_z is taken to be the value along the central vertical axis (R=0). V_θ is the value along the z direction at R, now shown in Fig. 6.13.
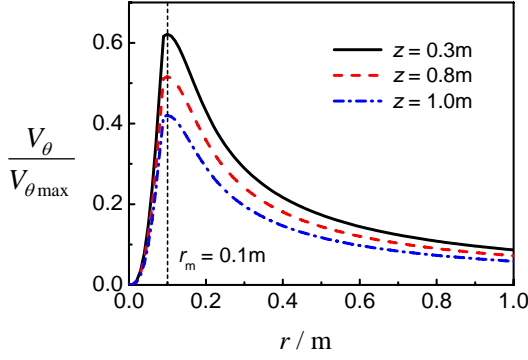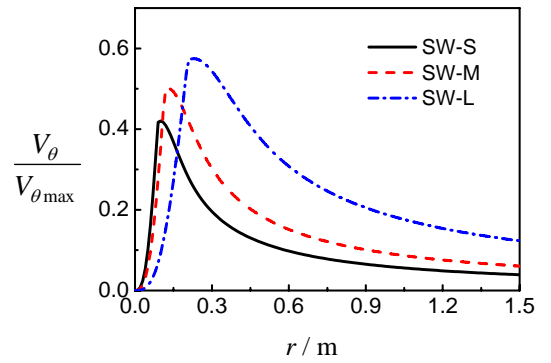
(a) Small pool SW-S
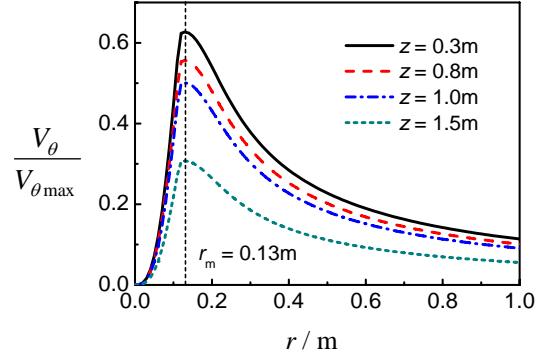
(b) Medium pool SW-M

(c) Large pool SW-L

(d) At 1 m above fire pool surface

Fig. 6.13: Radial variation of $\dfrac{V_\theta}{V_{\theta\max}}$ in a fire whirl

The radial variation of $\dfrac{V_\theta}{V_{\theta\max}}$ is shown in Fig. 6.13(a) to (c). The value of $\dfrac{V_\theta}{V_{\theta\max}}$ is zero at the flame axis, and then increases with r at a rate of r^n ($n>1$) until a maximum is reached at the flame radius r_m. For $r > r_m$ $\dfrac{V_\theta}{V_{\theta\max}}$ decreases. For the same fire, $\dfrac{V_\theta}{V_{\theta\max}}$ decreases as height increases. This indicates that flame swirls more vigorously at lower levels.

The radial variation of $\dfrac{V_\theta}{V_{\theta\max}}$ at 1 m is shown in Fig. 6.13(d) for different pool fires.

It can be seen that a small pool fire (that is, low heat release rate) has small $\dfrac{V_\theta}{V_{\theta\max}}$ at the same height. This further confirms that the heat release rate in a pool fire is a key factor in affecting flame swirling characteristics.

Chapter 7.

Experimental and Numerical Studies on Swirling of Internal Fire Whirls

The formation of fire whirl is due to the coupling of upward airflow caused by buoyancy and tangential airflow. Angular momentum was believed to be the key element. Some vertical shaft fire whirl experiments have been done [19,73-74] to study the impact of gap width on flame intensity. Recent studies [17] suggested that fire whirl burnt vigorously when the ratio of gap width to wall width was in a certain range. No velocity field of fire whirl was measured or analyzed by their studies. A series of comprehensive experimental investigations [15,75] was carried out with hot-wire anemometers to precisely measure the velocity at key positions. Semi-empirical formula was used [35] with the assumption that turbulent fire whirl height could be calculated based on turbulence suppression. By analysing Richardson Number, turbulent fire whirl suppression was attributed to the decrease of mixing length and plume expansion rate. The flame height, heat release rate, average axial velocity and the Richardson number were interrelated. Comparing with fires of the same fuel pool size, turbulence suppression was suggested to be the dominant mechanism of fire whirl elongation rate. Chuah et al. [48] clarified that flame height was determined by the vortex core diameter. Since the average heat transfer rate to the burning surface varied inversely to the vortex core diameter, smaller vortex core transferred more heat to the fuel surface and led to higher evaporation rate.

Numerical simulation [76-77] of fire field, for its nearly unlimited data details, is a good addition to experiment. Previous researches [78-80] have discussed the application of large eddy simulation to fire field computation and good performance

has been reported. Satoh and Yang [81] carried out simulation by using an approximate fire field model and by directly defining total heat load without experimental guideline. Chow et al. [82] presented a mathematical method to study the relationship between burning rate and fire whirl height. Moreover, simulation with the k-ε turbulent model and commercial software Fluent was presented but relationships between the parameters of fire whirl were not discussed in depth. Experiment and numerical simulation [11] suggested that standard and modified turbulent model did affect the simulated fire whirl height. Good agreement between experiment and simulation could be obtained when modified turbulent viscosity was utilized. In the numerical simulation, the author got results agreeing with the experimental results by enlarging turbulence suppression. Motivated by these experiences, LES method was used in this paper.

The reliability of the fire field simulation is based on the verification versus experiment. In this paper, medium-scale experimental observations were presented to investigate the features of fire whirl, including fuel burning rate, flame height and temperature. The IFW was divided into six stages from generation to extinction. The Fire Dynamics Simulator (FDS) was used to simulate the IFW using a fire source with heat release rate (HRR) compiled from experimental data. Taking HRR as FDS input parameters, good agreement between simulated and experimental IFW transient flame surface, flame height, and temperature were achieved. Furthermore, axial (vertical) and tangential velocity, streamline, velocity vector and vortex core were obtained.

7.1 Experimental Studies

A 2.1 m x 2.1 m square vertical shaft 9 m tall with a corner gap of adjustable width as shown in Fig. 7.1(a) was constructed. A glass wall of 2.0 m × 1.5 m was installed for observing flame whirling motions. The other walls were made of iron sheets. Gasoline pens of different diameters were put at centre of the floor.

The gap width was set as 0.33 m to provide a strong flame swirling. Thermocouples were put in positions as shown in Fig. 7.1(b). Different horizontal thermocouple distributions were set for different pool size. Tests for gasoline diameters of 0.2 m, 0.26 m and 0.46 m were labelled as SW-S, SW-M and SW-L. Experimental parameters in these tests and results are shown in Table 7.1.

As observed in the experiments, there were 6 stages in the IFW from ignition to stable swirling and then extinction, as summarized in Table 7.2.

- Stage I:

    Behaved as a normal pool fire with gas and air temperature increased.

- Stage II:

    Inclined pool fire with centerline temperature decreased.

- Stage III:

    Transition from a normal pool fire to elongated flame height, swirling observed intermittently with temperature rising rapidly.

- Stage IV:

    Inclined fire whirl rotated around central axis with temperature fluctuating.

- Stage V:

    Straight fire whirl with strong swirling flame and steady temperature measured.

108

•Stage VI:

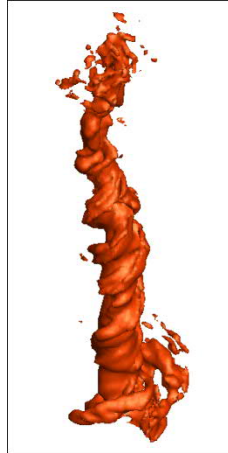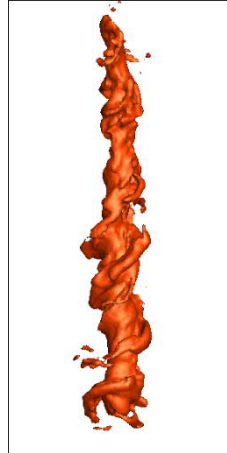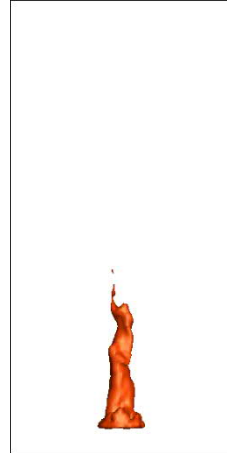Flame swirling decayed with decreasing flame diameter and height until extinction.
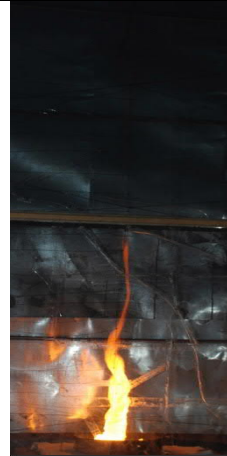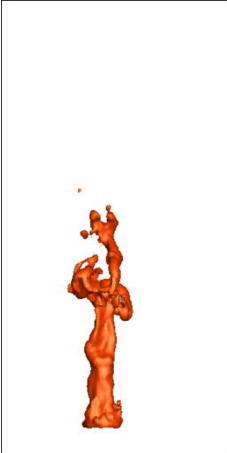
Measured axial and horizontal temperature distributions for the three different fire pools were shown in Fig. 7.2 and Fig. 7.3. For smaller fuel pool diameter, stage I and II were longer, which mean that the onset of fire whirl was later than bigger ones. Axial temperature rose up to the highest at the end of the transition stage III and then IFW was formed. Stage IV and stage V alternating existence after IFW generation. By comparing SW-S, SW-M and SW-L, large temperature fluctuations were observed for small pool diameters. Non-uniform density difference due to buoyancy was probably the reason of tangential wind generation. IFW trended to be generated easier with fire source having higher HRR.

The transient fuel mass was measured by an electronic scale placed under the fuel pool and was shown in Fig. 7.4. As the fuel loss rate fluctuation was small, no significant fluctuation on transient fuel mass was observed. The slope in the time interval (200 s to 250 s) of the three curves would give the stage V burning rate. The negative mass readings occurred at the end of combustion due to hot steam and negative pressure above the fuel tray resulted from high temperature.

Table 7.1. Experimental parameters and results

Label	Fuel diameter (m)	Mass (kg)	Fuel depth (cm)	HRR estimated from burning rate (kW)		Fuel burning rate (gs^{-1})		Burning time (s)	Maximum flame height (m)	Mean flame height (m)
				Mean($\bar{Q}$)	Stage V(Q)	Mean	Stage V			
SW-S	0.2	0.91	4	103.4	125.1	2.8	3.4	330	1.85	1.46
SW-M	0.26	1.53	4	173.0	213.4	4.7	5.8	327	2.25	1.81
SW-L	0.46	4.81	4	441.6	552.0	12.0	15.1	401	`3.2	2.5

Table 7.2. Experimental and simulated flame phase of SW-L

Stage	I	II	III	IV	V	VI
Flame phase	Ordinary pool fire	Inclined pool fire	Transition fire	Inclined fire whirl	Straight fire whirl	Weak straight fire whirl
Experi-mental patterns						
Corres-ponding CFD patterns						
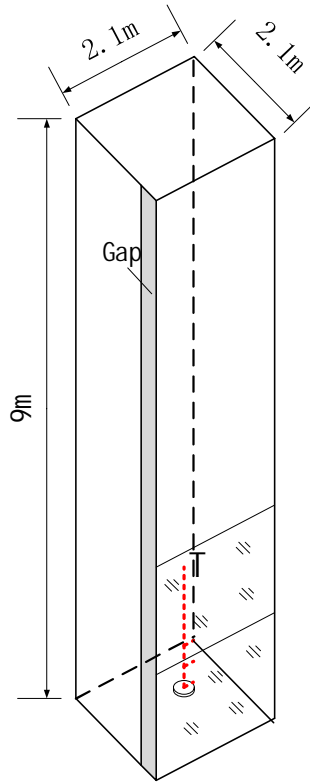
(a) The rig
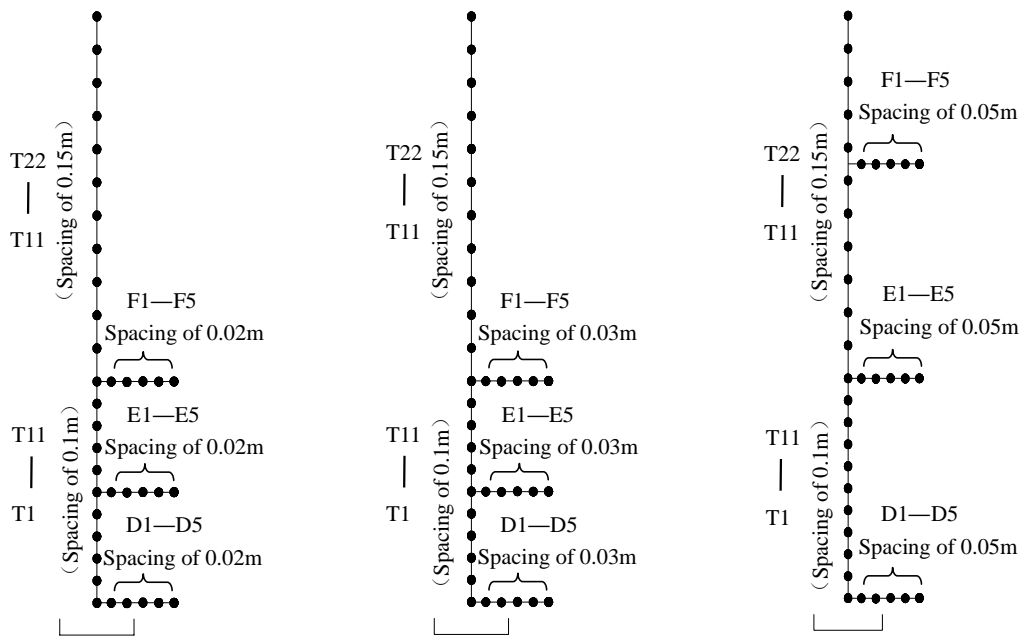
(i) 0.2 m diameter   (ii) 0.26 m diameter   (iii) 0.46 m diameter

(b) Temperature measurement points for different gasoline pool diameters
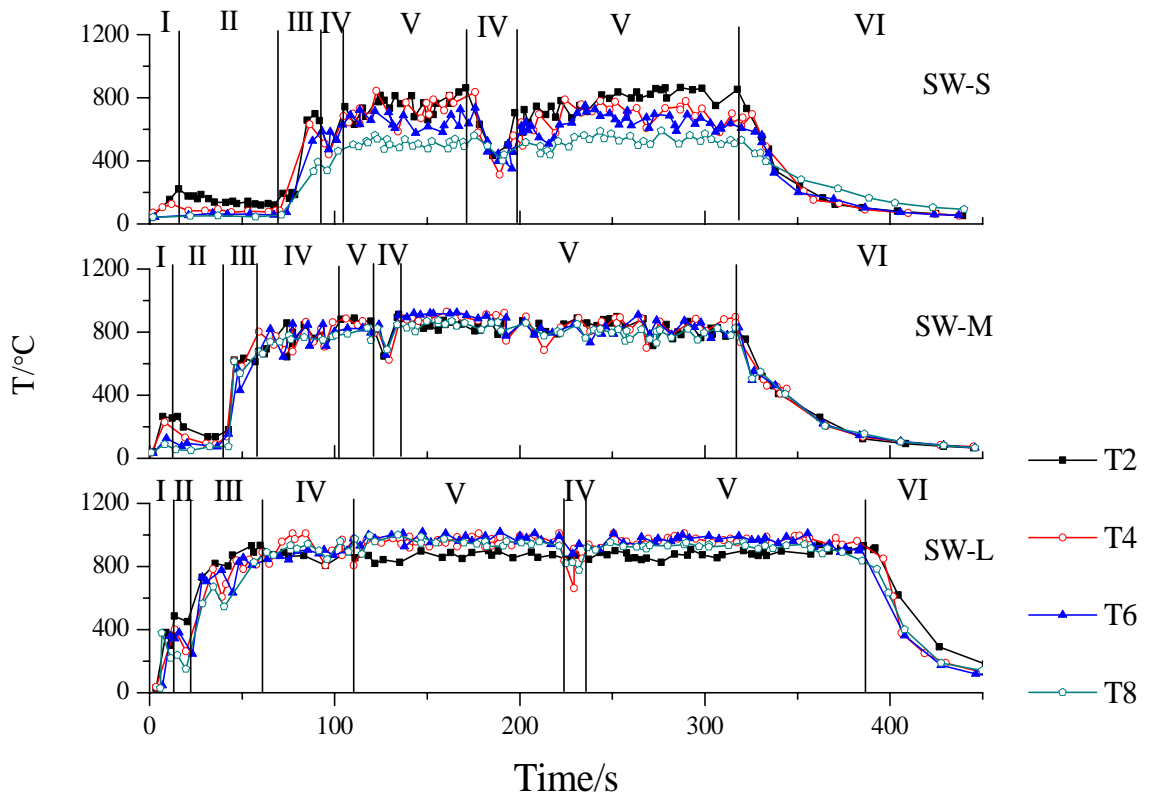
Fig. 7.1: Vertical shaft

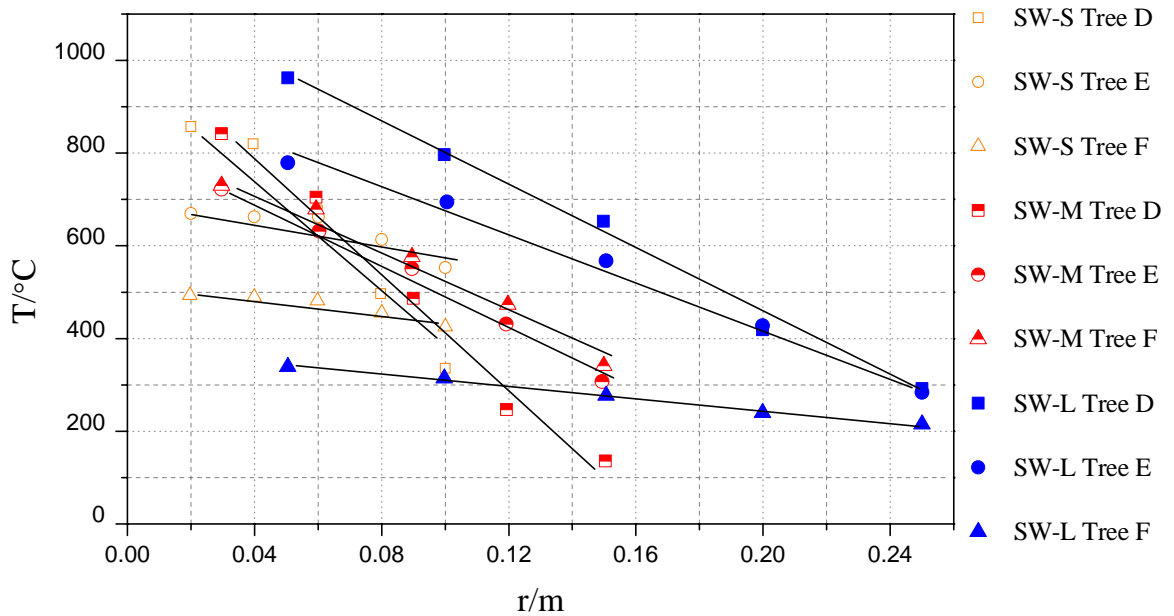**Fig. 7.2: Central gas temperatures under 0.8 m**

Fig. 7.3: Radial gas temperatures at different heights
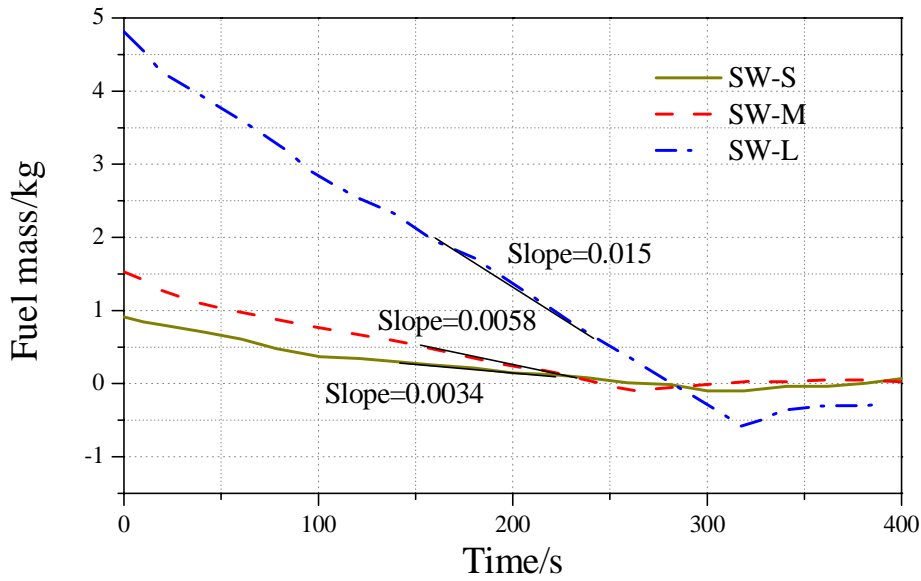
Fig. 7.4: Transient fuel mass

7.2 Numerical Simulation

The Computational Fluid Dynamics (CFD) software Fire Dynamics Simulator (FDS) is used to simulate the IFW. The simulation results are compared with the experimental data to validate the selected models. Three simulations are conducted corresponding to the above experiments labeled as SW-S, SW-M and SW-L. Based on experimental results, a fire source which heat release rate varying with time is set up. The finite volume method (FVM) as radiation model, the Large Eddy Simulation (LES) method as turbulent model with Subgrid scale (SGS) turbulence Smagorinsky model are used.

SGS Smagorinsky model has been demonstrated to be successful in studying buoyant flames by Zhou et al. [83], using a viscous stress $\tau_{ij,SGS}$ shown below.

$$\tau_{ij,SGS} - \frac{1}{3}\delta_{ij}\tau_{kk,SGS} = 2\mu_T \bar{S}_{ij} \tag{7.1}$$

where

Turbulent viscosity coefficient: $\mu_T = \bar{\rho}(C_S\Delta)^2(2\bar{S}_{ij}\bar{S}_{ij})^{1/2}$ (7.2)

and deformation rate tensor: $\bar{S}_{ij} = \frac{1}{2}(\frac{\partial \bar{u}_i}{\partial x_j} + \frac{\partial \bar{u}_j}{\partial x_i})$ (7.3)

$$\tau_{ij,SGS} = \mu_T(2\bar{S}_{ij} - \frac{2}{3}\delta_{ij}\bar{S}_{kk}) \tag{7.4}$$

Then turbulent viscosity coefficient is given by

$$\mu_T = \bar{\rho}(C_S\Delta)^2|S| = \bar{\rho}(C_S\Delta)^2\left\{-\frac{2}{3}(\bar{S}_{kk}\delta_{ij})^2 + 2(\bar{S}_{ij})^2\right\}^{1/2} \tag{7.5}$$

The subgrid length Δ is expressed as $\Delta = (\Delta x, \Delta y, \Delta z)^{1/3}$, C_S is taken to be within

0.1~0.25.

Applying literature results in studying turbulent flow [84], the species diffusion vector

is given by:

$$-\bar{\rho}(\overline{Y_l u_j} - \bar{Y}_l\bar{u}_j) = \frac{\mu_T}{Sc_T}\frac{\partial \bar{Y}_l}{\partial x_j} \tag{7.6}$$

The heat flux vector is

$$-\bar{\rho}(\overline{Tu_j} - \bar{T}\bar{u}_j) = \frac{\mu_T}{Pr_T}\frac{\partial \bar{T}}{\partial x_j} \tag{7.7}$$

The heat-conductivity factor k_T and mass diffusion coefficient D_T are given by:

$$k_T = \frac{\mu_T C_P}{Pr_T} \qquad (7.8)$$

$$\rho D_T = \frac{\mu_T}{Sc_T} \qquad (7.9)$$

Smagorinsky constant C_S, turbulent Schmidt number Sc_T and turbulent Prandtl number Pr_T have to be specified in the Smagorinsky model. According to the results of previous studies, C_S is not sensitive when the grid is small enough [76]. The value of C_S has an impact on the simulation results when buoyancy is strong. A greater C_S is recommended [85] when the grids are not fine enough. Values of Sc_T and Pr_T have little effect on simulation results. FDS numerical simulation applying SGS model for ordinary pool fire was conducted [86] by taking $C_S = 0.2$, $Pr_T = 0.7$, $Sc_T = 0.3$. Combining studies by different scolar [78-80], $C_S = 0.2$, $Pr_T = 0.5$, $Sc_T = 0.5$ are used in this paper.

Uniform Cartesian coordinate grids are used. In order to exactly capture the fire whirl details such as vortex, the grid size is determined by the flame characteristic diameter $D*$ and grid size l. $D*/l$ can be seen as the amount of grid in characteristic length. Reasonable results are obtained when $D*/l$ lies between 4 and 16 [54] with $D*$ given by:

$$D* = \left(\frac{\bar{Q}}{\rho_0 c_P T_0 \sqrt{g}} \right)^{\frac{2}{5}} \qquad (7.10)$$

Characteristic diameter $D*$ should cover [87] at least 10 grids to capture the fire plume. Taking ρ_0= 1.293 kg/m^3, c_P= 1.004 kJ/kg·K, g=9.8 kg/s^2, the calculated grid size is shown in Table 7.3.

Table 7.3. Grids of different cases

Simulation Number	q (kW)	$D*$	Grid size (m)	Grid size in flame zone (m)
SW-S	125.1	0.35	0.035	0.03
SW-M	213.4	0.45	0.045	0.03
SW-L	552	0.65	0.065	0.05

For simulating SW-L, the selected grid size is 0.05 m × 0.05 m × 0.05 m. The total number of grids is 42 × 42 × 183. For SW-S and SW-M, a smaller grid size of 0.03m was needed to capture flame data. If the grid size of the whole simulation zone is set to be 0.03 m × 0.03 m × 0.03 m, the total number of grids is nearly 1.5 million.

The whole computing domain is then divided into several parts to achieve simulated results. A region of 0.9 m × 0.9 m × 6.0 m around the flame is set as the flame zone, where 0.03 m × 0.03 m × 0.03 m grid is used. The other region is set as the flame far field, where 0.05 m × 0.05 m × 0.05 grid is used. The total number of grids is 0.46 million and the grid setting is shown in Fig. 7.6. Free boundary conditions on the gap and roof are set to allow fluid flowing across. The velocity and temperature gradients at these boundaries are set to zero.

The estimated total HRR of these three experiments at IFW stable stage are Q =125.1 kW, 213.4 kW, and 552 kW, respectively, higher than the mean HRR over the six stages denoted by $\bar{Q}$ (in kW). The simulated input stable-stage HRR Q_{in} (in kW)

should be equal to Q. Meanwhile, the input mean HRR $\overline{Q}_{in}$ should be equal to $\overline{Q}$ (obtained from average fuel loss rate in Fig. 7.5) too. After stage IV, a stable fire whirl formed. The end time of stage IV is the end of the ascent of the input HRR curve. When the stage VI begins, the fire whirl starts to extinguish, and the IFW is no more stable with the HRR curve starts to decrease, $Q_{in}=Q$. In this way, one can find that the mean input HRR is $\overline{Q}_{in}$= 99.5 kW, 168 kW and 440.5 kW, very close to estimated mean HRR $\overline{Q}$=103.4 kW, 173 kW and 441.6 kW.

Predicted flame temperature, flame height and flame pattern are compared with experimental results first to validate the simulation method using FDS. Flame axial velocity and tangential velocity are then studied by CFD-FDS.
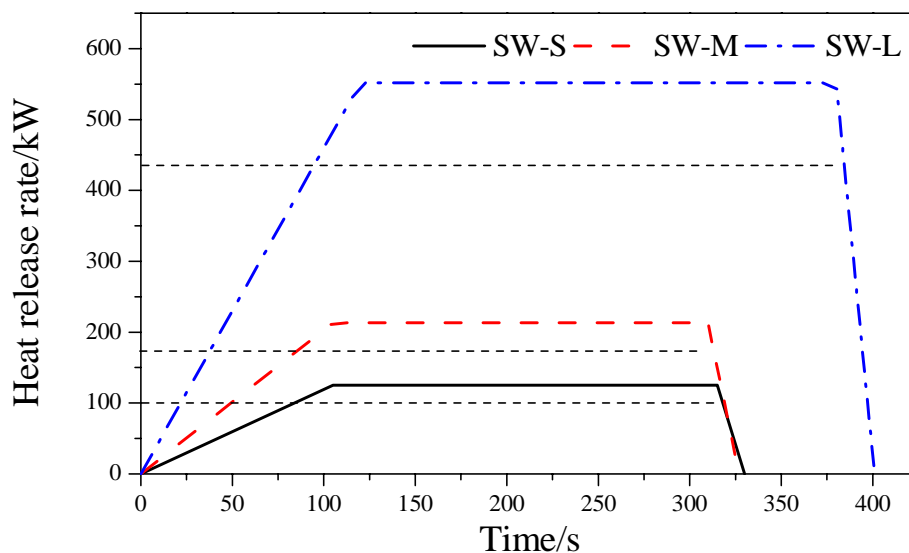
Fig. 7.5: Input HRRs in simulations. The horizontal section corresponding to experimental stable fire whirl stage HRR. $\overline{Q}_{in}$ =99.5 kW, 168 kW and 440.5 kW respectively.

(a) Shaft model   (b) Uniform grids (SW-L)   (c) Refined grids to the
                                                            flame region (SW-S,SW-M)

Fig. 7.6: Simulation geometry of model and grid

7.3 Analysis on Flame Surface and Streamline

Simulation results on the central lateral plane of the shaft under different parameters

for SW-L are shown in Fig. 7.7. The IFW length is 3.1 m. The temperature

distribution in Fig. 7.7(a) shows that the transient IFW temperature is not continuous

while the pressure distribution is continuous (Fig. 7.7(b)). In Fig. 7.7(c) and Fig.

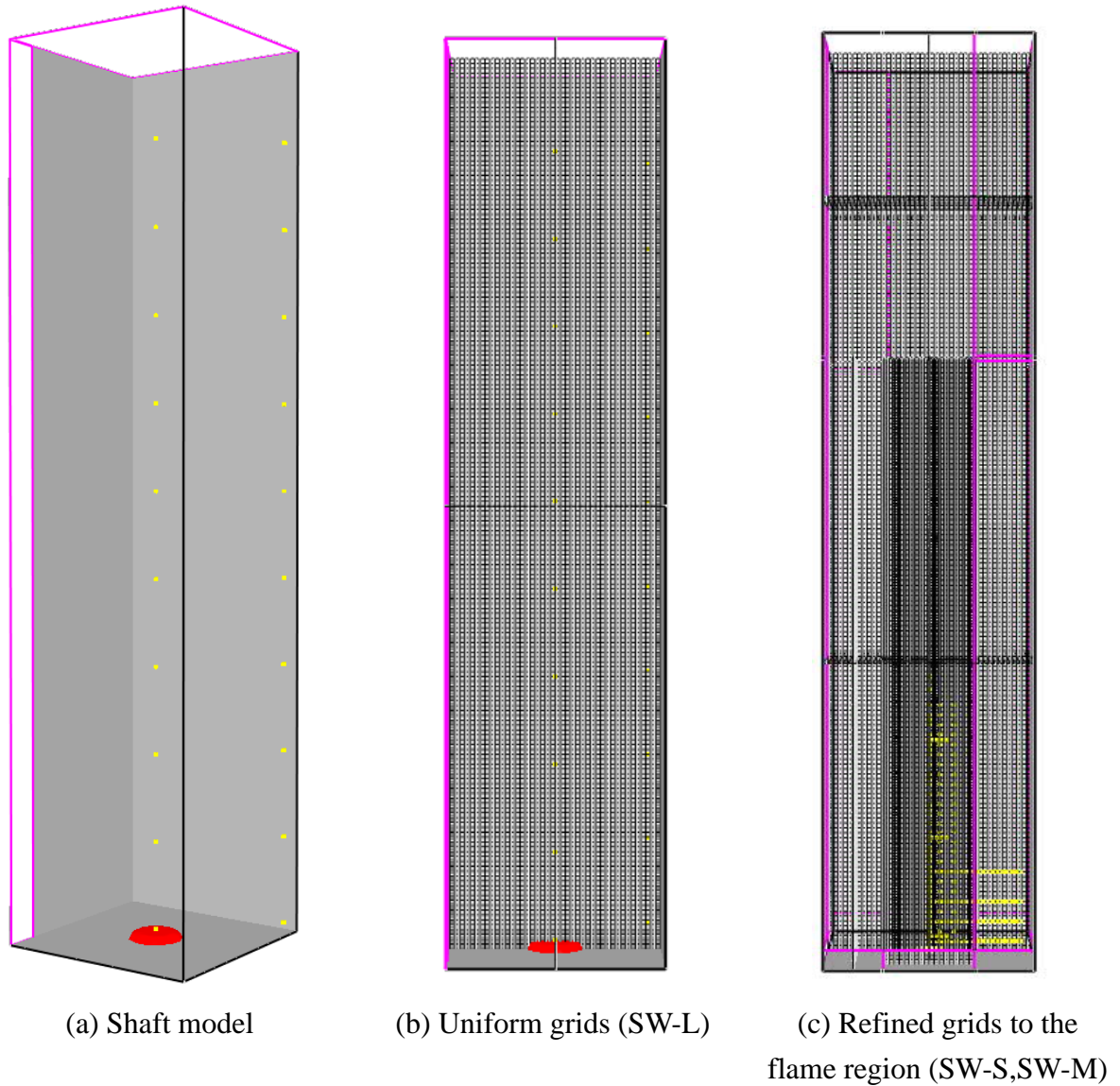7.7(d), the velocity on the centerline and v at the lower part is smaller than the other regions in IFW. The vertical velocity w is shown in Fig. 7.7(e).

Stable strong fire whirl could be generated in the simulation of the three cases corresponding to SW-S, SW-M and SW-L. The flame height has been defined [88] to be the region having a temperature of 500–600℃. In fact, a temperature of 550℃ has been used to denote maximum flaming regions. [18,89] Taking 550℃ as flame surface temperature, the spiral flame surface of 0.46 m fuel diameter agrees well with the experimental pattern. The 6 stages of fire whirl from generation to extinction are validated by comparing the experimental and simulated flame phases (Table 7.2).

Stage I simulated pattern is different from the experimental one due to assuming a linearly increasing HRR in the CFD input. Stage II simulated pattern inclines to the gap because of the air distribution. Gas temperature rises due to combustion and leads to stronger buoyancy with increased entrained air velocity. When the uneven velocity field is coupled with the buoyancy field, the flame starts to transit to IFW in Stage III. As the coupled field becomes steady, an inclined IFW (Stage IV) and a stable IFW (Stage V) are then formed.

CFD-FDS results for streamline is shown in Fig. 7.8(a). IFW of SW-L trends to be more slender. The streamline of larger fuel diameter is more concentrated and higher than the others, which means that it has stronger and steady airflow. Spiral streamlines are observed and air is mainly entrained from the base of gap. The lower part of the flame swirls more strongly. As height increases, the swirling streamline decays. The top views of the velocity vectors across flame base are shown in Fig. 7.8(b). A larger fuel diameter leads to stronger fire whirl.

<div align="center">(a) T   (b) P   (c)V   (d) v (e) w</div>
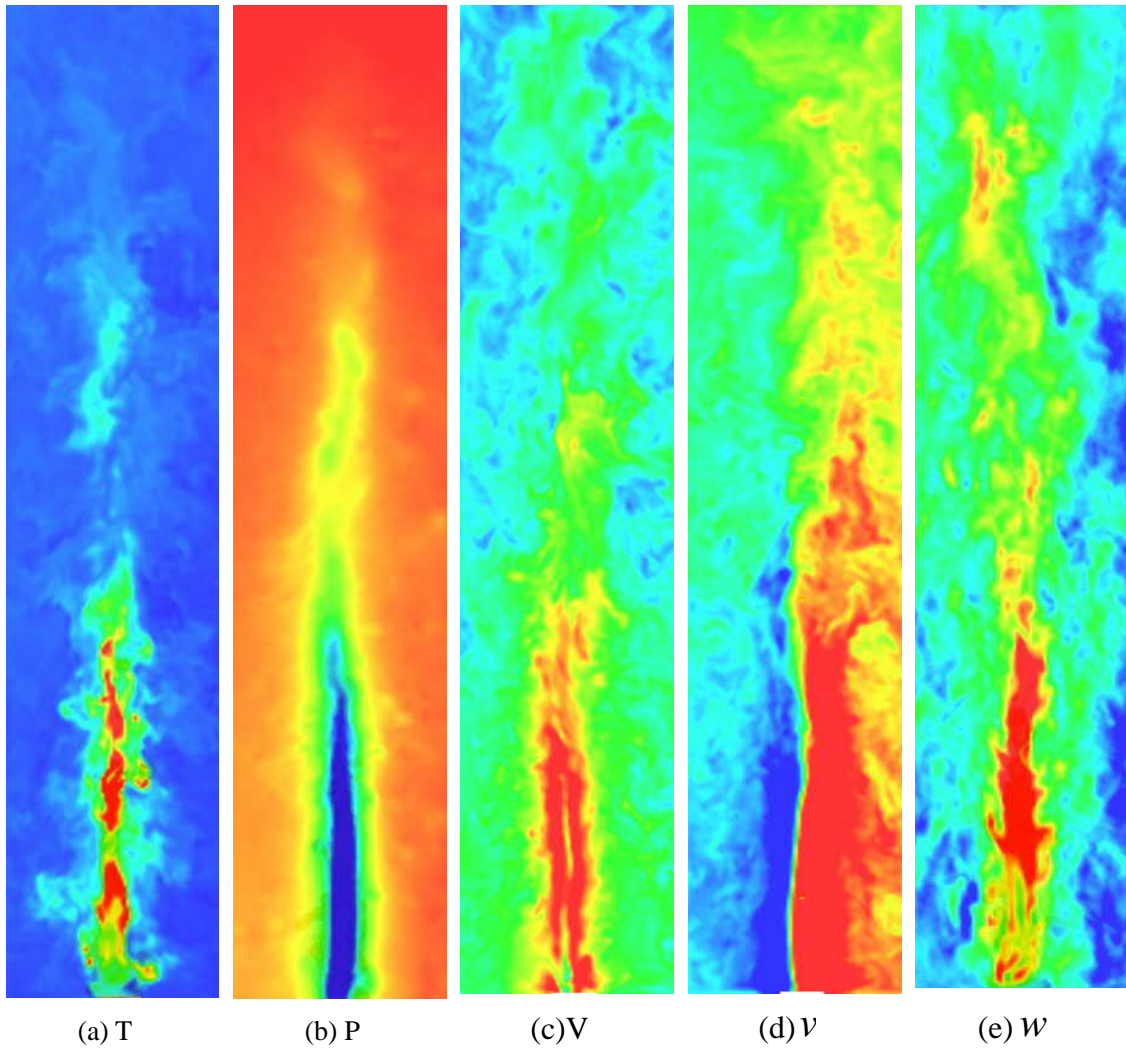
Fig. 7.7: SW-L simulated results. (a)Temperature varied 20-870 $^\circ C$ (b)Pressure varied -90~2 Pa. (c) Velocity varied 0~8.5 m/s. (d) v varied -5.5~4.5 m/s. (e) w varied -1.3~8.7 m/s. t=150s. Blue represents small value and red represents large value.
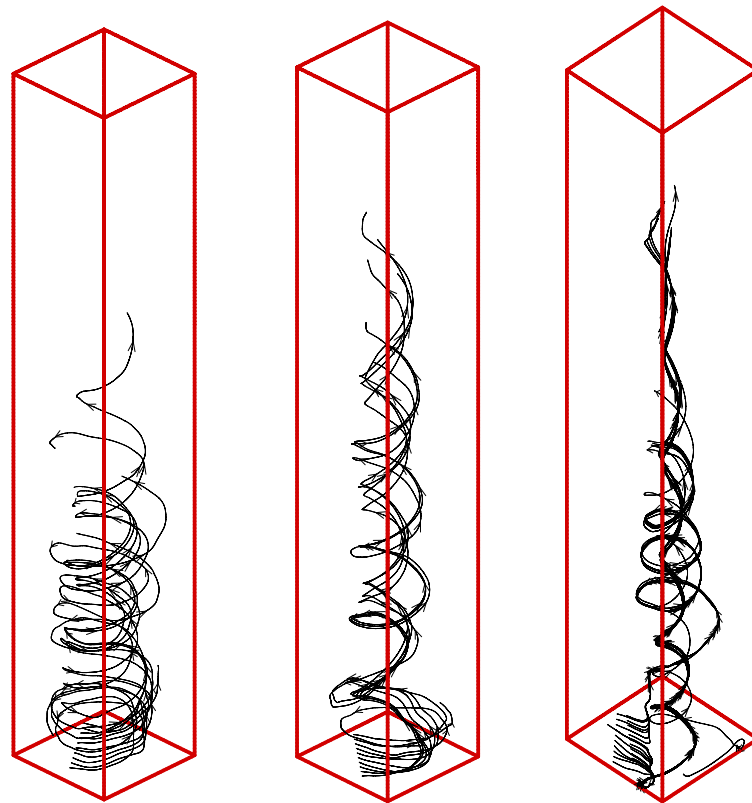
|(i) SW-S|(ii) SW-M|(iii) SW-L|
(a) Streamline of three IFWs

|(i) SW-S|(ii) SW-M|(iii) SW-L|
(b) Velocity vector of three IFWs

Fig. 7.8: Stage V streamline (a) and velocity vector (b) at $z = 0.5$ m

7.4 Analysis on Temperature

An ordinary pool fire is divided into the flame region, intermittent region and plume region as in [90]. The centerline temperature varies with height as

$$\frac{2g\Delta T}{T_0} = k^2 (\frac{z}{Q})^\eta \tag{7.11}$$

The characteristic region of flame corresponds to $z/Q^{2/5}$ and comparisons between an ordinary pool fire and an IFW are shown in Table 7.4.

Table 7.4. Parameter differences between pool fire and IFW

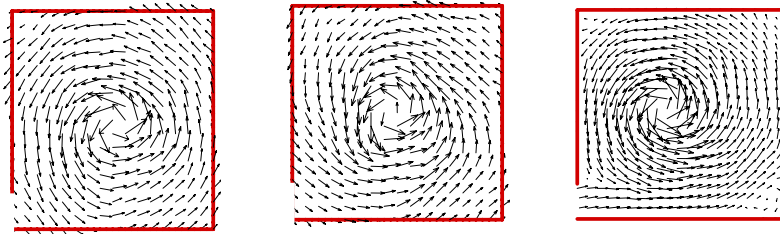| Region	Pool fire			IFW		
	k	η	$z/Q^{2/5}$ (m/kW$^{2/5}$)	k	η	$z/Q^{2/5}$ (m/kW$^{2/5}$)
Flame	7.5m$^{1/2}$/s	0	<0.08	7.7 m$^{1/2}$/s	0.3	<0.1
Intermittent	2.1m/kW$^{1/5}\cdot$ s	-1	0.08-0.2	4.4 m/kW$^{1/5}\cdot$ s	-0.42	0.1-0.25
Plume	1.2 m/kW$^{1/3}\cdot$ s	-5/3	>0.2	2 m/kW$^{1/3}\cdot$ s	-1.58	>0.25

The IFW flame region and intermittent region are longer than those in a pool fire. Fig. 7.9 shows the experimental and simulated temperature distribution comparing with McCaffrey's pool fire centerline temperature [90]. Similar empirical formula is applicable to an IFW too. It can be seen that for the pool fire flame region the average temperature of centerline is nearly constant, but falls in the intermittent region to about 320°C. However, the IFW average temperature rises a little in the flame region. This is because stronger fuel vaporization and air entrained at lower part consume more heat. At the end of the intermittent region, the centerline temperature falls to 490°C, significantly higher than that of pool fire. Thus, one would expect taking 550°C as the flame surface is appropriate. Taking 550°C as the flame surface temperature, in the three simulated cases, the flames height is 1.7 m, 2.25 m and 3.15

m respectively. Photographs taken by Bullen and Thomas [89] during the experiments suggest that this might underestimate the height by ~10%. Experimental results are 1.85 m, 2.25 m and 3.2 m, indicating good matching with results of simulation.
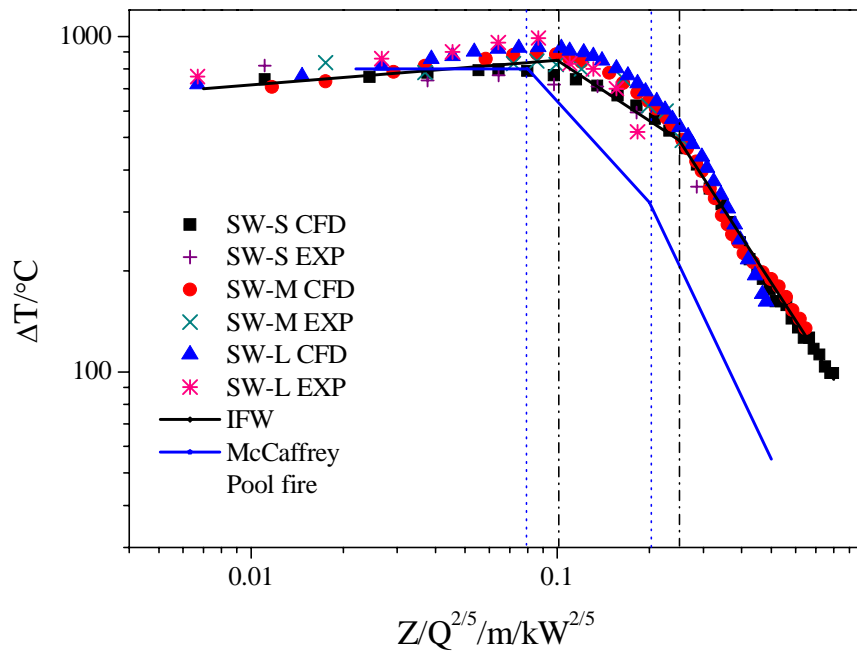
Fig. 7.9: Centerline excess temperature versus z/Q$^{2/5}$

In Fig. 7.10, Tree D simulated temperature is higher than the experimental temperature while Tree E and F are not. Usually simulated results trend to overestimate temperature, but strong entrained air current at the base (Fig. 7.8 (a)) would result in a lower simulated temperature.
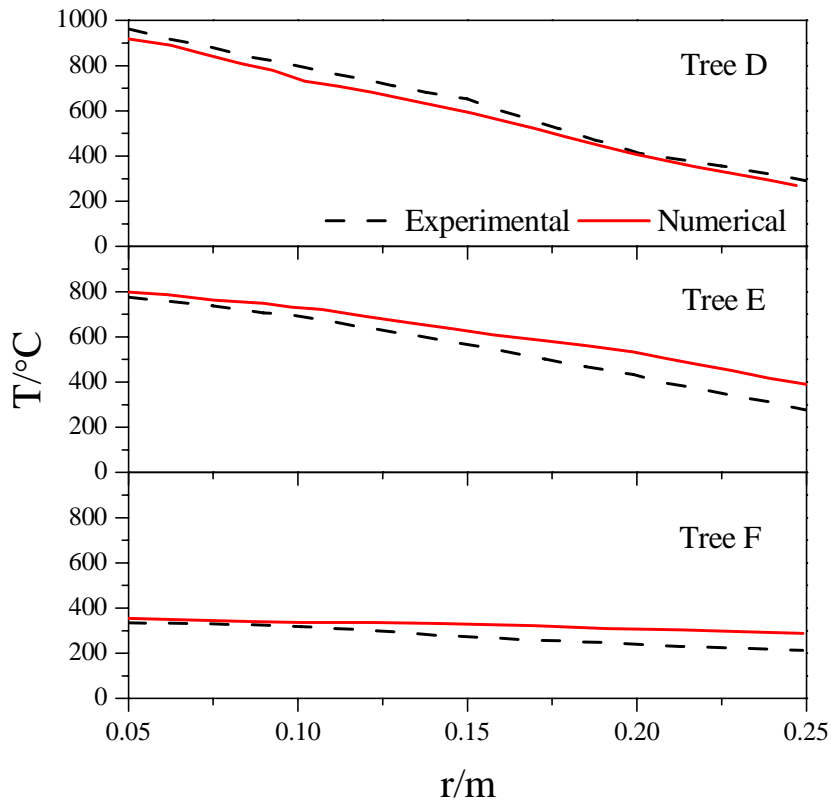
Fig. 7.10: Comparisons between experimental and numerical radial temperatures with 0.46 m diameter fire

7.5 Analysis on Tangential and Axial Velocity

Variation of tangential velocity along the radial length at different height (0.1 m, 0.3 m, 0.5 m and 0.8 m above the surface of fire pool) for the three cases are shown in Fig. 7.11. Trends of the four curves in the three cases are similar. The maximum tangential velocity is found on the flame surface, and the radical distance of maximum tangential velocity is equal to the vortex core radius in general. The vortex core radius is very close to the fuel pool radius.
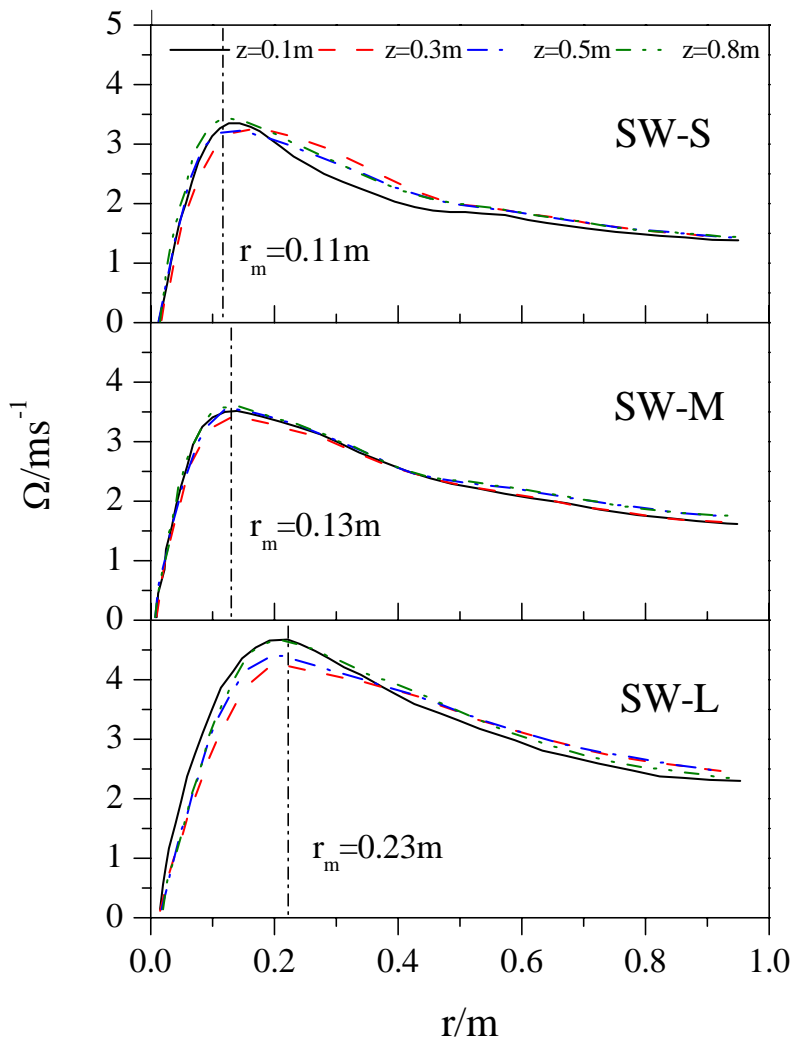
Fig. 7.11: Tangential velocity versus radius at different height

Fig. 7.12 is the vertical distribution of tangential velocity at different radial distances. The tangential velocity is larger at pool radius (vortex core radius) than at other vertical line in or out the IFW, which indicates that air swirls most strongly at the pool radius surface. Also, the tangential velocity fluctuates around $z=0$ at the centerline of the fire whirl. At each radius surface outside the IFW, tangential velocity starts to rise to a maximum at the flame base, and after decreasing a little bit, the tangential

velocity maintains stable with height. The curves reach the peak at 1.36 m, 1.6 m, 0.8 m, and Ω_{max} =3.6 m/s, 3.9 m/s, 4.8 m/s.
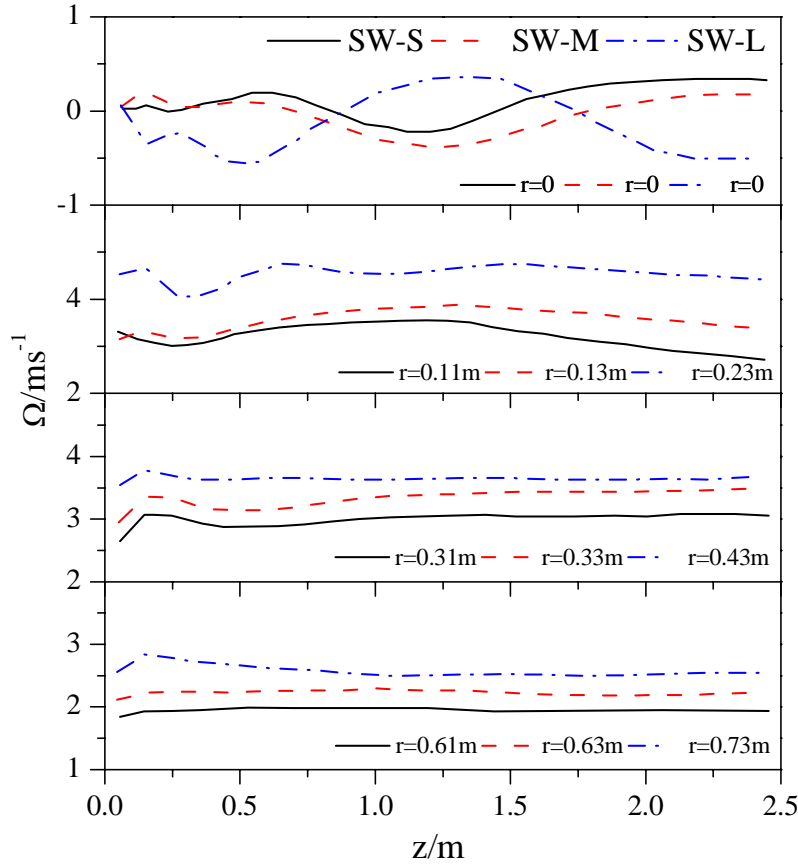
Fig. 7.12: Variation of tangential velocity versus height at different radial location. From top to bottom, $r=0$, $r=r_m$, $r=r_m+0.2$, $r=r_m+0.5$.

Variation of the centerline average velocity of fire whirl with height is shown in Fig. 7.13. It is observed that the centerline axial velocity increases rapidly with height due to increasing density difference and pressure gradient difference until its maximum value is reached. The maximum velocity appears at the average height of the flame. Comparing with McCaffrey's ordinary pool fire axial velocity fitted line, the IFW simulated data are not a function of $Q^{2/5}$ any more. This is because pool fire velocity consists of radial and axial velocity but not tangential velocity. The tangential velocity

127

has an increasing effect on the axial velocity. The IFW axial velocity increases more slowly than in pool fire because of the lower temperature distribution at the base of the flame due to stronger fuel vaporization. However, the maximum axial velocity of IFW is much larger than the maximum axial velocity of a turbulent pool fire with the same diameter at the position higher than 0.6 m.

Fig. 7.13: Average centerline velocity

Chapter 8. Conclusion

In this research, the internal fire whirl generated inside a vertical shaft is discussed. At first, it has been looked into deeply about the correlation on the single corner g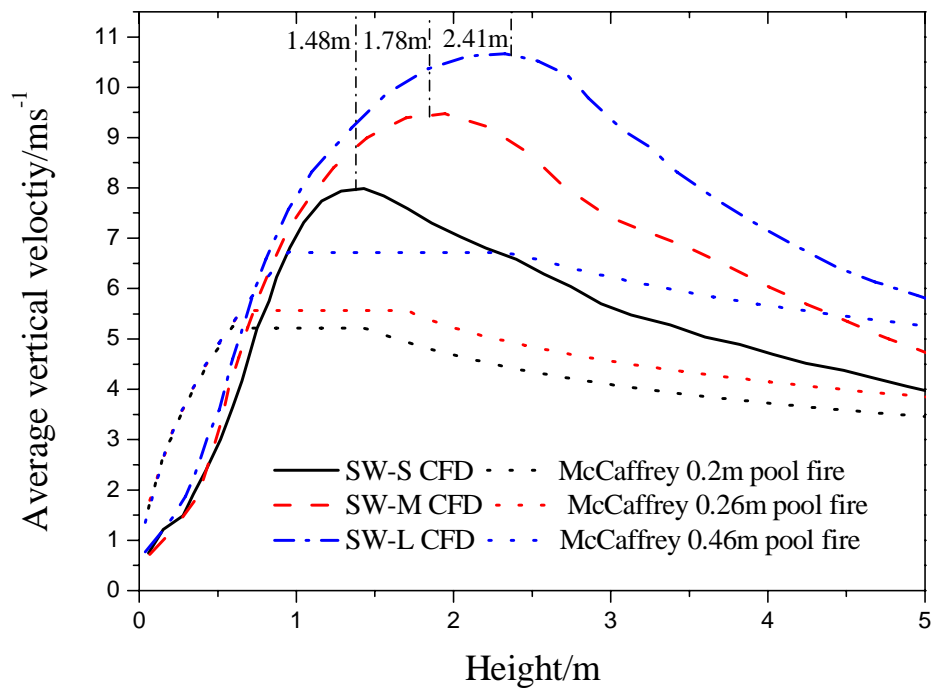ap width of the flame height based on some experimental data of a large-scale fire test on IFW. If the corner gap of the vertical shaft is too narrow or too wide, IFW cannot be formed. By using the experimentally observed flame swirling and compiled data with the assistance of an analytical study, a correlation of the width of the corner gap and the flame height of the IFW is obtained.

Secondly, this research project has further looked into the details of flame swirling. A high speed camera has been applied for a smaller scaled model to generate an IFW. It has been again investigated that even in a smaller scaled model, IFW will only be formed in a certain range of the single corner gap width, not too narrow or too wide. The IFW cannot be formed in an very narrow corner gap as well as when the gap opening is larger than half of the width of the vertical shaft. With the aid of the high speed camera, two vertex tubes were observed which moved around the horizontal pool fire surface. It is difficult to observe the fast-moving swirling motion of the IFW before without the use of a high speed camera. Therefore, this research has provided some innovative insight for the formation of the IFW. Furthermore, with the experimental data obtained coupled with some equations derived in the first part of this research, correlation between the flame height of the IFW and the width of the corner gap is further deduced.

Apart from the study of IFW inside a vertical shaft with a single corner gap with an open roof, experiment has also been carried out on a vertical shaft model with

different settings of the roof opening in which two scenarios have been studied with the front half of the roof opened and rear half of the roof opened. Background-oriented Schlieren (BOS) technique is used to record the hot smoke escaped from the vertical shaft. From the experiment, it is found that the IFW formed for both scenarios is similar regarding the flame height, neutral plane height, burning time and mass loss rate of the fuel. As compared to a shaft model with a closed roof, the IFW for a semi-opened roof model forms better (i.e. a higher flame height and faster burning time as well as a higher neutral plan height). The difference between the setting for a front closed roof and rear closed roof shaft model is that the latter contribute to a lower hot smoke layer temperature.

Furthermore, the swirling characteristics of the internal fire whirl are also studied. The variation of swirling characteristics and vertical flame velocity with height for IFW in vertical shafts was investigated using the vorticity transport equation with experimental data. Semi-empirical expressions were obtained, supplemented with discussions based on the relative effects baroclinic force and buoyancy force. Such relative effects depend on height and on the heat release rate from the fire pool. Classical solutions of Rankine, Oseen and Burgers vortex are limited to radial variation of ω_z and V_θ, with ω_z and V_θ not changing along the vertical direction. This paper presents a simple theoretical model of the fire whirl and the decay of rotation speed along the height, and gives some experiments to prove it indirectly in a vertical shaft. Upon generation of a fire whirl, *Fr* varies from infinity to 0 from the bottom to the top of flame. The fire whirl height is mainly affected by fuel surface temperature, external temperature, and density differences. The temperature and density differences produce a very big baroclinic force to maintain the swirling

130

ability of fire whirl when *Fr* approaches infinity. The longer the baroclinic force is maintained along the height, the taller is the flame height of the fire whirl.

Likewise, a numerical method is also used to study the characteristics of IFW. The temperature (average and time dependent), burning rate, IFW height and diameter were measured. With SGS Smagorinsky CFD-FDS simulation, the simulated results agree well with the experimental results on flame patterns, velocity (vertical and tangential), vortex core radius. It is found that circumferential non-uniform density difference and baroclinic gradient due to buoyancy contribute to tangential current generation. Thus, IFW forms more easily with larger HRR. Also, the single corner gap IFW character development process can be divided into six stages. In each stage, the relationship between the vertical transient temperature and flame shape is summarized. Good agreements of experimental and simulated flame surface are achieved. Comparison between average vertical temperature of IFW and pool fire is studied. IFW has longer flame region and intermittent region. Empirical equation for IFW vertical temperature is also derived.

To sum up, this research has provided a more in-depth investigation into the characteristics and the relationship between IFW and the vertical gap width of a vertical shaft, which is an area not extensively explored in previous studies. Also, high-speed camera and BOS technique used in this research allow us to have a more detailed study of the formation of different stages of the IFW and the smoke movement of IFW.

An IFW can be a dangerous if it happened inside a building as compared to a normal fire. This could happen in building areas similar to the vertical shaft discussed in this

research such as lift shaft and duct shaft [91-92]. The fire can reach a much higher flame height as well as a faster burning rate. The result and insight of this research would be useful to determine the appropriate passive and active fire safety provisions for vertical shafts in tall buildings where IFW might be generated.

References

1. Schencking C., "The Great Kantō Earthquake and the Chimera of National Reconstruction in Japan", New York: Columbia University Press, Chapter 1., (2013)

2. Hissong J.E., "Whirlwinds at Oil-Tank Fire, San Luis Obispo, Calif". Monthly Weather, Volume 54, Issue 4, p.161–163,(1926)

3. Emmons H.W. and Ying S.J., "The Fire Whirl", Eleventh Symposium (International) on Combustion, The Combustion Institute, Pittsburgh, Pennsylvanina, USA, p. 475-488, (1967)

4. Pinto C., Viegas D., Almeida M., Raposo J., "Fire whirls in forest fires: An experimental analysis", Fire Safety Journal, Volume 87, p.37-48 (2017)

5. Quintiere J.G., "Canadian Mass Fire Experiment", Journal of Fire Protection Engineering, Volume 5, Issue 2, p.67-78,(1993)

6. Perry G.L.W., "Current approaches to modelling the spread of wildland fire: a review", Progress in Physical Geography: Earth and Environment, Volume. 22, Issue 2, p.222-245, (1998)

7. Williams F. A., "Urban and wildland fire phenomenology", Progress in Energy and Combustion Science, Volume 8, Issue 4, p.317-354, (1982)

8. Chow W.K. and Han S.S., " Experimental data on scale modeling studies on internal fire whirls", International Journal on Engineering Performance-Based Fire Codes, Volume 10, Number 3, p.63-74, (2011)

9. Chow W.K., He Z. and Gao Y., "Internal fire whirls in a vertical shaft", Journal of Fire Sciences, Vol. 29, Issue 1, p. 71-92, (2011)

10. Satoh K and Yang K.T., "Experimental observations of swirling fires", Proceedings of ASME Heat Transfer Division, HTD-Volume. 335, Volume. 4, p.393-400, (1996)

11   Snegirev A .Yu., Marsden J.A., Francis J., Makhviladze G.M., "Numerical studies and experimental observations of whirling flames." Internaltinal Journa of Heat and Mass Transfer, Volume 47, Issue 12-13, p.2523-2539, (2004)

12   Kuwana K., Sekimoto K., Saito K. and Williams F.A., "Scaling fire whirls", Fire Safety Journal, Volume 43, Issue 4, p.252-257, (2008)

13   Lei J., Liu N.A., Zhang L.H., Chen H.X., Shu L.F., Chen P., Deng Z.H., Zhu J.P., Satoh K. and de Ris J.L., "Experimental research on combustion dynamics of medium-scale fire whirl", Proceedings of the Combustion Institute, Volume 33, Issue 2, p.2407-2415, (2011)

14   Yuen A.C.Y., Yeoh G.H., Cheung S.C.P., Chan Q.N., Chen T.B.Y., Yang W. and Lu H., "Numerical study of the development and angular speed of a small-scale fire whirl", Journal of Computational Science, Volume 27, p.21-34, (2018)

15   Jiao L., Liu N.A., Lozano J.S., Zhang L.H, Deng Z.H. and Satoh K., "Experimental research on flame revolution and precession of fire whirls", Proceedings of the Combustion Institute, Volume 34, Issue 2, p.2607-2615, (2013)

16   Kuwana K., Morishita S., Ritsu Dobashi R., Chuah K.H. and Saito K., "The burning rate's effect on the flame length of weak fire whirls", Proceedings of the Combustion Institute, Volume 33, Issue 2, p. 2425–2432, (2011)

17   Zou G.W., Chow W.K., "Generation of an internal fire whirl in an open roof vertical shaft model with a single corner gap", Journal of Fire Sciences, Volume 33, Issue 3, p.183-201, (2015).

18   Chow W.K., Han S.S., "Experimental investigation on onsetting internal fire whirls in a vertical shaft", Journal of Fire Sciences, Volume 27, Issue 6, p.529-543, (2009).

19   Yu H.Y., Guo S., Peng M.J., Li Q.W., Ruan J.F., Wan W. and Chen C., "Study on the influence of air-inlet width on fire whirls combustion characteristic", Procedia Engineering, Volume 62, p.813-820, (2013)

20   Zou G.W., Yang L. and Chow W.K., "Numerical studies on fire whirls in a vertical shaft", Proceedings of 2009 US-EU-China Thermophysics Conference-Renewable Energy (UECTC-RE '09), Beijing, China, 28-30 May (2009)

21   Chow W.K., "A study on relationship between burning rate and flame height of internal fire whirls in a vertical shaft model" Journal of Fire Science, Volume 32, Issue 1, p.72-83, (2014)

22   Zou G.W.,Chow W.K., "Generation of an internal fire whirl in an open roof vertical shaft model with a single corner gap", Journal of Fire Science, Volume 33, Issue 3, p.183-201, (2015)

23   Chen H.T., Lou L.L., Qiu J.Z., "Accident Cause Analysis and Evacuation Countermeasures on the High-Rise Building Fires", Procedia Engineering, Volume 43, p.23-27, (2012)

24   Liu X.Y., Zhang H., Zhu Q.M., "Factor Analysis of High-Rise Building Fires Reasons and Fire Protection Measures", Procedia Engineering, Volume 45, p.643-648, (2012)

25   Yu Y., Chu Y.Y, Liang D, "Study on Smoke Control Strategy in a High-rise Building Fire", Procedia Engineering, Volume 71, p.145-152, (2014)

26   Xu X.Y., Wang Z.H, Liu X.Y., Ji C., Yu N.H, Zhu H.Y., Li J.J., Wang P.F., "Study on Fire Smoke Control in Super-high Building Atrium, Procedia Engineering, Volume 211, p.844-852, (2018)

27   Meroney R.N., "Fire whirls and building aerodynamics", Proceedings of 11th International Conference on Wind Engineering, Texas Tech University, Lubbock, TX, June (2003)

28   Meroney R.N., "Fire Whirls, Fire Tornadoes and Firestorms: Physical and Numerical Modelling", Proceedings of Physmod 2003: International Workshop on Physcial Modelling of Flow and Dispersion Phenomena, (2003)

29   Durox D, Moeck J.P., Bourgouin J.F., Morenton P., Candel S., "Flame dynamics of a variable swirl number system and instability control", Combustion and Flame, Volume 160, Issue 9, p.1729-1742, (2013)

30   Mansouri Z., Aouissi M., Boushaki T., "Numerical computations of premixed propane flame in a swirl-stabilized burner: Effects of hydrogen enrichment, swirl number and equivalence ratio on flame characteristics", International Journal of Hydrogen Energy, Volume 41, Issue 22, p. 9664-9678, (2016)

31   Jerzak W., Kuźnia M., "Experimental study of impact of swirl number as well as oxygen and carbon dioxide content in natural gas combustion air on flame flashback and blow-off", Journal of Natural Gas Science and Engineering, Volume 29, p.46-54, (2016)

32   Liu J.Z., Liu Z.H., Chen S., Santos S.O., Zheng C.G., "A numerical investigation on flame stability of oxy-coal combustion: Effects of blockage ratio, swirl number, recycle ratio and partial pressure ratio of oxygen", International Journal of Greenhouse Gas Control, Volume 57, p.63-72, (2017)

33   Meroney R.N., "Fires in porous media: natural and urban canopies", Flow and Transport Processes with Complex Obstructions, Springer, Chapter 8, p.271-310, (2007)

34   Yu D.H., Zhang P., "On the flame height of circulation-controlled firewhirls with variable density", Proceedings of the Combustion Institute, Volume 36, Issue 2, p.3097-3104, (2017)

35   Lei J., Liu N.A., Tu R., "Flame height of turbulent fire whirls: A model study by concept of turbulence suppression", Proceedings of the Combustion Institute, Volume 36, Issue 2, p.3131-3138, (2017)

36   Hartl K.A., Smits A.J., "Scaling of a small scale burner fire whirl", Combustion and Flame, Volume 163, p. 202-208, (2016)

37   Hui Y., Gao Y. and Huang D.X., "Numerical Simulation of Internal Fire whirls in an Inclined Shaft", Advanced Materials Research, Volume 732-733, p.254-257, (2013)

38   Yuen A.C.Y., Yeoh G.H., Yuen R.K.K., Lo S.M., "Numerical Study on Small-Scale Fire Whirl using Large Eddy Simulation", Proceedings of the 3rd International Conference on Fluid Flow, Heat and Mass Transfer, Paper No. 165, (2016)

39   Satoh K, Liu N.A., Zhou K.B., Xie X.D., "CFD Study of Termination of Fire Whirls in Urban Fires", Procedia Engineering, Volume 62, p.1040-1049, (2013)

40   Sasaki T., Igari M., Kuwana K., "Fire whirls behind an L-shaped wall in a crossflow", Combustion and flame, Volume 197, p.197-203, (2018)

41   Huo Y., Chow W.K., Chow C.L., "Generation and characteristics of internal fire whirl in a shaft model with two corner slits under microgravity conditions", Advances in Space Research, Volume 59, p.3058-3069, (2017)

42   Yuen A.C.Y., Yeoh G.H., Cheung S.C.P., Chan Q.N., Chen T.B.Y., Yang W., Lu H., "Numerical study of the development and angular speed of a small-scale fire whirl, Journal of Computational Science", Volume 27, p.21-34, (2018)

43   Klimenko A.Y., Williams F.A., "On the flame length in firewhirls with strong vorticity", Combustion and Flame, Volume 160, Issue 2, p.335-339 (2013)

44   Cheung C.P.S., Yeoh G.H., "A fully-coupled simulation of vortical structures in a large-scale buoyant pool fire", International Journal of Thermal Sciences, Volume 48, Issue 12, p.2187-2202, (2009)

45   He B.S., Diao Y.F., Xu J.Y., Chen C.H., "Vorticity measurements in complex 3-D flow in tangentially-fired furnaces", Flow Measurement and Instrumentation, Volume 13, Issue 4, p.173-181, (2002)

46   Iqbal N., Salley M.H., Weerakkody S., "Fire Dynamics Tools (FDTs): Quantitative fire hazard analysis methods for the U.S. nuclear regulatory commission fire protection inspection program" (2004)

47   Chuah K.H. and Kushida G. "The prediction of flame heights and flame shapes of small fire whirls" Proceedings of the Combustion Institute, Issue 31: p.2599-2606. (2007)

48   Chuah K.H., Kuwana K. and Saito K., "Modeling a fire whirl generated over a 5-cm-diameter methanol pool fire" Combustion and Flame, Volume 156, Issue 9, p.1828-1833, (2009)

49   Matsuyama K., Ishikawa N., Tanaka S., Tanaka F., Ohmiya Y., Hayashi Y., "Experimental and numerical studies on fire whirls"

50   Zhou K.B., Liu N.A., Lozano J.S., et al., "Effect of flow circulation on combustion dynamics of fire whirl". Proceedings of the Combustion Institute, Volume 34, Issue 2, p.2617–2624, (2013)

51   Lei J., Liu N., "Burning rates of liquid fuels in fire whirls", Combustion and Flame, Volume 159, p.2104-2114, (2012)

52   Zhou R., Wu Z.N., "Fire whirls due to surrounding flame sources and the influence of the rotation speed on the flame height", Journal of Fluid Mechanics Volume 583, p.313-345, (2007)

53   Hill K., Dreisbach J., "Verification and Validation of Seclected Fire Models for Nuclear Power Plant Application – Volume 7: Fire Dynamic Simulator (FDS), NUREG-1842, (2007)

54   McGrattan k., Floyd J., Forney G., Baum H., Hostikka S., "Improved Radiation and Combustion Routines for a Large Eddy Simulation Fire Model", Fire Safety Science – Proceeding of the Seventh International Symposium, p.827-838, (2005)

55   de Ris, J., "Scale Modeling of Fires", Keynote lecture, Eighth International Symposium on Scale Modeling (ISSM-8), Portland, Oregon, USA, (2017).

56   Church C.R. et al., "Intense Atmospheric Vortices Associated with a 1000 MW Fire", Bulletin of the American Meteorological Society, Volume 61, Issue 7, p.682-694, (1980)

57   Venkatesh S. et al., "Flame Base Structure of Small-Scale Pool Fires", Proceedings of 26th Symposium (International) on Combustion, p.1437-1443, (1996)

58   Kuwana, K. et al., "Numerical Simulation of Internal Fire whirls t on the Flame Length of Weak Fire Whirls", Proceedings of Combustion Institute, Volume 33 , Issue 2, p.2425-2432, (2011)

59   Raffel M., "Background-oriented schlieren (BOS) techniques", Experiment in. Fluids, Volume 56, p.1–17, (2015)

60   Su C.H., Bai J.H., "Measurement of the neutral plane of an internal fire whirl using the background-oriented Schlieren technique for a vertical shaft model of a high- rise building", Measurement, Volume 78, p.151–167, (2016)

61   Su C.H., Ke, Y.P., Chow W.K., Hsu M.C., "Application of Schlieren Photography to Study Neutral Plane in a Compartment Fire with Scale Models", p. V002T05A011- V002T05A011, ASME 2013 Heat Transfer Summer Conference collocated with the ASME 2013 7th International Conference on Energy Sustainability and the ASME 2013 11th International Conference on Fuel Cell Science, Engineering and Technology, American Society of Mechanical Engineers, (2013)

62   Ota M., Leopold F., Jagusinski F., Maeno K., "Comparison between CBOS (colored background oriented schlieren) and CGBOS (colored-grid background oriented schlieren) for supersonic flow", Proceedings of the 15th international Symposium on Flow Visualization, (2012)

63   Soma S., Saito K., "Reconstruction of fire whirls using scale models. Combust Flame", Volume 86, Issue 3, p.269-284, (1991)

64   Hassan M.I., Kuwana K., Saito K. et al., "Flow structure of a fixed-frame type fire whirl", Fire Safety Science – Proceedings of the Eighth International Symposium, p.951-962, (2005)

65   Satoh K., Yang K.T., "Simulations of swirling fires controlled by channeled self-generated entrainment flows", Fire Safety Science – Proceedings of the Fifth International Symposium, p.201-212, (1997)

66   Lei J, Liu N., "Flame precession of fire whirls: A further experimental study", Fire Safety Journal, Volume 79, p.1-9, (2016)

67   Wu H.M., Gao Y. and Chow W.K., "Studies on internal fire whirls in a vertical shaft with a single corner gap", Journal of Applied Fire Science, Volume 22, Issue 2, p.179-200, (2013)

68   Wada Y., Kuwana K., "Influence of vortex structure on fire whirl behavior", Fire Safety Science, Volume 10, p.671-679, (2011)

69   Klimenko A.Y., "Strong swirl approximation and intensive vortices in the atmosphere", Journal of Fluid Mechanics, Volume 738, p.268-298, (2014)

70   Chow W.K., "Performance-based approach to determining fire safety provisions for buildings in the Asia-Oceania regions", Building and Environment, Volume 91, p.127-137, (2015)

71   Saffman P.G., Ablowitz M.J., Hinch E., et al., "Vortex Dynamics", Cambridge: Cambridge University Press, p.253, (1992)

72   McCaffrey B.J., "Momentum implications for buoyant diffusion flames". Combustion and Flame, Volume 52, p.149-167, (1983)

73   Satoh K.,Yang K.T., "Experiments and Numerical Simulations of Swirling Fires due to 2×2 Flames in a Channel with Single Corner Gap", Proceedings of ASME International Mechanical Engineering Congress and Exposition, ASME Heat Transfer Division, Volume. 2, p.74120-127, (1998)

74   Satoh, K.,Yang, K.T., "Measurements of Fire Whirl from a Single Flame in a Vertical Square Channel with Symmetrical Corner Gaps", Proceedings of ASME International Mechanical Engineering Congress and Exposition, ASME Heat Transfer Division, Volume 364, p.167-173, (1999)

75   Lei J., Liu N.A., "Temperature, Velocity and Air Entrainment of Fire Whirl Plume: A Comprehensive Experimental Investigation", Combustion and Flame, Volume 162, Issue 3, p.745-758, (2015).

76   Liu S.L., Chow W.K., "A Review on Numerical Simulation of Turbulent Flow", International Journal on Architectural Science, Volume. 3, Issue 2, p.77-102, (2002)

77   Ma T., Quintiere, J., "Numerical Simulation of Axi-Symmetric Fire Plumes: Accuracy and Limitations", Fire Safety Journal, Volume. 38, Issue 5, p.467-492, (2003)

78   Murakami S., "Overview of Turbulence Models Applied in CWE-1997", Journal of Wind Engineering and Industrial Aerodynamics, Volume 74, p.1-24, (1998)

79   Zhang W., Chen Q.Y., "Large Eddy Simulation of Indoor Airflow with a Filtered Dynamic Subgrid Scale Model", International Journal of Heat and Mass Transfer, Volume 43, Issue 17, p.3219-3231, (2000)

80   Jiang Y., Chen Q.Y., "Study of Natural Ventilation in Buildings by Large Eddy Simulation", Journal of Wind Engineering and Industrial Aerodynamics, Volume. 89, Issue 13, p.1155-1178, (2001)

81   Satoh K., Yang K.T., "Simulation of Swirling Fires Controlled by Channeled Self-generated Entrainment Flows, Fire Safety Science", Proceedings of the 5th International Symposium, International Association for Fire Safety Science, p. 208-216, (1997)

82   Chow W.K., Dang J.F., Gao Y., Chow, C.L., "Dependence of Flame Height of Internal Fire Whirl in a Vertical Shaft on Fuel Burning Rate in Pool Fire", Applied Thermal Engineering., Volume. 121, p.712-720, (2017)

83   Zhou X., Luo K.H., Williams J.J.R., "Numerical Studies On Vortex Structures In The Near-Field Of Oscillating Diffusion Flame", Heat and Mass Transfer, Volume 137, p.110-161, (2001).

84   Warrantz U., Maas U., Debbie R.W., "Combustion", Berlin: Springer-Verlag, (1996).

85   Zhang W., Hamer A., Klassen M., Carpenter D., "Turbulence Statistics in a Fire Room Model by Large Eddy Simulation", Fire Safety Journal., Volume 37, Issue 8, p.721-752, (2002)

86   Cheung S.C.P.,Yeoh G.H., "A Fully-coupled Simulation of Vertical Structures in a Large-scale Buoyant Pool Fire", International Journal of Thermal Science, Volume 48, p.2187-2202, (2009).

87   Wang H.Y., "Numerical Study of Under-ventilated Fire in Medium-scale Enclosure", Building and Environment, Volume 44, Issue 6, p.1215-1227, (2009).

88   Zukoski E.E., Kubota T., Cetegen, B., "Entrainment in fire plumes", Fire Safety Journal, Volume 3, Issue 3, p.107-121, (1981).

89   Bullen M.L., Thomas P.H., "Compartment Fires with Non-cellulosic Fuels", Proceedings of the Combustion Institute, Volume 17, Issue 1, p.1139-1148, (1979).

90   McCaffrey B.J., "Purely Buoyant Diffusion Flames: Some Experimental Results", NBSIR 79-1910, National Bureau of Standards, Gaithersburg, Maryland, p.10-16, (1979).

91   Chow W.K., Hung W.Y., "On the fire safety for internal voids in highrise buildings", Building and Environment, Issue 38, Volume 11, p.1317-1325, (2003)

92   Chow W.K., Fong N.K., Lui C.H.G, Tam T.K., Yue T.K., "Fire Safety Strategies for Supertall Buildings in Hong Kong", CTBUH Journal, Issue 1, p.26-31, (2013)

Appendix: Derivation of key equation (6.11) in Chapter 6

Equation (6.11) is given as:

$$\frac{d^2\omega_{zz}}{dz^2} - (\frac{\alpha}{v_z}z + \frac{b}{v_z})\frac{d\omega_{zz}}{dz} + \frac{\alpha}{v_z}\omega_{zz} = 0$$

Let

$$\omega_{zz} = \sum_{n=0}^{\infty} a_n z^n = a_0 + \sum_{n=1}^{\infty} a_n z^n \qquad (A1)$$

$$\frac{d\omega_{zz}}{dz} = \sum_{n=1}^{\infty} na_n z^{n-1} \qquad (A2)$$

$$\frac{d^2\omega_{zz}}{dz^2} = \sum_{n=2}^{\infty} n(n-1)a_n z^{n-2} = \sum_{n=0}^{\infty} (n+2)(n+1)a_{n+2} z^n = 2a_2 + \sum_{n=1}^{\infty} (n+2)(n+1)a_{n+2} z^n \qquad (A3)$$

Putting into equation (15) gives:

$$2a_2 + \sum_{n=1}^{\infty}(n+2)(n+1)a_{n+2}z^n - \frac{\alpha}{v_z}z\sum_{n=1}^{\infty}na_n z^{n-1} - \frac{b}{v_z}\sum_{n=1}^{\infty}na_n z^{n-1} + \frac{\alpha}{v_z}a_0 + \frac{\alpha}{v_z}\sum_{n=1}^{\infty}a_n z^n = 0$$

$$2a_2 + \sum_{n=1}^{\infty}(n+2)(n+1)a_{n+2}z^n - \sum_{n=1}^{\infty}\frac{\alpha}{v_z}na_n z^n - \frac{b}{v_z}a_1 - \sum_{n=1}^{\infty}\frac{b}{v_z}(n+1)a_{n+1}z^n + \frac{\alpha}{v_z}a_0 + \sum_{n=1}^{\infty}\frac{\alpha}{v_z}a_n z^n = 0$$

$$2a_2 - \frac{b}{v_z}a_1 + \frac{\alpha}{v_z}a_0 + \sum_{n=1}^{\infty}[(n+2)(n+1)a_{n+2} - \frac{b}{v_z}(n+1)a_{n+1} - (\frac{\alpha}{v_z}n - \frac{\alpha}{v_z})a_n]z^n = 0$$

$$2a_2 - \frac{b}{v_z}a_1 + \frac{\alpha}{v_z}a_0 = 0 \quad \Rightarrow \quad a_2 = -\frac{\alpha}{v_z}\frac{a_0}{2} + \frac{b}{v_z}\frac{a_1}{2}$$

Or

$$(n+2)(n+1)a_{n+2} - \frac{b}{v_z}(n+1)a_{n+1} - (\frac{\alpha}{v_z}n - \frac{\alpha}{v_z})a_n = 0$$

$$(n \geq 1)$$

$$\Rightarrow \quad a_{n+2} = \frac{\alpha}{v_z}\frac{n-1}{(n+2)(n+1)}a_n + \frac{b}{v_z}\frac{1}{n+2}a_{n+1}$$

Each term a_n has to be known. Putting

$$a_0 = a_0, \quad a_1 = 0,$$

$$\Rightarrow \; a_2 = -\frac{\alpha}{\overline{v}_z}\frac{a_0}{2}$$

$$a_3 = \frac{b}{\overline{v}_z}\frac{1}{3}a_2 = \frac{b}{\overline{v}_z}\frac{1}{3}\left(-\frac{\alpha}{\overline{v}_z}\frac{a_0}{2}\right) = -\frac{1}{6}\frac{\alpha b}{\overline{v}_z^2}a_0$$

$$a_4 = \frac{\alpha}{\overline{v}_z}\frac{1}{12}a_2 + \frac{b}{\overline{v}_z}\frac{1}{4}a_3$$

$$= \frac{\alpha}{\overline{v}_z}\frac{1}{12}\left(-\frac{\alpha}{\overline{v}_z}\frac{a_0}{2}\right) + \frac{b}{\overline{v}_z}\frac{1}{4}\left(-\frac{1}{6}\frac{\alpha b}{\overline{v}_z^2}a_0\right) = -\frac{1}{24}\left(\frac{\alpha}{\overline{v}_z}\right)^2 a_0 - \frac{1}{24}\frac{\alpha b^2}{\overline{v}_z^3}a_0$$

$$a_5 = \frac{\alpha}{\overline{v}_z}\frac{2}{20}a_3 + \frac{b}{\overline{v}_z}\frac{1}{5}a_4 = \frac{\alpha}{\overline{v}_z}\frac{1}{10}\left(-\frac{1}{6}\frac{\alpha b}{\overline{v}_z^2}a_0\right) + \frac{b}{\overline{v}_z}\frac{1}{5}\left(-\frac{1}{24}\left(\frac{\alpha}{\overline{v}_z}\right)^2 a_0 - \frac{1}{24}\frac{\alpha b^2}{\overline{v}_z^3}a_0\right)$$

$$= -\frac{1}{60}\frac{\alpha^2 b}{\overline{v}_z^3}a_0 - \frac{1}{120}\frac{\alpha^2 b}{\overline{v}_z^3}a_0 - \frac{1}{120}\frac{\alpha b^3}{\overline{v}_z^4}a_0$$

$$= -\frac{1}{40}\frac{\alpha^2 b}{\overline{v}_z^3}a_0 - \frac{1}{120}\frac{\alpha b^3}{\overline{v}_z^4}a_0$$

$$a_6 = \frac{\alpha}{\overline{v}_z}\frac{3}{30}a_4 + \frac{b}{\overline{v}_z}\frac{1}{6}a_5$$

$$= \frac{\alpha}{\overline{v}_z}\frac{1}{10}\left(-\frac{1}{24}\left(\frac{\alpha}{\overline{v}_z}\right)^2 a_0 - \frac{1}{24}\frac{\alpha b^2}{\overline{v}_z^3}a_0\right) + \frac{b}{\overline{v}_z}\frac{1}{6}\left(-\frac{1}{40}\frac{\alpha^2 b}{\overline{v}_z^3}a_0 - \frac{1}{120}\frac{\alpha b^3}{\overline{v}_z^4}a_0\right)$$

$$= -\frac{1}{240}\left(\frac{\alpha}{\overline{v}_z}\right)^3 a_0 - \frac{1}{120}\left(\frac{\alpha b}{\overline{v}_z^2}\right)^2 a_0 - \frac{1}{720}\frac{\alpha b^4}{\overline{v}_z^5}a_0$$

$$\omega_{zz}(z) = a_0 - \frac{1}{2}\frac{\alpha}{\overline{v}_z}a_0 z^2 - \frac{1}{6}\frac{\alpha b}{\overline{v}_z^2}a_0 z^3 - \frac{1}{24}\left[\left(\frac{\alpha}{\overline{v}_z}\right)^2 + \frac{\alpha b^2}{\overline{v}_z^3}\right]a_0 z^4 - \left(\frac{1}{40}\frac{\alpha^2 b}{\overline{v}_z^3} + \frac{1}{120}\frac{\alpha b^3}{\overline{v}_z^4}\right)a_0 z^5$$

$$- \left[\frac{1}{240}\left(\frac{\alpha}{\overline{v}_z}\right)^3 + \frac{1}{120}\left(\frac{\alpha b}{\overline{v}_z^2}\right)^2 + \frac{1}{720}\frac{\alpha b^4}{\overline{v}_z^5}\right]a_0 z^6 + \cdots$$

From $\omega_{zz}(0) = \omega_{zmax}$, one gets:

$$a_0 = \omega_{zzmax} \tag{A4}$$

Taking the first three terms gives equation (6.13).

144